A CLASS OF ITS OWN: FUNCTION-DISCOVERY OF HYDY, A NOVEL CLASS OF [FEFE]-HYDROGENASES

A Dissertation

by

DARRELL WAYNE MARTIN JR

Submitted to the Office of Graduate and Professional Studies of
Texas A&M University
in partial fulfillment of the requirements for the degree of

DOCTOR OF PHILOSOPHY

Chair of Committee,	David P. Barondeau
Committee Members,	Marcetta Y. Darensbourg
	Paul A. Lindahl
	Frank M. Raushel
Head of Department,	Simon W. North

August 2016

Major Subject: Chemistry

ABSTRACT

Hydrogen has received widespread attention as a potential energy carrier due to its high energy content and clean combustion product H_2O. [FeFe]-H_2ases exhibit the highest H_2 production rates utilizing a complex iron sulfur cofactor, called the H-cluster, that requires three biosynthetic maturation proteins. Mutagenesis studies of conserved residues surrounding the H-cluster led to variants with either decreased overall activity or minimal H-cluster incorporation. These studies underscore the importance of the protein matrix in tuning active site chemistry. Here, we investigated a new class of enzymes consisting of N-terminal [FeFe]-H_2ase fused to a C-terminal rubrerythrin domain (named HydY). Using protein film electrochemistry and colorimetric assays, HydY was found to function differently than standard [FeFe]-H_2ases: it exhibits strong product inhibition for H^+ reduction, a low K_M for H_2 oxidation, bias toward H_2 oxidation and significant overpotential. We hypothesized that the altered reactivity for HydY was due to hydrogen bonds from conserved residue substitutions vital for H-cluster coordination. Consistent with this hypothesis, HydY variants result in enzymes with catalytic properties more similar to traditional [FeFe]-H_2ases. In addition, the C-terminal domain (CTD) of HydY efficiently reduces H_2O_2 to H_2O. Electronic absorbance, EPR and Mössbauer spectroscopic studies of the CTD are consistent with a rubrerythrin di-iron active site with flanking mononuclear iron sites. A 1.77 Å crystal structure of the CTD reveals a domain swapped dimer in which ligands for a modified di-iron rubrerythrin active site are provided by residues across the dimer interface. Further, our

results indicate that electrons generated by the oxidation of H_2 are transferred to the CTD, presumably for H_2O_2 reduction. This is the first example of H_2-dependent peroxidase. We hypothesize that evolution 'tuned' HydY to favor H_2 oxidation and that HydY has a protective role in anaerobic bacteria that allows survival upon transient oxygen exposure. Additional bioinformatics indicate that HydY belongs to a broader class of [FeFe]-H_2ases that also use H_2 as a reductant for various substrates. Overall, these studies identify determinants for controlling active site chemistry of [FeFe]-H_2ases that may lead to improved design of biomimetic compounds with implications in energy production.

DEDICATION

This dissertation is dedicated to my loving, patient and supportive wife Elizabeth, from whom I received constant encouragement and support kept me motivated to complete my Ph.D.

ACKNOWLEDGEMENTS

I would like to acknowledge my advisor Dr. David Barondeau. He taught me how to think critically and deeply, how to analyze a scientific idea to the core, to understand the fundamentals of a research project. He taught me how to be a scientist, and for that I will always be thankful and grateful. I would also I would like to thank my committee members, Dr. Marcetta Darensbourg, Dr. Paul Lindahl and Dr. Frank Raushel for their helpful suggestions, support and guidance throughout my career at Texas A&M.

I would like to thank my colleagues from the Barondeau lab, past and present, for their helpful discussions and suggestions during my research endeavors. Specifically, I would like to thank Seth Cory for his expertise with protein crystallography and my previous undergraduate students Samuel Choi, Eric Redundo and Nathan Winser.

I must also acknowledge my invaluable and excellent collaborators. Mössbauer was collected and interpreted by Josh Wofford and Dr. Paul Lindahl, PFE and protein reconstitution with synthetic $[2Fe]_H$ was conducted by Garrett Williams in Dr. Anne Jones lab at ASU and computational modeling was started by Dr. Haixai Li in Dr. Michael Hall's lab. I was lucky enough to travel to ASU to learn PFE, and I must again thank both my advisor and Dr. Jones for the opportunity and experience. My research is indebted to all my collaborators. Thank you also to Dr. James Sacchetini for allowing me to use his Mosquito robot and x-ray equipment to set up crystal trays and crystal screening. Thank you also to Stanford Synchrotron Radiation Laboratory for providing opportunities to collect crystallography data at their synchrotron.

Finally, I would like to thank my friends, family and again my wife, Elizabeth, for their amazing support.

TABLE OF CONTENTS

LIST OF FIGURES

LIST OF TABLES

CHAPTER I

THE ANAEROBIC WAY OF LIFE

Introduction

Since the discovery of H_2 oxidation and production pathways in the early 20th century,[1] the metabolism of H_2 has been reported in bacteria, archaea and eukaryotes.[2,3] H_2 metabolism is now abundantly clear to be essential to many microbes: from organotrophs (microbes that catabolize organic compounds) to phototrophs (microbes that harness solar energy) and lithotrophs (microbes that use inorganic substrates for reducing equivalents), aerobes to anaerobes alike. H_2 has even been postulated to have been central to primordial evolution of life.[4]

Recent studies suggest that H_2 metabolism is far more widespread (and diverse) than previously postulated.[5,6] Central to H_2 metabolism are hydrogenases (H_2ases). These enzymes are named according their active site metals: [FeFe], [NiFe] and [Fe] (see *Diversity of hydrogenases*). In general, [FeFe]-H_2ases are described to favor H_2 production and are utilized in H_2 production pathways, [NiFe]-H_2ases in H_2 oxidation pathways and [Fe]-H_2ases specific to H_2 uptake in methanogens. Dependent mostly on [FeFe]-H_2ases, strict anaerobic environments were originally speculated to be the only niche for H_2 production pathways, but the discovery that phototrophs produce H_2 challenged that assumption.[7] Soil surface bacteria display H_2-dependent growth, presumably scavenging H_2 from the lower atmosphere, utilizing [NiFe]-H_2ases.[8] This finding of aerobic H_2 oxidation disproved the dogma that these metabolisms can exist

only in low O_2/high H_2 environments. Additionally, using deep genome sequencing, over half the identified microbiota flora in higher eukaryotes[5,9,10] contain at least one H_2ase enzyme. For microbes identified in the Human Microbiome Project, [FeFe]-H_2ases are detected in higher numbers than the other two types of H_2ases.[9] Since H_2 does not accumulate in the gut of humans, interspecies H_2 transfer (H_2 syntrophy) is proposed, where microbes import substrates and export metabolic end products to create a 'community budget' for resources necessary for survival.[11]

Here, the focus will be on H_2 production pathways, with a particular primary focus on anaerobic fermentation, and the enzymes utilized for this reaction. A short vignette on H_2 consuming metabolic pathways (and the required enzymes) will also be described.

H_2 evolving microbes: Anaerobic metabolism

Anaerobic fermentation is a process of energy production from substrate-level phosphorylation using oxidation of organic matter and relievement of excess reducing equivalents by evolving H_2.[12] The route of fermentative H_2 production begins with glycolysis. Carbohydrates, specifically glucose, are preferred substrates in this pathway,[13] where these substrates are converted to pyruvate, ATP and NADH in both strict anaerobes (such as members of the genus *Clostridium*) and facultative anaerobes (such as the proteobacteria *Escherichia coli*, *Ec*). Most Clostridria convert pyruvate to acetyl-CoA and CO_2 using pyruvate ferredoxin oxidoreductase (PFOR).[13-15] PFOR utilizes a thiamine cofactor to activate pyruvate by two successive, one electron oxidation reactions that are transferred through Fe-S cluster cofactors to ferredoxins

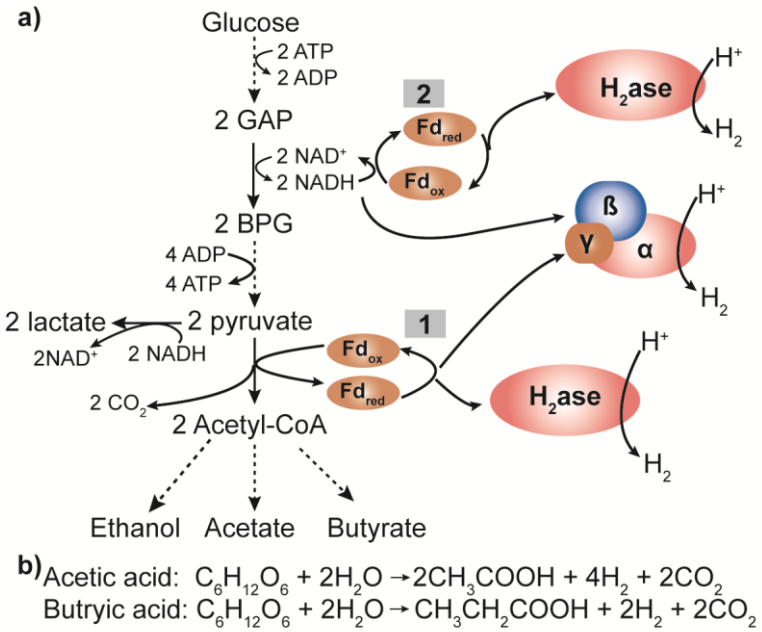

Figure I-1. Highlighting the role of [FeFe]-H_2ases in fermentative H_2 production. A) Fermentative H_2 production pathway in clostridia. There are two routes for H_2 production. One is linked to the action of pyruvate:ferredoxin oxidoreductase and reducing equivalents can be passed to monomeric or bifurcating H_2ases (1). The second pathway involves NADH:ferredoxin oxidoreductase (2), but only operates under extremely low H_2 partial pressures. B) Stoichiometry of anaerobic fermentation of glucose.

(Fds).[16,17] Reduced ferredoxins are used to produce H_2 via [FeFe]-H_2ases. Hydrogenases act as terminal electron acceptors, harnessing the low potential electrons from pyruvate oxidation (E' = -500 mV) to drive proton reduction (Figure I-1).[3,15] A similar pathway exists for the green algae *Chlamdynomous rheinhardtii* (*Cr*) through dark fermentation,[18] as it also does in the hyperthermophile *Pyrococcus furiousus* (*Pf*), although this archaea instead uses a [NiFe]-H_2ase to accomplish the same chemistry.[19] Maximally, 4 moles of H_2 can be produced per mole of glucose from glycolysis. NADH has been speculated to act as an electron source for H_2 production from monomeric H_2ases.[13] This reaction uses NADH:ferredoxin oxidoreductase (NFOR) and can only proceed at very low H_2 partial

pressures (see *Electrochemistry of Hydrogenases*). Highlighting the ingenuity of nature, recent studies of heteromultimeric [FeFe]-H_2ases have been found to minimize energy loss. These enzymes couple the endergonic reaction of NADH oxidation (E' = -320 mV) with ferredoxin oxidation (E' = -450 to -500 mV) to use protons as electron acceptors.[20-23] NAD^+ can be regenerated to form acetate, butyrate or ethanol. Under certain cellular conditions, NAD^+ can be formed directly from pyruvate, forming lactate.[13,14] Most *Clostridium* sp also reduce nitrate to ammonia,[24] but this is a H_2-independent pathway and lies outside the scope of this review. Acetate fermentation maximally yields four moles of H_2, while butyrate only yields 2 moles.[13] Rarely are these yields obtained due to various other metabolic shunts for reducing equivalents.

In facultative anaerobes, pyruvate is converted to acetyl-CoA and formate by pyruvate formate lyase (PFL).[13] Under acidic conditions and high formate concentrations, formate is disproportionated to CO_2 and H_2 by a membrane bound formate hydrogenlyase (FHL) complex.[4] Formate oxidation to electrons, protons and CO_2 occurs at a molybdenum- and selenocysteine-dependent enzyme, and these reducing equivalents are transferred to a [NiFe]-H_2ase (Hyd-3 in *Ec*) to produce H_2. Since two formate molecules are produced per mole of pyruvate, PFL theoretically produces 2 moles of H_2. Competing pathways for formate minimize H_2 production from pyruvate.[13] The FHL reaction is highly reversible. Indeed, Hyd-3 has received recent attention due to its intriguing chemistry of 'fixing' H_2 into a more easily transportable form, formate.[25]

Outside of anaerobic fermentation, H_2 is produced through several other pathways.[4] H_2 photoproduction pathways exist in a few green algae, including

Chlamdynomous rheinhardtii, *Cr*, that depend on both photosystem (PS) I and II (direct) or only PS II (indirect).[18,26] The direct pathway requires light-induced oxidation of water at PS I, electron transfer from PS I to PS II, and then light-dependent excitation of those electrons to reduce ferredoxin (called PetF). PetF then transfers electrons to an [FeFe]-H_2ase for H_2 production. The indirect pathway appears to only require PS I reduced plastoquinone, and may represent a mechanism to dissipate excess reducing equivalents under specific cellular conditions.[18] Additionally, H_2 is also produced as a by-product of N_2 fixation by nitrogenase-containing microbes. Nitrogenase activates the inert N_2 molecule using a specialized metallocofactor with the chemical formula MFe_7S_9, M=Mo, V or Fe.[27-31] Though nitrogenases show significantly slower catalytic rates of H_2 production in comparison to hydrogenases, this paradoxical H_2 production by nitrogenase is speculated to be a major source of the H_2 oxidized by soil bacteria.[4,8] To further demonstrate the breadth of hydrogenase activity, a fairly new class of bacteria has been identified that couples CO oxidation to H_2 production.[4] This new class of bacteria, called hydrogenogens, can be grown exclusively on CO as a carbon source, utilizing a [NiFe]-H_2ase and membrane-bound carbon monoxide dehydrogenase.[32] CO is a potent inhibitor for all H_2ases,[7] so these [NiFe]-H_2ases must somehow minimize CO diffusion into the active site.

H_2 consuming bacteria

In comparison, the major metabolic activities of H_2-consuming bacteria are wide-ranging.[2,3] Some bacteria found at surface waters use H_2 as an electron donor and O_2 as the terminal electron acceptor.[33,34] Such microbes are called Knallgas (German for

'bang-gas') bacteria. *Ralstonia eutropha* (*Re*) is the best studied Knallgas bacteria. *Re* uses a membrane bound hydrogenase [NiFe]-H_2ase (MBH) anchored to the periplasmic side of the cytoplasm.[4] This MBH is critical for establishing a H^+ gradient and transferring electrons to quinone and cytochromes for respiration. *Re*MBH has attracted significant attention recently due to its ability to maintain H_2 oxidation in O_2.[33,35,36] Furthermore, sulfate-reducing bacteria couple H_2 oxidation to sulfate reduction, with H_2 likely a product of syntrophy. Sulfate-reducing bacteria utilize either [FeFe]- or [NiFe]-H_2ases to accomplish H_2 oxidation, dictated by either metal availability or H_2 partial pressure. There are also the so-called 'ancient' pathways for H_2 oxidation: methanogenesis and acetogenesis.[21] Methanogens can convert H_2 and CO_2 (or methanol in some cases) to methane and water. The reducing power of H_2 is harnessed by multiple H_2ases, including membrane-associated and soluble [NiFe]-H_2ases as well as an [Fe]-only H_2ase. The [Fe]-H_2ase appears to be up-regulated under nickel-limiting conditions.[4] In addition, fumarate respiration is a H_2-dependent pathway.[3] Oxidation of H_2 requires a periplasmic oriented membrane-bound [NiFe]-H_2ase that transfers electrons to a membrane associated fumarate reductase anchored on the cytoplasmic side of the membrane. Lastly, additional H_2 oxidation dependent pathways exist in bacteria, including metal reduction (respiration), dehalogenation respiration and anaerobic photosynthesis, that require [NiFe]-H_2ases.[4]

Diversity of hydrogenases

Hydrogenases are complex catalysts utilized by myriad microorganisms to reversibly reduce protons to H_2. All H_2ases share a common theme of first row, low-

valent transition metals stabilized by small inorganic ligands (CO and/or CN^-), which were first detected by FTIR spectroscopy. While all H_2ases share active site similarity, they belong to three phylogenetically distinct H_2ases classes and are named according to the transition metal content: [NiFe]- and [FeFe]-H_2ases, for which protons, electrons, and H_2 are the only substrates and products, and [Fe]-H_2ases that couples H_2 uptake to pterin reduction in methanogens.[37] [FeFe]-H_2ases are superior hydrogenase catalysts,[38] with H_2 production turnover frequencies[39] of 6,000-9,000 s^{-1} and H_2 oxidation turnovers estimated up to 50,000 s^{-1},[40] while [NiFe]-H_2ases show catalytic rates at least an order of magnitude lower.[40,41] Ratios of H_2 production and consumption point to the metabolic roles of each respective enzyme. This section will focus primarily on [FeFe]-H_2ases with strong comparisons to [NiFe]-H_2ases.

Structure and function of [Fe]-H_2ases

[Fe]-H_2ases, named because the active site contains only a single iron atom are also called Hmd H_2ases (H_2-evolving N_5-N_{10}-methlenetetrahydromethanopternin dehydrogenases).[42-44] [Fe]-H_2ases catalyze the uptake of H_2 to reduce a methenyl-tetrahydromethanopterin (methylene-H_4MPT). These H_2ases were originally discovered in methanogenic *Methanothermobacter marburgensis*.[43] A homolog from *Methanocaldococcus jannaschii* was crystalized, revealing the active site of this unusual H_2ase binds two CO ligands at an octahedral iron site (Figure I-2).[45] Surprisingly, the iron appears to remain redox neutral, transferring a hydride to reduce methenyl-H_4MPT^+ methylene-H_4MPT.

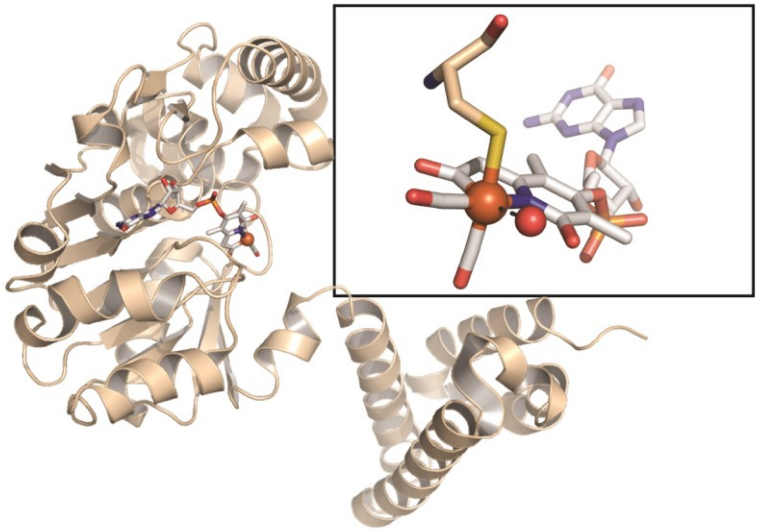

Figure I-2. Structure of Fe-H_2ase from *Methanocaldococcus jannaschii* determined to 1.75 Å (PDB entry: 3F47). Inset reveals active site of the [Fe]-H_2ase consisting of a Cys residue, two CO molecules, pyridol-GMP and a coordinated water from solvent.

Structure and function of [NiFe]-H_2ases

As deduced from the discussion of H_2 metabolism, [NiFe]-H_2ases are diffused across microbial communities. The minimal core of the [NiFe]-H_2ase consists of a catalytic subunit that incorporates a Ni-Fe(CO)$(CN)_2$ cofactor with additional Fe-S cluster binding motifs for electron transfer (Figure I-3).[46] [NiFe]-H_2ases reversibly react with oxygen, leading to considerable interest in [NiFe]-H_2ase-based biotechnological applications. While commonly described in the literature as H_2 uptake biased, [NiFe]-H_2ases have diverse catalytic activities, highlighted above.

Phylogenetic analysis of large data sets of [NiFe]-H_2ase sequences have led to a classification of [NiFe]-H_2ases, consisting of four different groups. Group 1 H_2ases are membrane-bound and energy transducing, coupling the oxidation of H_2 to electron

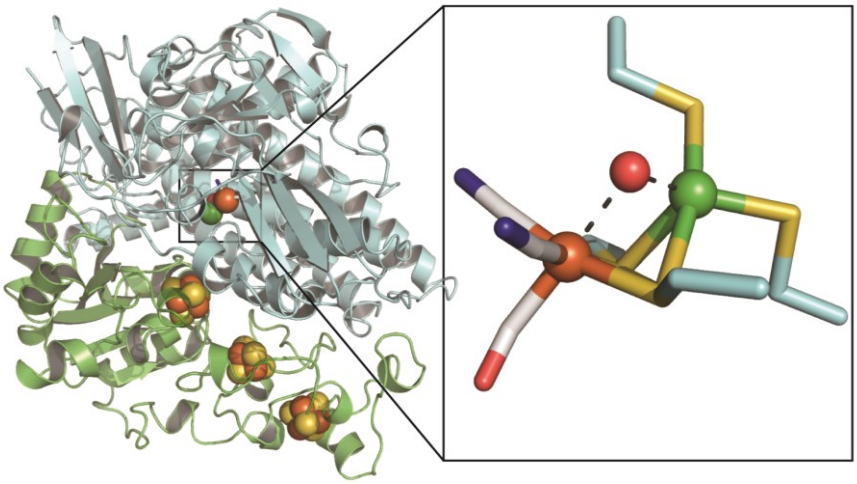

Figure I-3. Structure of [NiFe]-H_2ase from *Desulfovibrio gigas* (PDB entry: 2FRV). All [NiFe]-H_2ases identified to-date are heterodimeric, with one subunit encoded Fe-S clusters (green) and the other housing the catalytic subunit (blue). Inset reveals the catalytic site made up of a Ni atom (green sphere) coordinated by four Cys residues, two of which bridge to an Fe atom (orange sphere). The Fe contains one CO and two CN^- ligands. A bridging H_2O (red sphere), likely a hydroxide, is modeled.

transport phosphorylation. Group 2 H_2ases contain soluble uptake hydrogenases found in cyanobacteria and specialized sensory H_2ases that act as signal transducing components. Group 3 H_2ases are found in archaeal and bacteria species. This group consists of complex subunits and often called bidirectional; the catalytic direction *in vivo* is highly sensitive to the cellular environment. Lastly, group 4 H_2ases are multisubunit and membrane bound. These are typically utilized *in vivo* for H_2 production coupled to oxidation of another substrate, similar to *Ec*PFL.[3]

Significant interest in H_2ase interactions with O_2 have led to a greater understanding of O_2 inactivation and the identification and characterization of H_2ases that retain activity after O_2 exposure, so-called O_2-tolerant enzymes. Initial reports with

[NiFe]-H_2ases indicated O_2 exposure caused formation of an inactive species that required long incubations under H_2 before activity returned.[47] Two spectroscopically distinct species are formed. A quickly recovering "ready" Ni-B, and a slowly reactivating "unready" Ni-A arise from O_2 exposure. Structural studies led to models in which the Ni-B and Ni-A states resulted from hydroxide and peroxide molecules bound to the Ni ion, respectively.[46] Hypotheses to improve O_2 tolerant H_2ases included limiting access of O_2 to the active site and somehow avoiding the formation of Ni-A. Structural and modeling studies identified gas channels that connected the active site with the surface of the protein.[46] Remarkably, mutations designed to constrict the hydrophobic channel did result in increased O_2 tolerance.[48] Recently, *Re*MBH was found to oxidize H_2 in O_2.[49] Reports first circulated that this increased O_2 tolerance was due to limited O_2 diffusion to the active site;[50] however, spectroscopic studies indicated an exclusive formation of Ni-B and an apparently never-before characterized [Fe-S] species.[51]

Two structural reports, published in quick succession, elucidated the determinants for the remarkable O_2 tolerance of this class of [NiFe]-H_2ases (Figure I-4).[35,52] *Re*MBH is attached to the cytoplasmic membrane and consists of a large subunit containing the active site, and a small subunit that contains three Fe-S cluster centers that function in electron transfer. Traditional [NiFe]-H_2ases contain [4Fe-4S] clusters ligated by four cysteine residues (Figure I-3). In contrast, *Re*MBH contains a specialized cluster ligated by six cysteine residues, where one sulfide ion is replaced by two thiols, leading to [4Fe-3S] cluster (Figure I-4b). This unusual ligation scheme appears to facilitate two redox transitions within a narrow redox window – transitions unlikely for typical [4Fe-

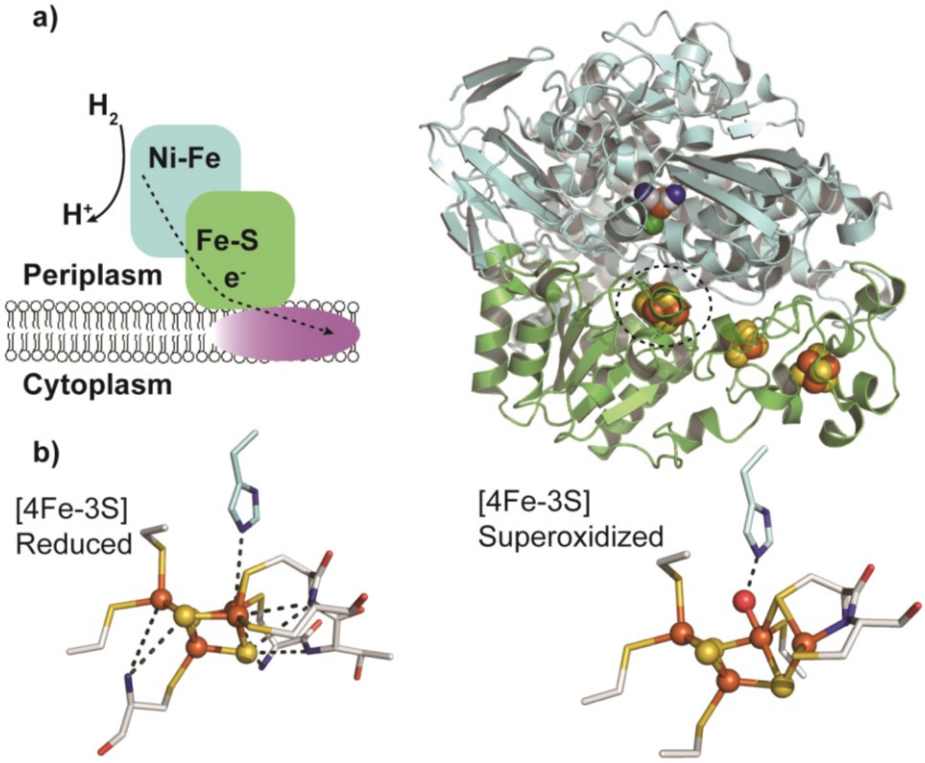

Figure I-4. Schematic depiction and structure of O_2-tolerant *Re*MBH. (a) *Re*MBH consists of a [NiFe]-H_2ase subunit (cyan), an Fe-S cluster containing subunit (green) and an integral membrane subunit (magenta). The proximal [4Fe-3S] is circled. (b) The proximal [4Fe-3S] displays redox-dependent structural changes. The Fe atoms are ligated by all thiol (sulfides and thiolates), whereas the superoxided the Fe atoms are ligated by a peptide amide and a water molecule. Adapted and reprinted by permission from Macmillan Publishers Ltd: Nature, Frielingdorf, S *et al*, 2014.

4S]-clusters.[53] Upon O_2 binding, four electrons are quickly passed directly to [NiFe] site to completely reduce O_2 to water,[54] thus avoiding Ni-A formation. Recent evidence suggests that the [NiFe] site provides one electron, while proximal and medial clusters donate two and one electrons, respectively.[55] Although electron flow is "uphill" thermodynamically to the [NiFe] site, electron transfer rates are efficient because the overall reaction (reduction of O_2 to water) is much more thermodynamically

"downhill."[56] This MBH has been used in a fuel cell, oxidizing H_2 at the anode, at ambient O_2 concentrations.[57]

Structure and function of [FeFe]-H_2ases

[FeFe]-H_2ases (previously known as Fe-only H_2ases) are mostly found in strict anaerobic eubacteria, such as fermentative bacteria (*Clostridium*, *Thermotoga*, *Ruminococcus*) and sulfate reducers (*Desulfovibrio*), and occasionally in eukaryotes, including some anaerobic protozoa and green algae (*Chlamydomonas*). [FeFe]-H_2ases have been given the name HydA, with a number to indicate the genomic context.[58,59] High-resolution X-ray crystallographic data now exits for representative bacterial H_2ases *Clostridium pastueranium* HydA-1 (*Cp*I) and *Desulfovibrio desulfuricans* HydA (*Dd*) as well as algal *Cr* (Figure I-5). For most bacterial HydA enzymes, a variable length N-terminal domain, called the F-domain, that contains a chain of Fe-S clusters. These clusters are spaced ~12 Å apart, which is ideal for facile electron transfer, and lead from the surface to the active site. The H-cluster active site is contained within the C-terminal core, and is an extended six iron core. The H-cluster consists of a typical [4Fe4S] cluster with a bridging cysteine ligand coordinating an additional two iron subsite ($2Fe_H$). The $2Fe_H$ contain two low spin irons (distal and proximal Fe, named according to proximity to the [4Fe-4S] cluster), each coordinated by biologically toxic CN^- and CO ligands. Along with a bridging CO, the $2Fe_H$ is also bridged by dithiolate ligand. This unique ligand has only recently unequivocally been demonstrated to be an azadiothiolate,[60] and the bridgehead N is positioned to act as a catalytic base for catalysis.[7]

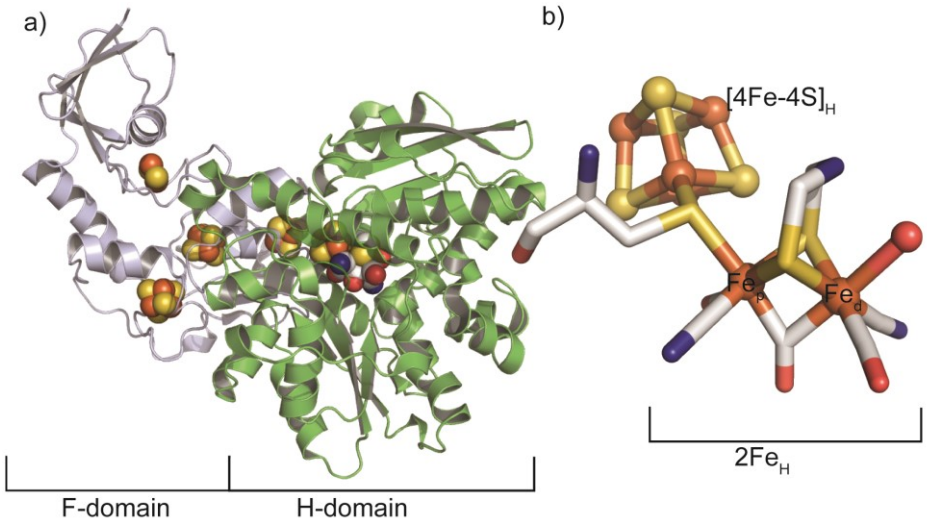

Figure I-5. Structure of *Cp*I (PDB entry: 3C8Y). A) Overall fold of [FeFe]-H_2aes *Cp*I with minimal H-cluster domain colored green and ferredoxin(F)-domain in grey. B) Active site of *Cp*I consisting of $[4Fe\text{-}4S]_H$ and $[2Fe]_H$. The $[2Fe]_H$ consists of a two irons coordinated by CO, CN and a unique azadithiolate. The irons are named according to proximity to the $[4Fe\text{-}4S]_H$, proximal (Fe_p) and distal (Fe_d). Fe_d is modeled with a terminal water.

[FeFe]-H_2ases are quite modular in domain architecture. Based on the structure of *Cr*HydA1, the core catalytic domain is called the H-domain. This domain is comprised of all the cysteines required to coordinate the H-cluster as well as amino acids that produce second-shell interactions: P1, TSCCPxW; P2, MPCxxKxxE; and P3, ExMACxxGCxxGGGxP (Figure I-6).[3] Canonical H-domains contain a span of ~350 residues with these strictly conserved motifs, represented in the structures mentioned above. Some identified homologs have extended H-domains up to 800 residues. Substitutions within these motifs, or cases where a motif is absent, are considered non-canonical H-domains, as in the case of NAR proteins.[61] Many [FeFe]-H_2ases contain additional, accessory domains. A variable length F-domain is the most common domain found in [FeFe]-H_2ase homologs, exemplified in structures of *Cp*I and *Dd*. A multitude

of other accessory domains have been identified, including many hydrogenase fusion proteins, and highlight the modular nature of [FeFe]-H_2ases in strict anaerobes. Attempts to separate HydA homologs into distinct phylogenetic groupings have failed, likely due to variability of additional domains.[2,3,6]

Monomeric H_2ases can be considered the most classical in regards to both *in vitro* and *in vivo* function. For example, the structurally characterized *Cp*I and the well-studied *C. acetobutylicum* (*Ca*) HydA are both monomeric and found in the cytoplasm.[7] Both are astonishingly active enzymes, with *Cp*I catalyzing H_2 evolution at 5500 U/mg protein and H_2 oxidation at 24,000 U/mg protein (one U is defined as 1 μmol H_2 produced or consumed per min)[62] and *Ca*HydA exhibits comparable activity. The ratio

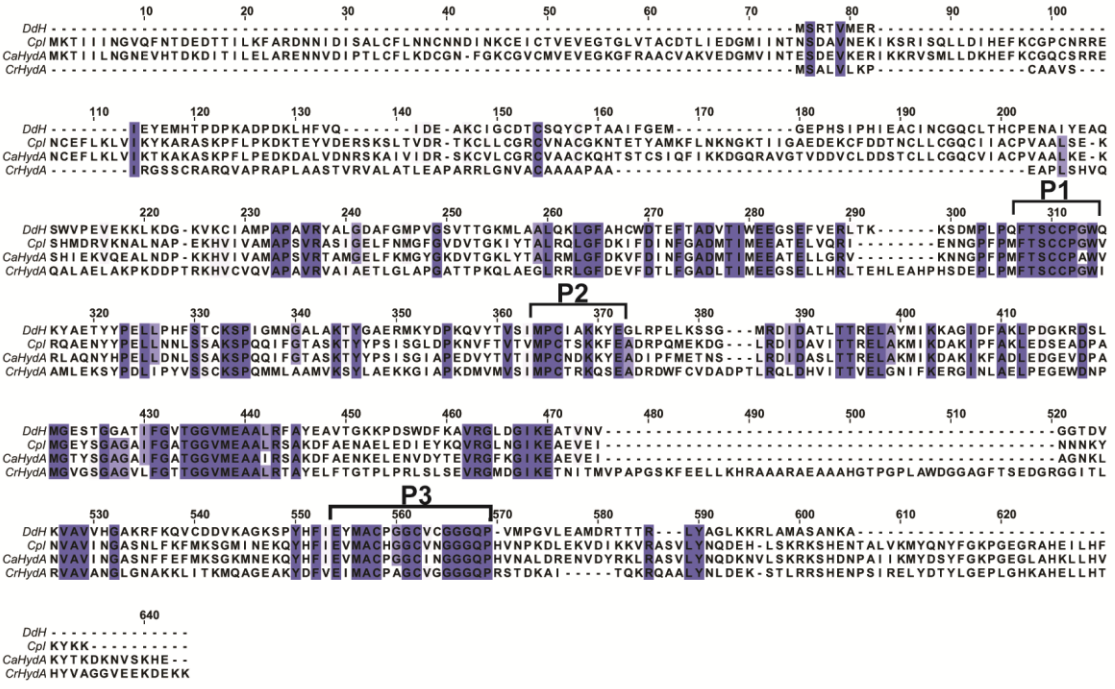

Figure I-6. Sequence alignment of classical [FeFe]-H_2ases studied in vitro recently. Residues are shaded according to a 90% sequence identity threshold.

of oxidation/evolution rates is 4.36). *Cp*I and *Ca*HydA are also extremely sensitive to O_2, where exposure to atmosphere O_2 results in a complete abatement of hydrogenase activity ($T_{1/2}$ < 5 min). *In vivo*, both these monomeric H_2ases function in relieving anaerobic fermenters of reducing equivalents by evolving H_2.[3] Results indicate these types of monomeric H_2ases accept low potential electrons from ferredoxins (Fdx), derived from oxidation of pyruvate to acetyl-CoA by pyruvate:ferredoxin oxidoreductase (E' -520 mV) – the final step of anaerobic glycolysis. *Cr*HydA is an additional 'classical' monomeric H_2ase from green algae. *In vitro*, *Cr*HydA behaves similarly to the clostridial H_2ases above, but its hydrogenase activity is somewhat lower (H_2 evolution, 1000 U/mg; H_2 oxidation, 1000 U/mg; oxidation/reduction, 10).[63,64] Additionally, *Cr*HydA appears confined to chloroplasts *in vivo*, utilized for redox balancing during dark fermentation or light driven H_2 production, where electrons from photosystem I and transferred to *Cr*HydA by a ferredoxin called PetF.[26,65,66] In summary, classical [FeFe]-H_2ases are monomeric, capable of both fast H_2 evolution and oxidation and function *in vivo* primarily in evolving H_2.

In contrast, *Dd* is heterodimeric and located in the periplasm. The structure of *Dd* revealed a 42 kD catalytic H-domain with two [4Fe-4S] clusters in the F-domain, appearing quite similar to *Cp*I. However, *Dd* structure also contained a small subunit consisting of an 11 kD 'belt' peptide surrounding the H-domain.[67,68] The exact function of the small subunit is unknown, but has been speculated to aid in signaling transport to the periplasm. *Dd* is suspected to be involved in promoting a H^+ gradient in the periplasm by oxidizing H_2. *Desulfovibrio desulfuricans*, interestingly, also encodes

[NiFe]-H_2ases.[3] Why sulfate reducers employ both hydrogenases also remains unclear. *In vitro*, *Dd* is highly active in H_2 production (V_{max}, 10,400 U/mg) and H_2 consumption (50,000 U/mg), yielding a ratio of activities similar to monomeric hydrogenases (4.8).[40] Additionally, *Dd* can be purified from the periplasm aerobically, meaning it retains activity in the presence of air. Aerobically purified *Dd* has much lower hydrogenase activity and requires reductive activation for maximal H_2 oxidation activity.[40] Somewhat surprisingly, if *Dd* is reduced with H_2, the resulting enzyme is now inactivated by oxygen at similar rates as monomeric H_2ases.

While monomeric and dimeric [FeFe]-H_2ases catalyze one of the simplest chemical reactions, more complicated reactions involving hydrogenases have been reported.[3,6,14] For instance, studies in cell lysates of fermentative anaerobes have been known to display NAD(P)H-dependent H_2 evolution.[69] Use of NAD(P)H (E' = -320 mV) is thermodynamically unfavorable for H_2 production (E' = -420 mV). Recently, heterotrimeric and heterotetrameric [FeFe]-H_2ases have been found to catalyze this reaction in *Thermotoga maritima*, *Ruminococcus albus* and *Acetobacterium woodii*, among others; these complexes are called bifurcating hydrogenases (BF-H).[15,22,23,59,70] BF-Hs are complexes of H- and F-domain containing proteins (α-subunit), a ß-subunit with a FMN cofactor and NAD(P)H binding site, ferredoxin binding γ subunit with an occasional fourth subunit. BF-Hs catalyze H_2 production (V_{max}, 7.8 U/mg) in the presence of reduced ferredoxin and NADH and H_2 oxidation in presence of oxidize ferredoxin and NAD^+ (V_{max}, 49.4 U/mg).[15] Surprisingly *in vitro*, BF-Hs show no activity in absence of pyridine nucleotides or ferredoxin. BF-Hs have been ascribed a role in

redox balance by conserving energy. In fermentative bacteria, BF-Hs are proposed to regenerate NAD^+ for glycolysis by evolving H_2,[15] whereas in acetogens BF-H's are speculated to oxidize H_2.[21] In addition to BF-Hs, acetogenic bacteria, such *A. woodii*, also encode for a heterotetrameric H_2-dependent carbon dioxide reductase (HDCR), catalyzing the reduction of CO_2 to formate using H_2.[21,71] HDCRs encode an [FeFe]-H_2ase with a H-domain and two [4Fe-4S]-clusters in the F-domain, a Mo/W-molybdopterin and two (or sometimes three) electron transfer subunits that bind [4Fe-4S]. Sequence alignments of both BF-Hs and HDCRs indicate a canonical H-domain.

Hidden within the annals of the scientific literature is *C. pasteurianum* hydrogenase II (*Cp*II), an [FeFe]-H_2ase with unusual catalytic properties. *Cp*II was first isolated and characterized from the cytoplasm of native source by Chen and co-workers in 1978.[72] *Cp*II appeared monomeric, was a poor H_2 production catalyst and from the preparation it was unclear of the protein bound Ni or simply Fe. Additional work demonstrably found the *Cp*II bound only Fe and S, thus it was an [FeFe]-H_2ase.[73] This enzyme catalyzed H_2 oxidation at rates comparable to *Cp*I and *Dd* (V_{max}, 34,000 U mg^{-1}), yet it catalyzed H_2 production at rates several orders of magnitude lower (V_{max}, 10 U mg^{-1}). *Cp*II also showed the same rate of O_2 inactivation as *Cp*I. Essentially, *Cp*II was a unidirectional H_2ase (oxidation/production ratio: 3,400).[74] Potentiometric titrations monitoring spin active species by EPR revealed the H-cluster had the same midpoint potential as *Cp*I (E_m = -400 mV). However, the two [4Fe-4S] clusters within the F-domain of *Cp*II had significantly increased (more oxidizing) potentials (E_m = -180 and -300 mV) than similar clusters of *Cp*I (E_m = -420 mV).[75] Based the large differences in

potentials of electron transfer centers and the active site, *Cp*II was proposed to be a unidirectional [FeFe]-H_2ases because it appeared thermodynamically predestined for H_2 oxidation only. No sequence information was known at the time of discovering *Cp*II and no structure was determined. Additionally, no *in vivo* function was ever assigned for this unique [FeFe]-H_2ase.

As the cost of complete genome sequencing as diminished, new insights have been gained into the diversity, distribution, and most importantly, the function of hydrogenases in strict anaerobes.[2,3,5,6,10,14,76] Several bioinformatic surveys of hydrogenases have further implanted the idea that H_2 metabolism is quite complex. Many anaerobes apparently encode multiple putative copies of [FeFe]-H_2ases (as many as seven).[6,14] A survey of clostridrial hydrogenases revealed the C-terminal additions with annotated chemical activity, such as rubrerythrin-like, glutamate synthase-like, carbon-monoxide dehydrogenase-like, etc (Figure I-7).[5,14] Rubrerythrins are diiron proteins almost exclusively found in anaerobic bacteria believed to be involved in reducing H_2O_2, and perhaps O_2, in reactive oxygen species defense systems (See *Anaerobes and the problem with oxygen*). Glutamate synthases are proteins that use NADH or reduced ferredoxins with co-substrates glutamine and α-ketogluturate to produce two glutamates.[77] [FeFe]-H_2ase fusions to a PAS domain, which often function to sense some signal,[70,78] have also been identified. The H-domain of sequences with a PAS domain has been mentioned in several studies to be non-canonical.[70] These protein fusions have yet to be investigated *in vivo* or *in vitro*. Additionally, hydrogenase-like sequences have been identified in higher eukaryotes, including humans.[6] These genes

appear to encode a H-domain like gene product, but lack many cysteines important to H-cluster binding. This gene product in humans has been demonstrated to localize to the nucleus and interact with prelamin A, thus the name NarF.[79] A similar Nar gene is speculated to be involved in cytosolic Fe-S biosynthesis in higher eukaryotes.[80,81]

The diversity of [FeFe]-H_2ase domain architectures and large variations of activity undercuts the general consensus that [FeFe]-H_2ases function primarily in H_2 production pathways. The large swath of activities highlights the need for a broader understanding of [FeFe]-H_2ase function *in vivo* and better fundamental understanding of the protein framework's role in tuning active site chemistry.

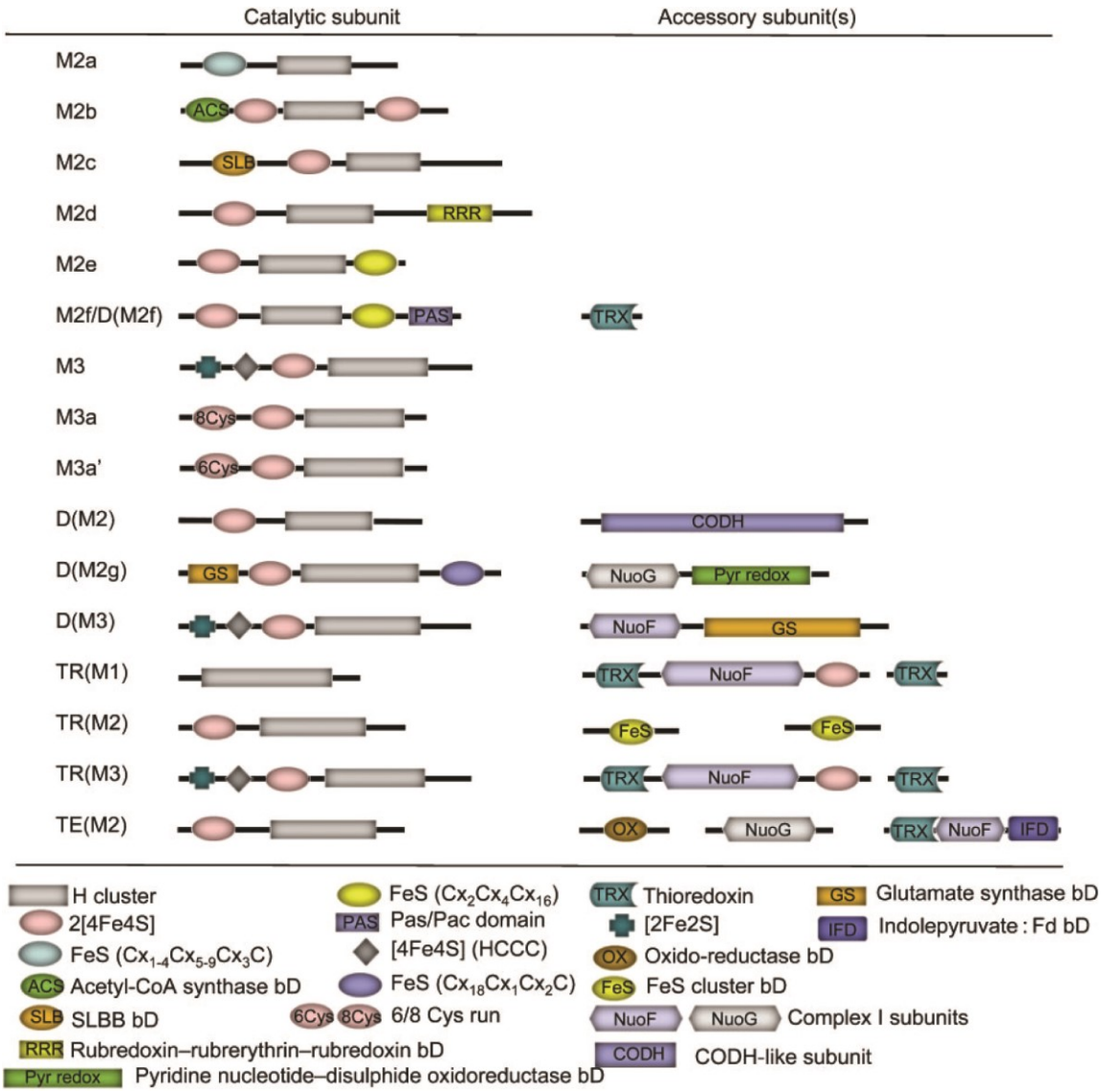

Figure I-7. Cartoon depictions of modular domains of clostridial [FeFe]-H_2ases. M, Monomeric; D, dimeric; TR, trimeric; TE, tetrameric; bD, binding domain; Fd, ferredoxin; CODH, carbon monoxide dehydrogenase. Republished with permission of Microbiology, from The surprising diversity of clostridial hydrogenases: a comparative genomic perspective, Calusinka, M, Happe, T, Joris, B, Wilmotte, A,156, 2010; permission conveyed through Copyright Clearance Center, Inc.

Electrochemistry of hydrogenases

Protein film electrochemistry (PFE) has become the nouveau technique in the study of H_2ases. This technique consists of absorption of a protein onto an electrode, forming a protein film. PFE's pioneering work was accomplished by Armstrong in 1999 using *Allochromatium vinosum* [NiFe]-H_2ase, where it was shown that pmol of enzyme dried on an electrode resulted in observable currents dependent upon substrate.[82] Since that initial study, PFE has become the nouveau technique for H_2ase research, supplanting traditional dye-based assays.[7,83] Indeed, PFE even showed dye-based assays could be rate-limiting for H_2ase catalysis.[82] The power of PFE is beyond simply 'breaking' older assays, because in concert with other techniques such as EPR, IR and X-ray crystallography, significant progress has been made in understanding the mechanism of H_2 turnover, formation and catalytic rate of intermediate states, as well as the mechanisms of inhibition for O_2, CO_2 and even product (H_2).[7]

Basics of protein film electrochemistry

PFE is a dynamic electrochemical technique where an observed electric current generated by an enzyme on an electrode corresponds to electron transfer and/or catalytic activity.[84] It is well established that redox active enzymes can be absorbed,[82,85] or in some cases covalently attached,[86,87] on electrode surfaces and exhibit fast electron transfer rates from electrode to protein (interfacial). A signal (current) is observed as electrons exchange between the electrode and the enzyme. The catalytic turnover is directly controlled by variations in electrode potential.[83]

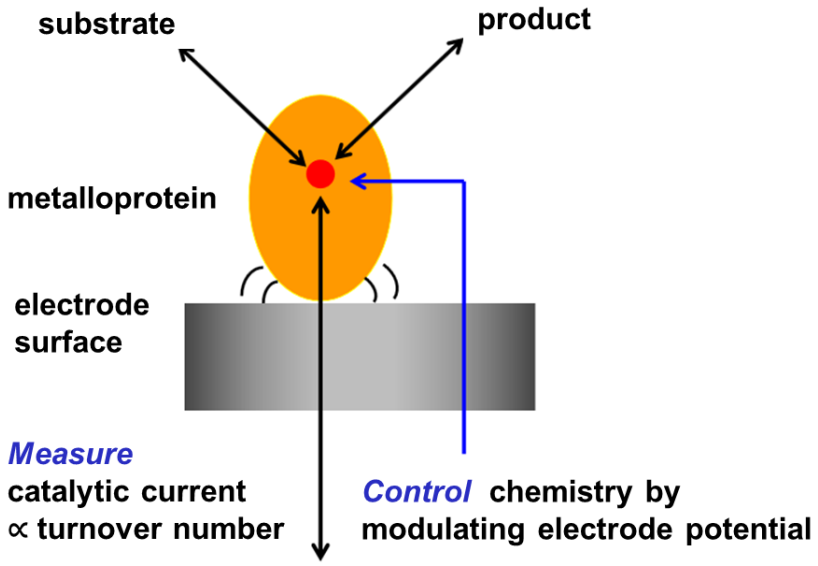

Figure I-8. Model for protein film electrochemistry. Reprinted and adapted with permission from Vincent, KA, Parkin, A, Armstrong, FA, Chem Rev, 107 (10), 2007. Copyright 2007 American Chemical Society.

A simple model for observed currents is given by Figure I-8. Once a protein is deposited onto an electrode, some amount of the protein will be oriented for direct interfacial electron transfer; this correctly oriented enzyme is called electroactive enzyme. It is assumed, then, that fast electron transfer can occur from the electrode to the protein. Electrons must traverse across the interface, through the protein relay and ultimately to active site for catalysis. If mass transport is minimized by rotating the electrode, then the observed current corresponds to electrocatalysis. In this general scheme, it is assumed that the observed rate of electrocatalysis depends solely on a chemical step and not electron transfer into the active site.[7]

A measured current is proportional to the inherent activity of the enzyme. For H_2ases, the potential as which current can be observed is given by the Nernst equation,

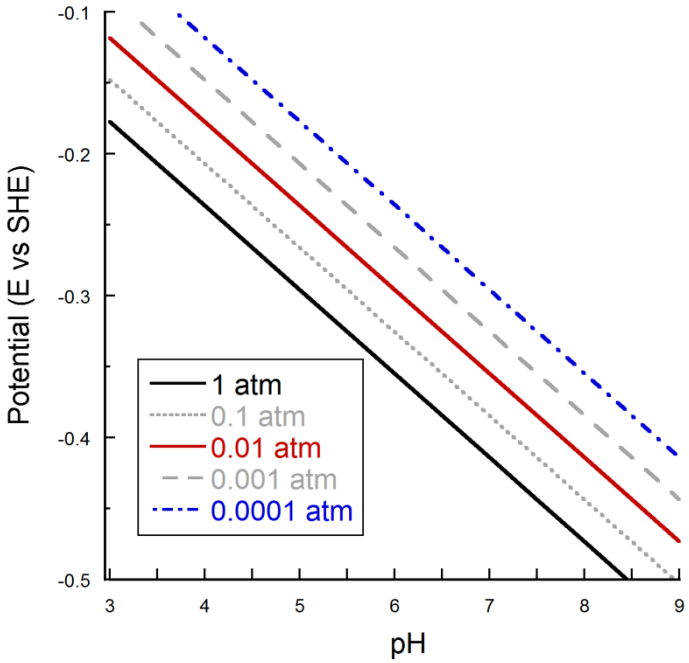

Figure I-9. pH dependence of the $2H^+/H_2$ equilibrium potential as dictated by the Nernst equation.

where T is the absolute temperature, R is the gas constant, n is the number of electrons transferred (2), and $p(H_2)$ is the partial pressure of H_2. The standard reduction potential ($E^0 = 0$ V) is the standard hydrogen electrode (SHE), under 1 bar of H_2, pH 0 and 25 °C.

$$2H^+ + 2e^- \rightarrow H_2 \quad E^\circ = 0 \text{ V} \qquad (\mathbf{1})$$

$$E_{eq} = E^0 + \frac{2.3RT}{nF} \log(H^+)^2/p(H_2) \qquad (\mathbf{2})$$

Under typical laboratory experimental conditions (pH 7 and 1 atm H_2), the reduction potential of this reaction is -414 mV vs SHE.[88] This so-called equilibrium potential ('E_{eq}') varies considerably by pH and partial pressures of H_2 (Figure I-9).[89] For instance, under low H_2 partial pressure (0.01%) – a pressure likely encountered by bacteria[83] –

NADH (E' = -320 mV) can drive H_2 evolution (E_{eq} = -296 mV). Thus, the direction of electron flow (measured current) is dictated by the Nernst equation.

PFE allows for the possibility of thermodynamically pushing the enzyme by varying potential. Under cases when the current maximizes (plateaus), the observed current is equal to k_{cat} as described by (equation **3**)

$$k_{cat} = i_{lim}/nFA\Gamma \qquad (3)$$

where k_{cat} is turnover frequency of the enzyme, i_{lim} is the maximum catalytic current measured, n is the number of electrons transferred, F is Faraday's constant, A is the area of the electrode and Γ is the coverage of the electrode by electroactive enzyme.[83] Several important points arise from this equation. First, the magnitude of observed current depends on the area of the electrode *and* amount of electroactive enzyme. The amount of enzyme that orients correctly on the electrode is not controllable, making direct current comparisons between experiments nearly impossible. Additionally, direct comparison of the observed current to a turnover number is incorrect, unless Γ is measured. Electrode coverage can only be measured under nonturnover conditions, i.e. measurement of redox potentials of bound cofactors. This is often difficult to measure due to weak or broad currents.[83] Though activity per enzyme (k_{cat}) is often not able to be reported, qualitative comparison of relative electroactive properties of enzymes on electrodes has been extremely insightful.

In a general sense, the current is a direct measure of the rate of catalytic electron transfer and reflects the enzyme's turnover rate. Negative currents indicate cathodic processes, i.e. reduction of H^+, and positive currents indicate anodic processes. The

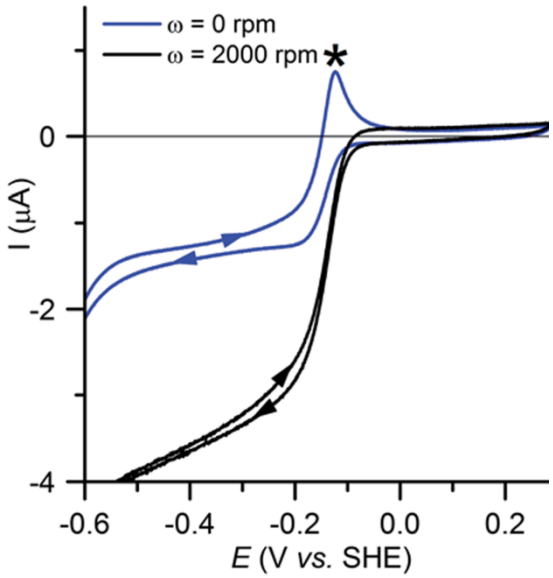

Figure I-10. A comparison of voltammograms of *Ec*Hyd-1 at pH 3.0 recorded under stationary (blue) and rotating conditions (black). Reproduced from Ref 101 with permission of The Royal Society of Chemistry. dx.doi.org/10.1039/C3EE43652G

importance of minimizing mass transport by quickly rotating the electrode should not be overlooked. A stationary electrode with a hydrogenase film will exhibit a negative current at potentials more negative than E_{eq} (Figure I-10).[90] However, as the scan continues to more oxidizing conditions, H_2 produced from the negative potential regions builds up at the electrode surface. This H_2 is then re-oxidized as the potential crosses E_{eq}, leading to a sharp oxidizing current.[89] When the electrode is rapidly rotated, this peak is not observed since the evolved H_2 is dissipated to the bulk solution. A comparison of stationary and rotating CVs confirms that the measured currents are due to H_2ase electrocatalytic activity.

Protein film electrochemistry with hydrogenases

Cyclic voltammograms (CVs) have provided great insight into functional differences between [NiFe]- and [FeFe]-H_2ases.[7,34,91-95] A comparison of electrocatalytic CVs of two [NiFe]-H_2ases (Hyd-1 and Hyd-2) and two [FeFe]-H_2ases (*Cr*HydA and *Ca*HydA) is provided in Figure I-11. Immediately, it is clear that Hyd-1 catalyzes of H^+ reduction while Hyd-2 does not at pH 6 and 1 atm 100% H_2. The [FeFe]-H_2ases display much faster H^+ reduction under the same conditions, highlighting the first difference between these hydrogenases: [NiFe]-H_2ases display a large product (H_2) inhibition of H^+ reduction ($K_i^{H_2}$) while [FeFe]-H_2ases are mostly unaffected by the presence of a H_2

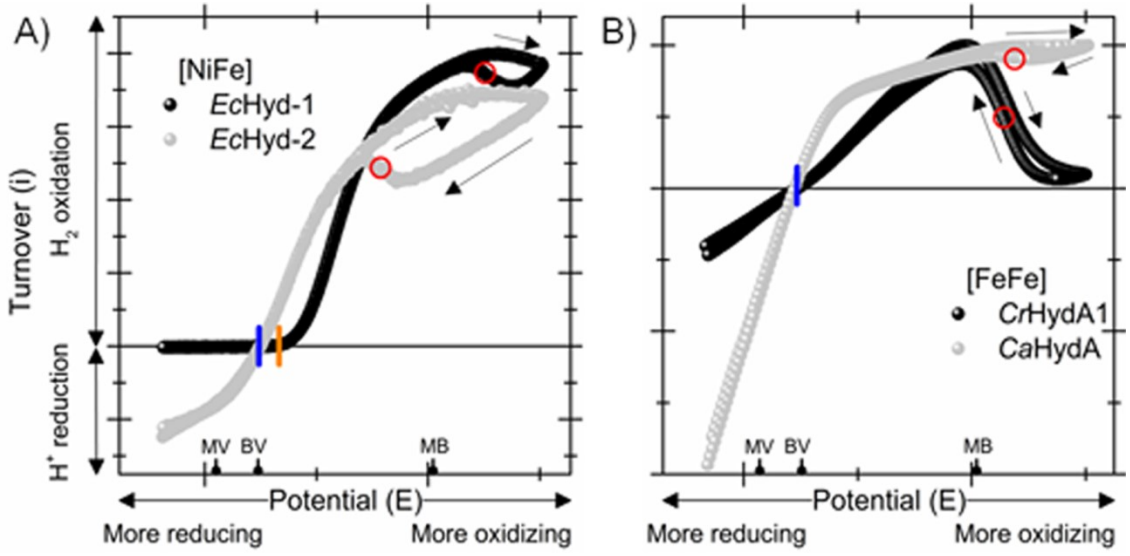

Figure I-11. Electrocatalytic CVs of various hydrogenases adsorbed onto a PGE electrode. A) [NiFe]-H_2ases Hyd-1 and Hyd-2 with 10% H_2 atm, pH 6 and scan rate = 1 mV s^{-1}. B) [FeFe]-H_2ases *Cr* and *Ca*HydA with 100% H_2 atm, pH 6 and scan rate = 5 mV s^{-1}. Blue lines indicate E_{eq} and orange line indicate the onset potential. Red circles indicate oxidative inactivation. Arrows indicate the scan direction. Redox potentials of commonly used redox dyes are indicated on the bottom (methyl viologen, MV; benzyl viologen, BV; methylene blue, MB). Reprinted with permission from Armstrong, FA, Evans, RM, Hexter, SV, *et al*. *Accounts of Chemical Research* **49** (2016).

atmosphere.[96,97] The currents for Hyd-1, *Cr* and *Ca* immediately change sign on either side of E_{eq}, indicating that electrocatalysis is reversible.[90] Hyd-2, though, is not reversible and requires overpotential (see below). All H_2ases exhibit fast H_2 oxidation. Interestingly, [FeFe]-H_2ases, in contrast with [NiFe]-H_2ases, display sizable losses in current as the pH_2 is lowered. Numerous electrocatalysis studies have shown NiFe]-H_2ases have much lower K_m values for H_2 than [FeFe]-H_2ases.[96] Lastly, all H_2ases display loss of current (inactivation) under high (oxidizing) potentials.[34,83,85,94] This inactivation appears mostly reversible. Upon scanning in the reverse direction of the CV, the fast H_2 oxidation current can be recovered. The inflection point of this reactivation is defined as the switch potential (E_{switch}).[84] The inactivated species formed by [NiFe]- and [FeFe]-H_2ases are presumed to be analogous to inactivated species formed in potentiometric experiments, i.e. Ni-B and $H_{ox}^{inactive}$, respectively.[34] It must be pointed out, however, that E_{switch} is a model dependent apparent reduction potential that can be controlled experimentally by kinetics (scan rate) and pH.[7,85] Thus, direct comparisons between electrocatalytic and potentiometric species are difficult. Qualitatively, E_{switch} defines the potential window in which H_2ases are active (Figure I-12).[83] Standard [NiFe]- and [FeFe]-H_2ases display electrocatalysis from -400 mV to ~ +50 mV, while the O_2-tolerant hydrogenase (Hyd-2) oxidize H_2 from -280 mV to +100 mV.[7,34] Thus, despite the overpotential of Hyd-2, it remains active in a larger redox window than standard H_2ases, emphasizing the physiological roles and potential niches of these enzymes.[83]

Comparison of the potential dependence of electrocatalysis of H_2ases additionally reveals the limitation of redox dyes (Figure I-11). For instance, dithionite-reduced methyl viologen (MV; E' = -450 mV) is a commonly utilized reagent to probe H_2ase reactivity. Most H_2ases display electrocatalytic H^+ reduction that is potential dependent – more negative potential equates to a faster rate. Oxidized MV has also been used as electron sink for H_2 oxidation. Due to its potential, it is only effective at basic pH values. So, use of MV does not reveal the 'true' or maximal catalytic rate, but instead can act as a bottleneck for catalysis. Additionally, methylene blue (MB, E' = +16 mV) is another dye often used for H_2 oxidation. Often, this potential is at or near the inactivation range observed in PFE.

Electrocatalytic CVs also have exposed the H_2ase's catalytic bias. It is important

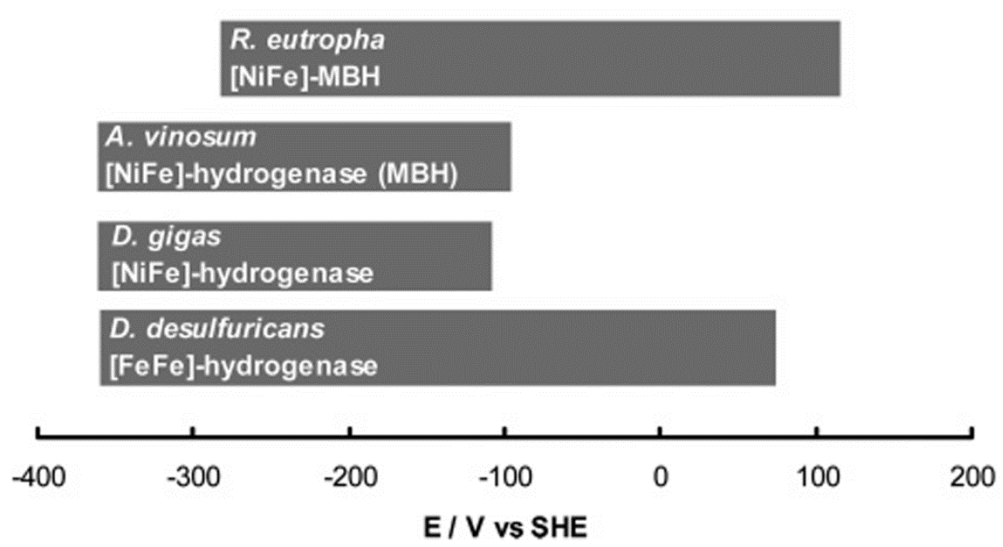

Figure I-12. Potential window for H_2 oxidation activity for four different H_2ases, defined as the range from E_{onset} to oxidative inactivation. Vincent, KA, Parkin, A, Armstrong, FA, Chem Rev, 107 (10), 2007. Copyright 2007 American Chemical Society.

to note here that a true catalyst cannot affect the ratio of products and reactants (thermodynamics) of a reaction, but instead only affects the rate of catalysis. Bias here reflects a comparison of observed currents under different electrode conditions. Catalytic bias is now defined as the ratio of maximally observed electrocatalysis, although the role of H_2 in affecting different types of H_2ases must be accounted. As stated above, [FeFe]-H_2ases display marginal effects of H^+ reduction in the presence of H_2 ($K_i^{H_2}$) and relatively high $K_m^{H_2}$; the opposite is true for [NiFe]-H_2ases. Thus, the bias of hydrogenase appears to be dictated by apparent H_2 affinity and inhibition constants.

When the potential of the electron transfer relay of H_2ase is near E_{eq}, then the H_2ase is capable of reversible catalysis and requires minimal overpotential ($E_{chem} - E_{eq}$).[98] This is true for all [FeFe]-H_2ases studied by electrochemistry so far, as well as the standard [NiFe]-H_2ases. However, if an electron relay center or active site potential lies significantly far from the E_{eq}, then the enzyme will preferentially operate in a particular direction. The catalytic bias depends on the difference between E_{chem} and E_{eq}.[90] This was shown to be true for the O_2-tolerant Hyd-2. Hyd-2 contains the special distal [4Fe-4S] cluster that is required for O_2-tolerance. The distal cluster has an especially high redox potential (+160 mV), which thermodynamically poises Hyd-2 to oxidize H_2.[89]

Biosynthesis of hydrogenases

Biosynthesis of these organometallic catalysts has garnered much attention, and tremendous progress has been made in understanding the maturation processes. The [NiFe]-H_2ase follows a complex assembly process, utilizing at least six accessory hyp proteins (HypA-F) and an endopeptidase.[47,99] HypA binds and inserts Ni, while HypC binds Fe and is the scaffold for synthesis of the diatomic ligands. Carbomylphosphate (CP) is the precursor for CN^- biosynthesis, requiring CP transferase (HypF) and HypE, which ultimately generates a transferrable thiocyanate moiety to HypC. The remaining hyp genes are involved in scaffolding, proteolysis, and structural rearrangements. In contrast, H-cluster specific maturation machinery appears quite simple, requiring only three proteins.[100]

The genes required to fully mature [FeFe]-H_2ases were initially discovered in green algae by screening for mutants that lacked the ability to produce H_2.[101] The gene responsible for the loss of H_2 evolution was mapped to the gene *hydEF*. Upstream of *hydEF* was an additional gene, *hydG*. The *hydEF* fusion gene contains two distinct domains that are homologous to two trenchant prokaryotic domains, *hydE* and *hydF*. These gene products were proposed to be the sole maturation factors for [FeFe]-H_2ase. Functional studies in *E. coli* demonstrated that the homologous three *Clostridium acetobutylicum* (*Ca*) gene products are required to mature [FeFe]-H_2ases: HydE, HydF, and HydG.[101,102] HydE and HydF belong to the radical SAM superfamily, that is they contain a [4Fe-4S] cluster binding domain with an open coordination site where S-

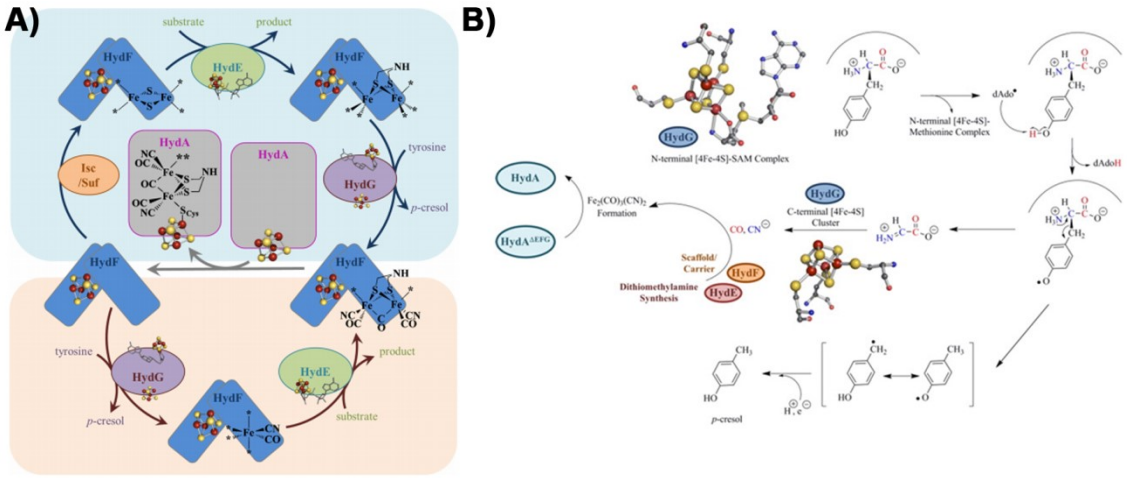

Figure I-13. Cartoon depiction for biosynthesis of $[2Fe]_H$. a) Two possible pathways for [FeFe]-hydrogenase maturation. In both pathways, the maturation process involves synthesis and assembly of the 2Fe subcluster of the H-cluster, followed by insertion of this 2Fe subcluster to generate the active hydrogenase. JBIC, H-cluster assembly during maturation of the [FeFe]-hydrogenase, 19 (6), 2014, 747-757, Broderick, JB, with permission from Springer. b) Formation of the Fe synthon by HydG. Reprinted from BBA – Molecular Cell Research, 1853 (6), Peters, JW, Schut, GJ, Boyd, ES, Mulder DW, Shepard, EM, Broderick, JB, King PW, Adams, MWW, [FeFe]- and [NiFe]-hydrogenase diversity, mechanism, and maturation, 1350-1369, Copyright 2015 with permission from Elsevier. http://www.sciencedirect.com/science/journal/01674889

adenosyl methionine can bind as a ligand. HydF has clear GTP- and [Fe-S]-binding domain that are both essential for complete maturation.

H-cluster maturation first requires a preformed [4Fe-4S],[103] which is synthesized by general iron-sulfur cluster biosynthetic machinery (Figure I-13). Based on recombinant studies where HydF was spectroscopically (FTIR and EPR) demonstrated to bind a $[2Fe]_H$-like species, HydF is proposed to be the scaffold protein upon which the nascent $[2Fe]_H$ is synthesized.[104] HydG uses radical SAM chemistry to cleave tyrosine to *p*-cresol and an intermediate, suggested perhaps to be dehydroglycine.[105,106] Recent studies by the Britt group have demonstrated that two turnovers of Tyr lead to the

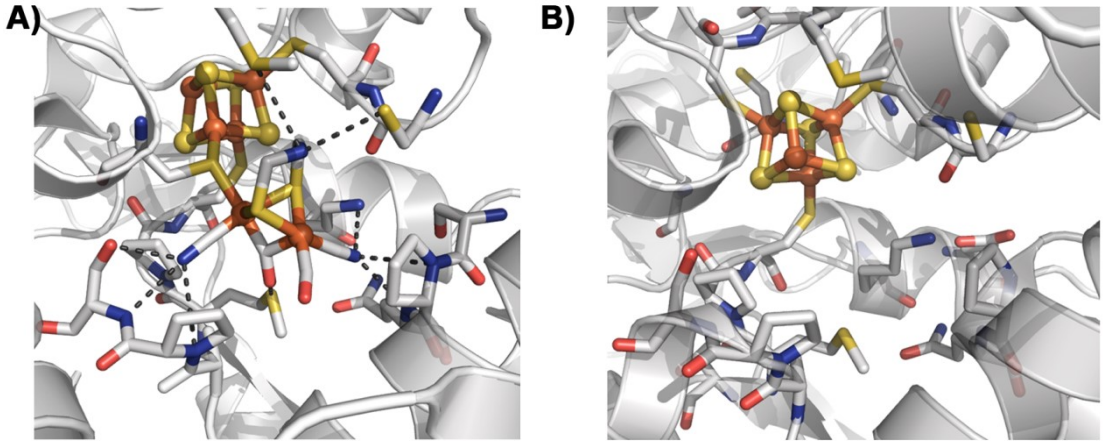

Figure I-14. Structures of *Cp*I reveal the structurally rigid H-cluster binding residues. A) *Cp*I reconstituted semi-synthetically with azadithiolate (PDB entry: 4XDC). B) *Cp*I expressed in the absence of maturation factors, CpI^{IM} (PDB entry: 4XDD). Overall RMSD: 0.33 Å.

formation of an $Fe(CO)_2(CN)$ synthon that can be transferred to mature the hydrogenase.[107-109] HydE, then, must be involved in generation of the azadithiolate ligand.[110] Little evidence exists as to the substrate or mechanism, but cysteine is believed to be the substrate for HydE,[111-113] and HydE has been shown to form carbon-sulfur bonds from 1,3-thiazolidines using a carbon-based radical species.[114] To complete H-cluster synthesis, the newly synthesized $[2Fe]_H$ on HydF is transferred intact to HydA.[60,115,116]

Recently, synthetic mimics have been shown to fully activate immature forms of [FeFe]-H_2ases (H_2ases containing the [4Fe-4S] cluster but lacking the $[2Fe]_H$). A seminal study found HydF could be loaded with a synthetic mimic of the $[2Fe]_H$ and activate an [FeFe]-H_2ase to wild-type levels.[60] A follow-up study found that HydF was not required for maturation, the synthetic mimic was capable of spontaneously activating the hydrogenase.[117] Additional studies have demonstrated the active site of [FeFe]-H_2ase

accommodates various other synthetic mimic derivatives, but these other mimics cannot achieve full activation. Structures of the immature form of *Cr*HydA, along with *Cr*HydA reconstituted with a few synthetic mimics illustrate the active site of the protein is rigid, adopting the same conformation regardless of the presence of a $[2Fe]_H$ (Figure I-14).[118] These results demonstrate the essential role of the dithiolate central bridgehead nitrogen and the importance of the protein framework in dictating the conformation of the diiron site.

Anaerobes and the problem with molecular oxygen

Microbes display disparate abilities to survival in oxygen, a fact that defines the microbial world. Figure I-15 displays a cartoon depiction of a pond, displaying the types of niches microbes evolved to proliferate within.[8,119] The surface of the water and soil is saturated with air, giving rise to O_2 concentrations, maximally, of ~0.28 mM. Organisms found here not only survive in oxygen, but also thrive, utilizing the oxidizing power of O_2 to drive their metabolism. Oxygen has limited access to sub-surface environments, and microbes found here are either facultative anaerobes, meaning their metabolism can harness the oxidizing power of O_2 or can switch to other metabolic routes under O_2-deplete conditions, or microaerophiles.[8] Microaerophiles are an interesting set of microbes because they require O_2 for survival, but can only tolerate sub-saturating air conditions (5-10% O_2). Microbes found here are aerobic, requiring oxygen for survival. Knallgas bacteria, such as *Ralstonia eutrophia*, which encodes for a O_2-tolerant [NiFe]-H_2ase, requires both O_2 and H_2 for growth.[33] Toward the bottom of the pond, anaerobic microbes such as *Clostridia* and *Desulfovibrio* species rarely encounter O_2, so they lack

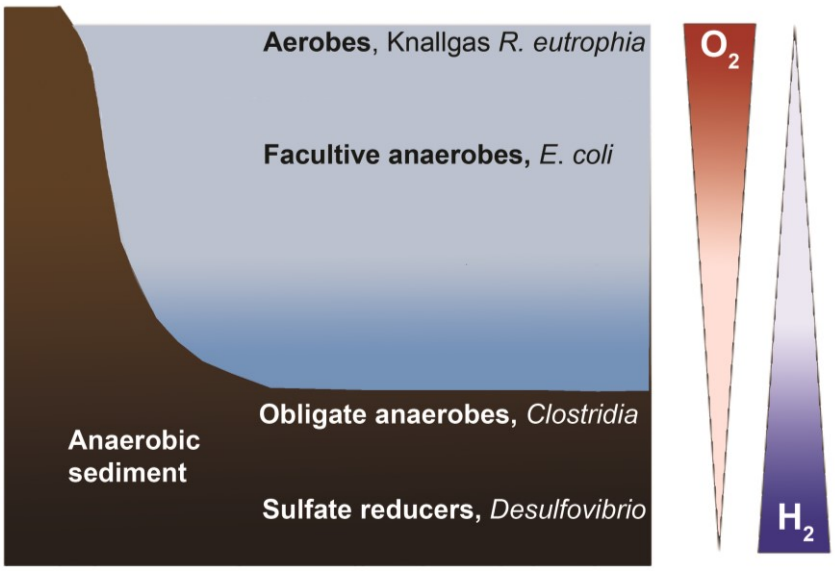

Figure I-15. Schematic depiction of the distribution of various microbes in within pond waters. Adapted from ref 49. Copyright 2005 American Chemical Society.

metabolic pathways to utilize O_2.[8] These obligate anaerobes utilize other pathways for metabolism, such as fermentation (see section above), sulfate reduction, etc. Thus, H_2 concentrations can be considered inverted to O_2. Additionally, it appears H_2 generated from fermentative anaerobes is 'recycled' by organisms in aerobic zones.[4,5] In turn, organic detritus generated from the surface eventually sinks to the bottom of the pond where it is degraded by various pathways to generate H_2 again. The general scheme of the anaerobic pond seems to be mirrored in other microbial communities, such as the gut of higher mammals[11,70] and soil sediments.[8]

These anaerobic microbial communities are under constant threat of exposure to oxygen. Storms may disturb hypoxic waters, exposing air-sensitive microbes. The gut of higher eukaryotes, such as humans, contains a large ecological community of commensal, symbiotic and pathogenic microbes. These microbes must be capable of

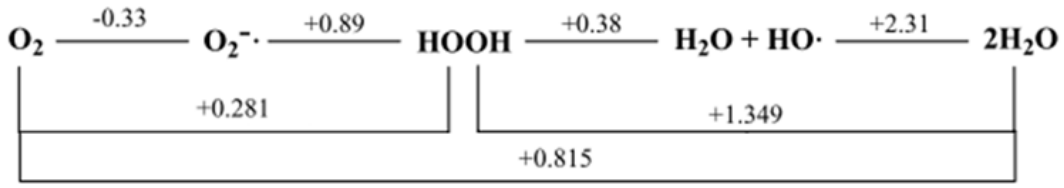

Figure I-16. Reduction potential diagram for oxygen at pH 7. The units are in V vs SHE. Adapted from ref 125.

surviving O_2 exposure long enough to encounter a host organism.[120-122] For instance, strict anaerobes were once thought to completely die upon oxygen exposure, but studies with the human pathogen *Clostridium perfringens*[123] or the commercially valuable *Clostridium acetobutylicum*[124] have found these anaerobic bacteria can survive up to 10% O_2.[122] Clearly, environmental stresses have resulted in mechanisms for increased survivability of strict anaerobes to oxygen.

To ascertain the mechanisms by which anaerobes tolerate O_2, it is necessary to understand why O_2 is inherently toxic to these microbes. Oxygen is a potent two and four electron oxidant (Figure I-16).[125,126] However, these reactions do not occur readily. Ground state oxygen contains two unpaired electrons in its frontier molecular orbital. Both electrons have the same spin state, meaning ground state oxygen is triplet (S=1, $2S$+1). Triplet oxygen is kinetically stable because most biomolecules are singlet species (S=1), and reactions between triplet and singlet molecules are spin disallowed. Oxygen can act as an oxidant to form various reactive oxygen species (ROS), but this requires a source of low potential electrons.[126] Unfortunately for fermentative anaerobes, they are virtual cornucopias for ROS formation, where their metabolism utilizes PFOR (E' = -

450 to -510 mV, see above section) ferredoxins (E' = -440 mV), reduced flavin nucleotide cofactors, as well as various reduced metal centers and thiols.[14,23,120,127] Oxidation of these reduced species disrupts anaerobic metabolism, can damage protein cofactors (especially Fe-S clusters) and lead to oxidatively modified biomolecules. H_2O_2 is also a potent one electron oxidant, forming the hydroxyl radical.[125] $OH^{\cdot}$ reacts at near diffusion controlled rates with virtually all biomolecules, stressing it as the most potent ROS.[126] H_2O_2 can also form hydroxyl radical from reaction with superoxide, called the Haber-Weiss reaction (reaction **4**), which is iron-mediated and actually the sum of the Fenton reaction plus reduction of ferric iron with superoxide (reactions **5**-**6**).[128] In summary, exposure of O_2 to anaerobes results in the formation of highly reactive ROS (called ROS stress) that are capable of oxidatively modifying any biomolecule such as DNA or protein, which decreases growth rates, increase rates of genomic mutagenesis and, potentially, cellular death.[126]

$$H_2O_2 + O_2^- \rightarrow O_2 + OH^- + OH^{\cdot} \quad (\mathbf{4})$$

$$Fe^{2+} + H_2O_2 \rightarrow Fe^{3+} + OH^- + OH^{\cdot} \quad (\mathbf{5})$$

$$Fe^{3+} + O_2^- \rightarrow Fe^{2+} + O_2 \quad (\mathbf{6})$$

A few misconceptions arise that must be taken into account in regards to defense against ROS stress. First, it was initially proposed, and to some extent still propagated, that strict anaerobes lack any ability to defend against ROS stress. Many strict anaerobes are quite capable of surviving limited exposure to oxygen, exemplified above. Lastly,

although aerobes and facultative anaerobes employ O_2, incomplete reduction of O_2 to water is common. The steady-state concentration of H_2O_2 in *E. coli*, in fact, has been measured in the low micromolar range,[129,130] and higher aeration rates increased the H_2O_2 concentration.[121] This latter effect is also seen in higher eukaryotes, when the respiratory complex decouples to form ROS,[131] either by mutations in the electron transport chain or upon exposure to increased oxygen concentrations, such as those in hyperbaric chambers.[132] Mechanisms to avoid oxygen stress, then, must be central to survival of all forms of life, especially anaerobes.

ROS scavenging enzymes across life appear mostly conserved, and enzymes from aerobes and facultative anaerobes have been well characterized.[127,133] These microbes employ a large suite of ROS detoxification of enzymes including catalases, superoxide dismutases and peroxidases. Catalase was first identified in 1900 in tobacco leaf extracts from observations that addition of H_2O_2 resulted in the formation of trace amounts of O_2.[134] Catalase catalyzes reaction **7** at near diffusion controlled rates.[133]

$$2\,H_2O_2 \rightarrow H_2O + O_2 \qquad (7)$$

These enzymes use heme iron as a cofactor, though non-heme dimanganese proteins are found in aerobic microbes that lack heme biosynthetic machinery.[135] Superoxide dismutases (reaction **8**) are identified by the metal cofactor, containing either a Cu/Zn

$$2O_2^- + 2H^+ \rightarrow H_2O_2 + O_2 \qquad (8)$$

site or Fe, Mn or even Ni (monomeric).[136] Lastly, peroxidases are much broader class of ROS scavenging enzymes (reaction **9**).[122] These enzymes typically use the reducing

$$H_2O_2 + NADH + H^+ \rightarrow 2H_2O + NAD^+ \qquad (9)$$

power of NADH (-320 mV) to reduce H_2O_2. Peroxidase enzymes range from peroxiredoxins (as known as akyl hydroperoxide reductase, Ahp), thiol peroxidases, glutathione peroxidase and cytochrome *c* peroxidase. Peroxiredoxins, in particular, appear to be efficient H_2O_2 scavengers (k_{cat}/K_m, 10^7 M^{-1} s^{-1})[137] using two surface exposed cysteine thiols to catalyze hydrogen peroxide reduction.

In comparison, anaerobes use even more enzymes to protect themselves from the stresses of ROS (Figure I-17).[128,138] Generally, most anaerobes are deemed catalase negative.[139] The evolutionary logic must be that O_2 is deleterious to healthy anaerobes, so there is not much need to regenerate O_2. However, genome searches of anaerobes reveal the presence non-heme, dimaganese catalases (KatBs).[135] The role of these non-heme catalases is currently vague, but it appears some sporulating microbes line their cell walls with KatB homologs in their vegetative state.[140-142] Likely, KatB serves to minimize excessive formation of mutagenic hydroxyl radicals while the organism is in the spore state. Anaerobes also encode for SODs.[12,128] Along with the above mentioned peroxidases, anaerobes also employ superoxide reductase (SOR) and rubrerythrins (reaction **10** and **8**, respectively).These two proteins are specific to anaerobes and are often located on the same operon, indicating they may act in concert.[143]

$$e^- + 2H^+ + O_2^- \rightarrow H_2O_2 \qquad (10)$$

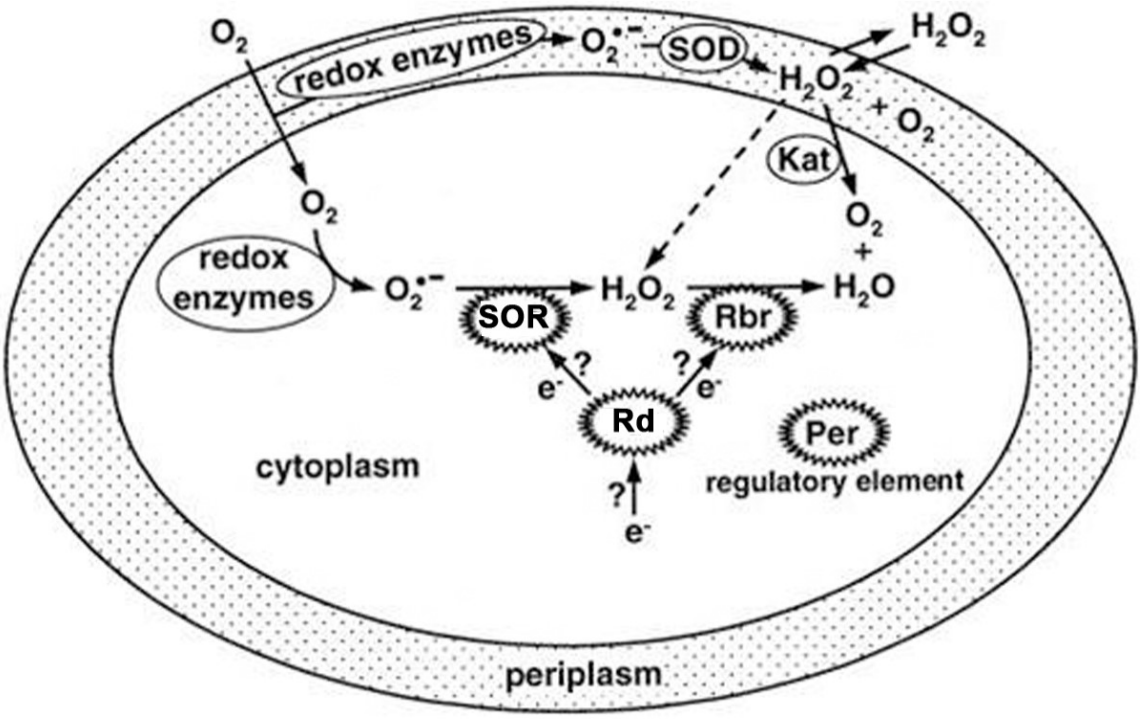

Figure I-17. Reactive oxygen species enzyme response system in anaerobic bacteria. Reprinted with permission from ref 128.

SORs and rubrerythrins are hypothesized to act in concert to scavenge for adventitiously generated superoxide and fully reduce this species to water.[144] SOR is a non-heme, mononuclear enzyme that uses a $(His)_3Cys$ ligation scheme at the metal center. This enzyme has been shown to be effective at scavenging for superoxide,[128,136,145-148] and thus represents a bona fide ROS enzyme. Rbr, on the other hand, uses a diiron site for NADH-dependent H_2O_2 reduction, but its catalytic parameters *in vitro* call its role as a ROS scavenger into question.[122] Rbrs will be enumerated in further detail below. A recent study in the obligate anaerobe *Bacteroides thetaiotaomicron* confirmed this large coalition of ROS scavenging enzymes was utilized *in vivo*. Additionally, the authors provided data that Rbr and SOR act as the first

line of defense against ROS. Upon further ROS stress, SOD and various other catalases, including peroxiredoxins, supplant SOR and Rbr as primary ROS scavengers.[121]

Rubrerythrins

Rubrerythrins (Rbr) were first isolated from the sulfate-reducing, obligate anaerobe *Desulfovibrio vulgaris* strain Hildenborough (*Dv*) by purification of a dark red fraction from cell-lysate.[149,150] Subsequent spectroscopic characterization identified two distinct iron sites: a mononuclear iron site ligated by four cysteines most similar to rubredoxin; and a non-heme diiron site similar to hemerythrin.[150,151] Thus, the name rubrerythrin is a contraction of the two different iron sites. Rubredoxins (Rds) are small, monomeric proteins characterized by a tetrahedral $Cx_2C_{x30}Cx_2C$ iron binding site that is dark red/ruby in color (hence the name). Rds found as fusions, as in the original *Dv* Rbr, contain a shortened $Cx_2Cx_{12\text{-}20}Cx_2C$ motif. Generally, it is believed that Rds function in electron transfer.[128] Conventional Rbr proteins contain an N-terminal diiron center and a C-terminal Rd. Additional reverse rubrerythrins (revRbr) have been annotated and characterized, where the Rd found at the N-terminus of the diiron site.[152] Anaerobic bacteria typically encode for 'classic' and reverse Rbrs, often with multiple copies, underscoring the importance of Rbrs in anaerobes. Sequence comparison suggested the diiron site *Dv* Rbr was ligated differently than hemerythin, which contains four histidines and two carboxylates.[153] Indeed, Mössbauer spectroscopy of ^{57}Fe grown *Dv* identified the diiron site to be most consistent with four carboxylates and two histidines, similar to μ-oxo diiron proteins methane monooxygenase (MMO), ribonucleotide reductase subunit 2 (RNR-R2) and ferritin.[151]

Despite this similarity to other μ-oxo diiron proteins, Rbrs share no ability to activate O_2 via a ferryl intermediate (MMO and RNR-R2) or assemble large oligomers for iron storage; instead, most studies indicate Rbrs function as ROS scavengers.[154-156] Rbrs were first demonstrated *in vivo* in ROS detoxification in the microaerophilic *Spirillum volutans* (*Sv*). A mutant strain of *Sv* that was H_2O_2 resistant exhibited high levels of NADH-dependent peroxidase activity, and a Rbr homolog was expressed in surprisingly high levels.[157] Complementation experiments, where *Dv*Rbr was over-expressed, increased growth rate and viability following exposure to external H_2O_2.[143] Moreover, Rbr homologs in *P. gingivalis*[158,159] and *C. acetobutylicum*[160-163] were induced upon aeration, apparently controlled by *perR*, an ROS response gene in anaerobic bacteria.[124] Lastly, Rbr was shown to be vital for function of the O_2-sensitive nitrogenase in cyanobacteria species *Albaena sp*. upon ROS stress.[164]

Initial reports suggested Rbrs catalyzed multiple reactions, including ferroxidase, O_2-activation and pyrophosphatase activity, but only ROS – namely H_2O_2 and O_2 – reduction have been reproducibly observed *in vitro*.[154-156] Reaction of Rbr with H_2O_2 causes oxidation of the irons within the diiron center, resulting in reduction of substrate to H_2O. To complete the catalytic cycle, two additional electrons must be transferred from the reduced rubredoxin domain to the diferric site. The (now) oxidized rubredoxin can then be reduced by some external reductant pool.

If the function of Rbr truly is in H_2O_2 scavenging, then anaerobic bacteria must have a pathway to catalytically regenerate reduced irons sites within Rbr. Toward that end, rubredoxin has been proposed to act as a reductant for the iron sites of Rbr since Rd

genes are adjacent to Rbrs within the genomes of both *Pyrococcus furiosus* (*Pf*) and *Dv*.[165] Incorporation of a separate reduced Rd protein for assays of Rbr-catalyzed H_2O_2 reduction resulted in k_{cat} estimates of greater than 2000 min^{-1} (reaction **11**).[154] A

$$2Rd_{red} + H_2O_2 + 2H^+ \rightarrow 2H_2O + 2Rd_{ox} \qquad (\mathbf{11})$$

complete *in vitro* peroxidase system (reaction **7**) has been proposed where electrons are derived from the NADH pool. A flavin-dependent oxidoreductase is required to transfer the electrons from NADH (via hydride) to a separate, one electron accepting Rd. Coulter and coworkers first demonstrated that *Dv*Rbr was capable of catalyzing the peroxidase reduction (**3**), with an estimated k_{cat} of 300 min^{-1}.[154] The oxidoreductase, BenC, was shown to influence the catalytic rate, nearly saturating at 5 μM. This steady-state system, while promising, yields a k_{cat} that is an order of magnitude slower than the rates measured from a reduced Rd pool only. The authors suggested use of non-physiological electron donors was responsible for the difference in catalytic rates.[154] Additional Rbr homologs were shown to catalyze reaction **7** using other flavin-containing enzymes, such as ferredoxin:$NADP^+$ reductase (FNR) from spinach and the now annotated NADH:Rd oxidoreductase (NROR), have found that other Rbr homologs are capable of catalyzing the peroxidase reaction.[164,166,167] A complete *in vitro* system has been developed that allows for measurements of steady-state kinetics using NADH (Figure I-18). Measured rates for reaction (**7**) vary between homologs of Rbr, with reported specific activities from 1 – 50 μmol NADH consumed min^{-1} mg $protein^{-1}$.[164,166,167] Reports of a K_m for H_2O_2 are scarce, but two values of 35 μM[167] and 2 mM[164] have been reported from *Pf* and a cyanobacterial species (Albaena), respectively. Additional Rbr

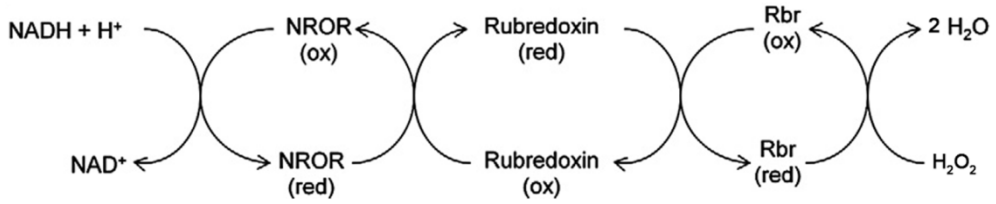

Figure I-18. Schematic for steady-state electron delivery to Rbr for peroxidase function. Reprinted from Journal of Bacteriology, 525, Mishra, S, Imlay, J, Why do bacteria use so many enzymes to scavenge hydrogen peroxide?, 145-160, Copyright 2012, with permission from Elsevier. http://www.sciencedirect.com/science/journal/00039861

peroxidase rates are only reported at a single H_2O_2 concentration, making direct comparison to k_{cat} difficult. Assuming the concentration of H_2O_2 is in fact saturating the Rbr active site (a large assumption), these rates are several orders of magnitude slower than the non-NADH coupled reaction. It should be noted that most NADH peroxidase assays only utilize a catalytic amount (0.5-1 μM) of Rd or oxidoreductase. These discrepancies between measured coupled assays and single-turnover experiments suggest that electron transfer into the diiron site is – or at least contributing to – the rate limiting step measured in steady-state experiments. Additional experiments where concentrations of substrate, Rd and flavin-containing proteins are varied will be necessary to better understand how Rbr functions in H_2O_2 reduction.

Reduction of O_2, in comparison, by Rbr is even less understood. Based on *in vivo* results and spectroscopic similarity to O_2-activating enzymes, Rbr was proposed to also function in reduction of O_2 completely to water. However, numerous attempts to confirm an oxidase function for Rbr have undercut this reaction as a possibility.[154] For example, incubation of reduced Rbr with air-saturated buffer show a slow reaction with O_2,

requiring several minutes for complete oxidation of Rbr.[154] Similar aerobic conditions with H_2O_2 included only required seconds. These results led to the suggestion that the proposed oxidase function of Rbr is artefactual.[128] However, a recent report of a revRbr from *C. acetobutylicum* indicated an increased oxidase rate in comparison to a classical Rbr called RubY. Additionally, over-expression of revRbr in *C. acetobutylicum* led to significantly increased growth tolerance to both O_2 and H_2O_2. Interestingly, revRbr, like conventional Rbrs, was shown to preferentially use H_2O_2 over O_2 as a substrate, despite the increased reactivity with O_2. The authors speculated that this rearranged domain architecture might improve electron transfer rates from the Rd domain to the diiron site.[152]

All Rbrs studied to-date adopt a homodimeric quaternary fold, which has now

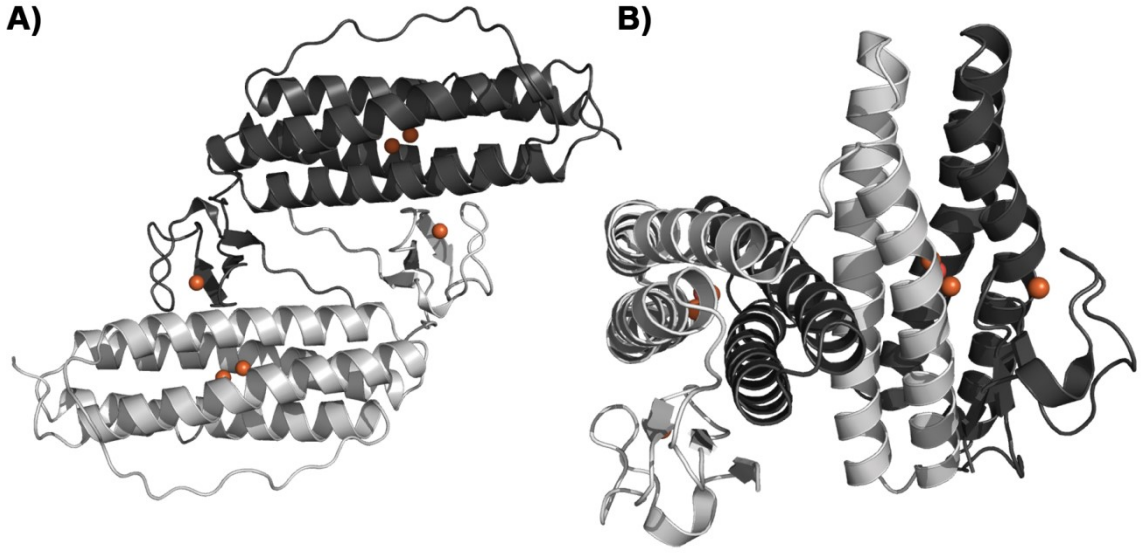

Figure I-19. X-ray crystal structures of *Dv*Rbr (A) and *Pf*Rbr (B) homodimer structures. The two subunits are colored as grey and black. Ferric iron atoms are depicted as orange spheres. PDB entry: 1RYT and 3MPS.

become an additional characteristic of Rbrs, and is reflected in various crystal structures of classical Rbrs from *DvH* and *Pf* (Figure I-19).[168-174] These structures contain an N-terminal four-helix domain containing the diiron site, and a C-terminal domain containing the Rd-like $Fe(Cys)_4$ site. In addition, the diiron and $Fe(Cys)_4$ sites are orientated to achieve a distance of 12-13 Å for efficient interdomain electron transfer (Figure 1-19).[128] Electron transfer between sites is presumably through-bonds since conserved aromatic residues are found between the two iron sites. While the distance between the Fe sites is maintained, the separation is achieved differently in the two structures. *Dv*Rbr adopts a 'head-to-tail' dimer that places the iron sites across the dimer interface within 12 Å (Figure I-19a).[174] A Rbr homolog that lacks Rd domains, called symerythrin, has this same core four-helix bundle fold.[168,175] In the *Pf*Rbr structure, the four-helix bundles containing the diiron site are domain swapped, meaning the bundle consists of two helical regions from both subunits.[169,170] The intersite distance for *Pf*Rbr is within a single subunit (Figure I-19b). Sulerythrin, a rubrerythrin-like homolog found in strict aerobes that only encodes for the four-helix bundle domain, also adopts this domain swapped dimer.[176]

From the first structure of oxidized Rbr, it was clear that the active site of Rbr differed significantly from other diiron proteins. As expected from numerous spectroscopic studies, an oxo-species was observed between the diferric site with two bridging carboxylates.[149,151,177-179] However, the structure also revealed an extra terminal glutamate ligand (Figure I-20; numbering according to PDB entry 3RYT) bound to Fe1.[174] This extra Glu ligand, called the seventh Glu, has no counterpart in O_2-activating

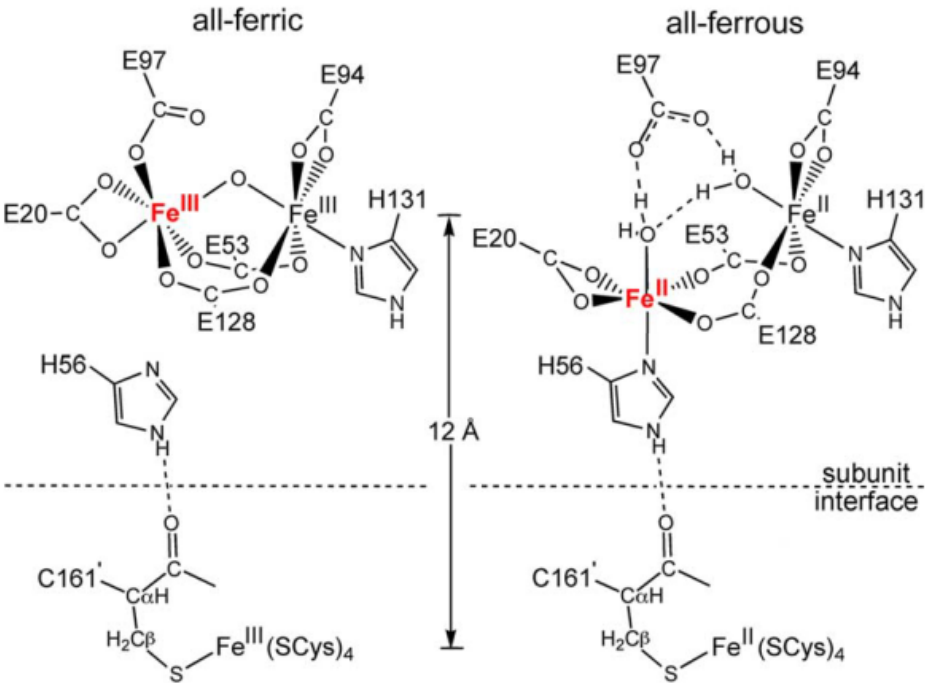

Figure I-20. Diagrams of Rbr active site based on all-ferric and all-ferrous structures. The redox toggling Fe is depicted in red. Reprinted from the Journal of Inorganic Biochemistry, 100, Kurtz, DM, Avoiding high-valent iron intermediates: Superoxide reductase and rubrerythrin, 679-693, Copyright 2006, with permission from Elsevier. http://www.sciencedirect.com/science/journal/01620134

enzymes and is now considered a hallmark motif for Rbr homologs.[128] The expected histidine (H56) is 4.2 Å away from the iron, too far to be considered a ligand. Subsequent structures of reduced (all ferrous) Rbr indicated that the seventh Glu was no longer a ligand to Fe1, and instead 'toggled' 1.8 Å to now be ligated by His56.[180] The protein backbone and His56 do not appear to indicate any redox-dependent movement. Only a bidentate glutamate (Glu20, Figure I-20, right) appears to move appreciably, essentially paralleling the movement of Fe1. The distance between Fe1 and Fe2 also increases considerably upon this redox toggle, from 3.3 Å to 4.0 Å, respectively, and the oxo-bridge is replaced by solvent molecules upon reduction. The redox-dependent

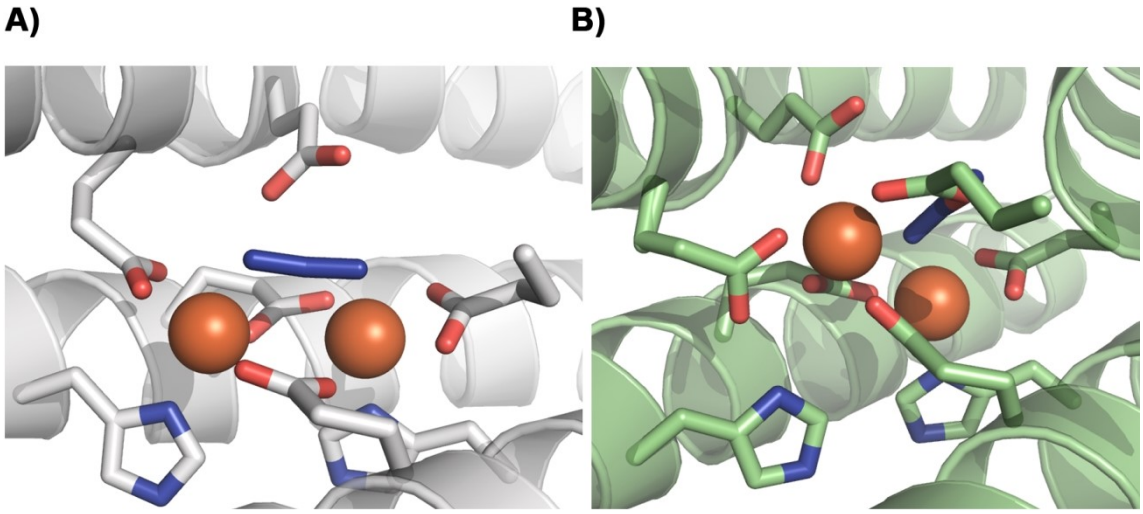

Figure I-21. Views of the diiron center of rubrerythrin and its homolog, symrerythrin, with azide bound. A) Azide binds μ,1-3 in the structure of diferrous *Dv*Rbr (PDB entry: 1LKP). B) Azide binds μ,1 in the structure of diferric symrethrin (PDB entry: 3SID).

movement was confirmed by advanced EPR techniques, and appears to occur at a mixed-valent state (Fe^{II}/Fe^{III}).[177] Co-crystallization of reduced Rbr with azide found this ligand to bind μ-1,3, replacing solvent molecules at the active site (Figure I-21a).[169,180] Another feature of Rbr is that the active site is highly solvent accessible, with two helices from the bundle creating essentially a coordinated solvent canyon. All of these features, including the redox toggling of Fe1 and solvent accessibility of the active site, are characteristic of Rbrs, and have been confirmed in other homologous structures. Additional crystallographic work with oxidized Rbr even indicated that synchrotron radiation was capable of photoreduction of the diiron site, and Fe1 stilled showed movement at 100K.[172] Interestingly, the structure of oxidized symerythrin in complex with azide finds the ligand binds μ-1 to the diferric site, replacing the oxo bridge (Figure I-21b).[168] The seventh Glu has two positions in the structure; either partial coordination

to Fe1 or rotated to interact with solvent. Combined, these results indicate that the Rbr active site is quite plastic, capable of redox and ligand dependent movements.

From these structures, one can reasonably assume that the Rd site is responsible for electron transfer to the diiron site, where H_2O_2 reduction occurs. Through-bond electron transfer has been inferred based on placement of aromatic residues between the two iron sites. Substitution of one Cys→Ser (presumably forming a $Fe(Cys)_3Ser$ site) caused a considerable decrease in the rate of (**7**). Additionally, Rbr substituted with Zn resulted in a complete abatement of reaction (**7**).[155] These experimental results support external reducing equivalents travel through the Rd iron site to the diiron center. The solvated canyon near the solvent exposed diiron site may contribute to the relatively sluggish reactivity with O_2 by essentially selecting for polar substrates. The surprisingly high reduction potential (E' > + 200 mV) can, at least, be rationalized by this highly solvent exposed active site and redox-dependent toggling of Fe1. The diferrous state reacts with H_2O_2 quickly (millisecond time scale), with no formation of higher oxidation states of iron, *i.e.* ferryl intermediates seen in MMO and RNR-R2, when diferric Rbr is incubated with additional substrate. Furthermore, E97A or E97F substitutions lead to significantly decreased reactivity of reduced Rbr and H_2O_2 (requiring minutes for complete oxidation of Rbr), highlighting the important role Glu97 plays in coordinating substrate.[155]

Based on these results, a mechanism has been proposed for Rbr (Figure I-22), starting at the reduced (diferrous state) due to the reduction potential of irons.[128,169] Substrate binds, displacing coordinating waters, and the seventh Glu has a stronger

interaction with one of the oxygen atoms of peroxide. Next, two electrons are transferred to peroxide (successive one electron transfers from the diiron center), concomitant with the Fe1 toggle to Glu97 and water release. The seventh Glu likely becomes protonated at this step, due to its strong interaction upon substrate binding. One electron is then transferred from the $Fe(Cys)_4$ site to the diiron site , likely forming a mixed-valent $Fe1^{III}$-$Fe2^{II}$ species. In the presence of external reducing equivalents, another electron transfer event from the Rd site can occur. Fe1 toggles back to His ligation, the bridging hydroxo is protonated and an additional water molecule binds in the now open diferrous active site to complete the catalytic cycle.[169]

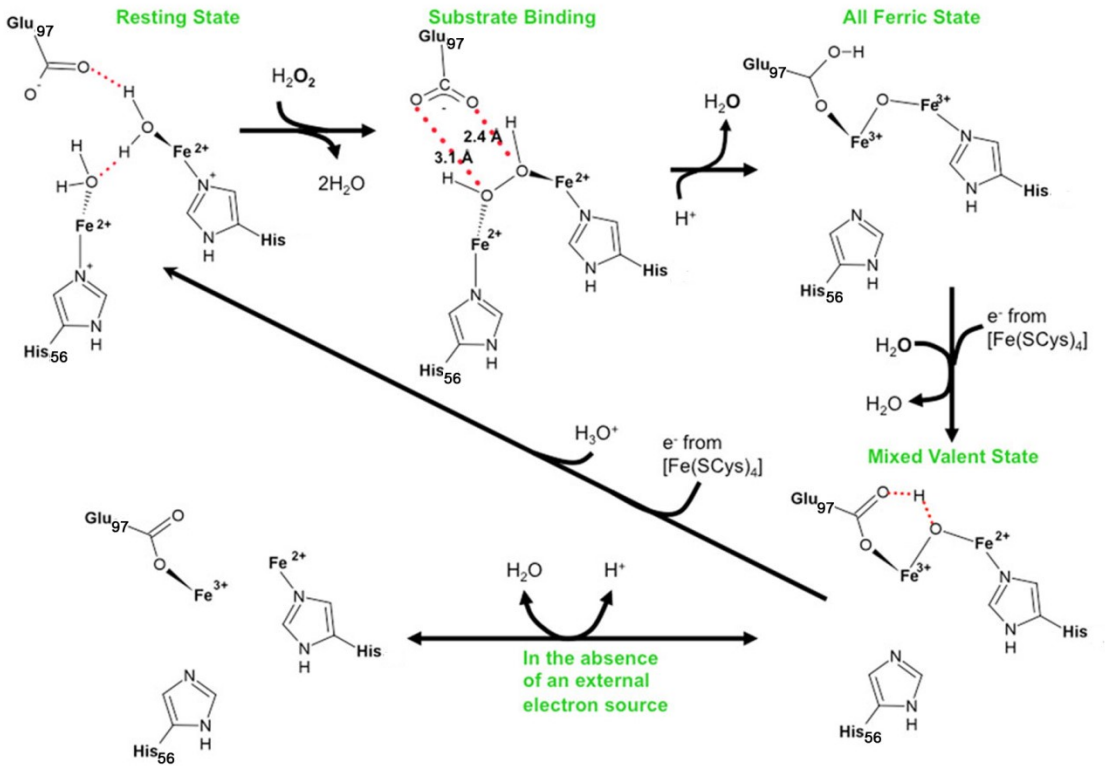

Figure I-22. Modified reaction scheme for rubrerythrins. Similar to Figure I-20, all the glutamate side chains have been removed for clarity, with the exception of those involved in redox toggling. Proposed hydrogen-bonding interactions are highlighted in *red*. The distances are based on the crystallographic models. Consistent with the proposed binding mode for peroxide, our data provide insight into the orientation of oxygen atoms in the strictly conserved glutamic acid side chain (E83 in PfRbr) relative to bound peroxide as well as evidence that the bridging oxygen atom in the mixed-valence state is indeed exchangeable. Reprinted from the Journal of Biological Inorganic Chemistry, A cryo-crystallographic time course for peroxide reduction by rubrerythrin from *Pyrococcus furiosus*, 16, 2011, 949-59, Dillard, BD, Demick, JM, Adams, MW, Lanzilotta, WN, copyright Journal of Biological Inorganic Chemistry with permission of Springer.

CHAPTER II

EXPERIMENTAL SECTION FOR SUBSEQUENT CHAPTERS

Experimental methods for Chapter III

Reagents and general procedures

Reagents and buffers were of highest commercial purity. DNA constructs were confirmed by sequencing (Gene Technologies Lab, TAMU). Cell cultures were grown in a 15 L bioreactor (ChemGlass Life Sciences) equipped with a pH controller that maintained pH 7.0 by titrating with 1 M KOH. Growth temperatures were sustained in a water bath by a water circulator (VWR).

All proteins were purified using an ÄKTAFPLC (GE LifeSciences) located inside a refrigerated anaerobic glovebox (mBraun, 10-14 °C, < 0.5 ppm O_2) and were manipulated in this anaerobic glovebox, unless otherwise stated. Soluble protein fractions were isolated by centrifugation at 20,000x*g* in anaerobic centrifuge tubes. Proteins were concentrated on preparative scale by a 50 mL pressurized Amicon (EMD Millipore) using Ar gas passed through an O_2 trap (Supelco, < 0.5 ppm O_2). Spin concentrators (30 kD MWCO, GE Lifesciences) were to concentrate proteins for spectroscopic analysis. All pH values are temperature-adjusted.

Cloning and protein expression

All cell lines and plasmids used are represented in Table II-1. The gene encoding *C. symbiosum hydY* (WP_044902140.1, GenBank ID: EGA94013.1) was codon optimized for *Escherichia coli* and synthesized (Life Technologies) with a TEV protease recognition site. The synthesized gene was cloned into pET28a (Novagen) using

Table II-1. Strains and plasmids used in this study.

Strains and plasmids	Relevant characteristics	Source or reference
Strains		
Lemo21(DE3)	pLemo21(DE3)	NEB
BL21(DE3)	BL21(DE3)	Invitrogen
Rosetta™2(DE3)pLysS	Express rare codons for *E. coli*	Novagen
Plasmids		
pHydY	pET28a/His_6-Tev-HydY	This study
pCTD	pET28a/His_6-CTD	This study
pNTD	pET28a/His_6-NTD	This study
p*Ca*I-*hydE*	pETDuet-1/*Ca*I-Strep	[102]
p*hydF-hydG*	pCDFDuet-1	[102]
p*NTD-hydE*	pETDuet-1/ His_6-NTD-Strep	This study

MEGAWHOP mutagenesis[181] between the 5' His_6-tag and XhoI sites, and the resulting plasmid (pHydY) was transformed into *E. coli* BL21(DE3) pLemo21 cells[182] for protein expression.

E. coli BL21(DE3) pLemo21 cells containing pHydY were grown aerobically (10L/min air) in LB supplemented with 30 μg/mL chloramphenical, 30 μg/mL kanamycin, 50 μM L-rhamnose, and 0.002% anti-foam B at 30°C. At OD_{600} of 0.6, 0.5 mM L-Cys, 0.5 mM $(NH_4)_2Fe(SO_4)_2$ and 0.4 mM IPTG was added to the culture. Cells were grown for an additional 16 hours at 20°C with an air flow of 2 L/min.

The sequence encoding the C-terminal domain of *CshydY* (CTD, codons corresponding to residues 465-682), was cloned into the cloning site of p*HydY* using MEGAWHOP mutagenesis. The resulting plasmid (p*CTD*) was transformed in *E. coli* BL21(DE3) cells and grown aerobically (10 L/min air flow rate) at 37 °C in LBP supplemented with 30 μg/mL kanamycin and 0.002% anti-foam B (Sigma) until reaching an OD_{600} of 1.0 - 1.2. Cultures were induced with 0.5 mM IPTG and media was supplemented with 0.5 mM $(NH_4)_2Fe(SO_4)_2$, 0.5% (w/v) glucose and 0.5% (v/v) glycerol. The gas supply was switched to 2 L/min N_2 and temperature was adjusted to 20 °C during the additional 16-18 hours of protein expression.

The sequence encoding the N-terminal domain of *Cs hydY* (NTD, codons corresponding to residues 1-464) was cloned into two distinct plasmids. First, NTD was cloned in the same manner as CTD, generating p*NTD*. p*NTD* was transformed into *E. coli* BL21(DE3) cells, allowing for production of NTD without an H-cluster (NTD^{IM}). Additionally, NTD (with 5' His_6-tag from pNTD) was cloned into the first cloning site of p*Ca*I-*hydE* using NcoI and BamHI restriction sites. p*NTD-hydE* was transformed into *E. coli* Rosetta2(DE3)pLysS cells harboring *phydF-hydG* (p*Ca*I-*hydE* and p*hydF-hydG* were gifts from Dr. Paul King)[102] allowing for production and insertion of H-cluster.

Cells were grown aerobically (>10 L/min air) at 37 °C in LBP (LB plus 50 mM Na_2HPO_4, 50 mM KH_2PO_4, 25 mM $(NH_4)_2SO_4$ and 2 mM $MgSO_4$)[183] with 0.002% anti-foam B. Cultures of pNTD were supplemented with 30 μg/mL kanamycin, while cultures of pNTD-hydE/hydF-hydG was supplemented with 100 μg/mL ampicillin, 50 μg/mL spectinomycin and 30 μg/mL chloramphenicol. When the OD_{600} reached 0.6, the

cultures were supplemented with 1 mM L-cys and 1 mM ferric ammonium citrate. At OD_{600} of 1.2-1.5, 25 mM sodium fumurate, 0.5% (w/v) glucose and 0.5% (v/v) glycerol were added, the temperature was reduced to 20 °C, and the supply gas switched to 5 L/min N_2. After a 20 min purge with N_2, the cells were induced with 1.5 mM IPTG and grown for an additional 16-18 hours under 2 L/ min N_2.

Following protein expression, cultures were transferred to a glovebox by a peristaltic pump and centrifuged in anaerobic centrifuge bottles. Cell pellets were frozen in N_2 (*l*) and stored at -80°C until further use.

Protein purification

Cell pellets of *E. coli* Lemo21(DE3) with p*hydY* were resuspended and lysed in Buffer A (50 mM MOPS, 250 mM NaCl, 10 mM imidiazole, 5% glycerol, pH 7.0) with 0.5 mM $(NH_4)_2Fe(SO_4)_2$, 0.5 mM L-Cys, 1 mM DTT and 2 mM sodium dithionite (NaDT, ε_{315}=8 mM^{-1} cm^{-1}),[184] by sonication (Branson sonifier 450). The soluble fraction was isolated by centrifugation and loaded onto a 5 mL Ni-NTA column (GE LifeSciences). Column-bound protein as eluted with Buffer B (A plus 0.5 M imidiazole). HydY were incubated with 2 mM DTT and 1 mM $(NH_4)_2Fe(SO_4)_2$, concentrated by Amicon and loaded onto an analytical S200 gel filtration column equilibrated in Buffer SE (50 mM Mops, 250 mM NaCl, 5% glycerol, temperature adjusted pH=7.0). The dimeric fractions of HydY were combined and incubated with 1 mM $(NH_4)_2Fe(SO_4)_2$ for 2 hours. Excess iron was removed by 5 mL Hi-trap desalting columns (GE LifeSciences). Typical yields were <1 mg HydY/15L culture.

The CTD was purified from cell pellets of *E. coli* BL21(DE3) in a similar manner as HydY, except NaDT was omitted and a preparative-scale S300 gel filtration column (GE Life Sciences) was used. Dimeric fractions of CTD were incubated with 1 mM $(NH_4)_2Fe(SO_4)_2$ overnight and typical yields were 20-30 mg CTD/L of culture.

NTD^{IM} cell pellets were resuspended in buffer A supplemented with 20 mg lysozyme, 30 mg protease inhibitor A (Sigma), 1 mM $(NH_4)_2Fe(SO_4)_2$, 1 mM L-Cys, 2 mM DTT and 10 mM NaDT and lysed by sonication. NTD^{IM} was purified by Ni-NTA using a linear gradient buffer B. NTD^{IM} was concentrated in the presence of 1 mM DTT and was loaded onto an analytical S200 gel filtration column equilibrated in Buffer SE. Dark-brown monomeric fractions were collected with typical yields of 2-3 mg/L of *E. coli* culture.

Cell pellets with over-expressed NTD, HydE, HydF and HydG were thawed, resuspended in Buffer A2 (50 mM Tris-base, 250 mM NaCl, 5% glycerol, pH=8.0) supplemented with 20 mg lysozyme, 30 mg protease inhibitor A (Sigma), 1 mM $(NH_4)_2Fe(SO_4)_2$, 1 mM L-Cys, 2 mM DTT and 10 mM NaDT and lysed by sonication. The soluble protein fraction was loaded onto a 5 mL Strep-Tactin column (GE LifeSciences). NTD fractions were eluted using a linear gradient of Buffer B2 (Buffer A2 plus 5 mM desthiobiotin). NTD was concentrated in the presence of 1 mM DTT and 10 mM NaDT. The concentrated protein was loaded onto analytical S200 gel filtration column equilibrated in Buffer SE. Dark-brown monomeric fractions were collected with typical yields of 1-2 mg/L of *E. coli* culture.

T. maritima NADH/rubredoxin oxidoreductase (*Tm*NROR)[185] and *D. vulgaris* rubredoxin (*Dv*Rd),[186] as well as *E. coli* ferredoxin (*Ec*Fdx)[187] were purified as described previously.

Protein purity was >95% as judged by SDS-PAGE. Protein concentrations were estimated by Bradford, using BSA as a standard, unless otherwise stated. Protein iron and sulfur content was determined using assays developed by Fish[188] or Heibert, respectively.[189]

EPR spectroscopy

An as-isolated NTD sample (final concentration 120 μM) was oxidized with 20-fold molar excess of thionine and subsequently frozen in $N_2(l)$. A similar NTD EPR sample (final concentration of 90 μM) was prepared by addition of 1 mM NaDT. X-band continuous wave EPR spectra were recorded using a Bruker ELEXSYS II E 500 spectrometer equipped with a liquid helium cryostat.

Mössbauer spectroscopy

Isotopically labeled ^{57}Fe-CTD was prepared for Mössbauer experiments by using $^{57}FeCl_3$ throughout the expression and purification protocols. ^{57}Fe-CTD was concentrated to 750 μM and 600 μL was frozen in Mössbauer cups at -80°C. Reduced CTD was prepared by addition of 2 equiv of NaDT in the presence of 50 μM methyl viologen (as an electron mediator). Oxidized CTD was prepared by addition of 4 equiv of H_2O_2. EPR spectra were also collected on the oxidized and reduced CTD samples. Low-field Mössbauer spectra were recorded using a model MS4 WRC spectrometer (SEE Co., Edina, MN) at 5 K and 0.05 T (field applied parallel to the γ radiation), and

analyzed using WMOSS software (SEE Co.). Parameters are quoted relative to those of α-Fe foil at 298 K.

H_2 oxidation/H_2 production assays

H_2 oxidation activities were assayed in 1 mL septum-capped (SubaSeal, Sigma) quartz cuvettes in H_2-saturated (~0.78 mM H_2) Buffer C (50 mM Mops, 150 mM NaCl, pH 7.0). Reduction of methyl viologen (MV; one mol of H_2 reduces 2 mol of MV^{2+}) was monitored by the increase in absorbance at 604 nm (ε_{604} = 13.6 mM^{-1} cm^{-1})[102] using an Agilent 8453 spectrophotometer. Alternatively, activity was assayed via reduction of 0.15 mM methylene blue (MB; ε_{590} = 10.7 mM^{-1} cm^{-1} in buffer C).[74] Assays were initiated by addition of purified enzymes via gas-tight syringe.

H_2 production assays were performed in 20 mL septum-capped glass vials in 2 mL of Buffer C with 10 mM MV^{2+} and 25 mM NaDT. NTD solutions were placed in double-septa sealed glass vials and removed from the anaerobic glovebox. Assays were initiated via addition of an aliquot of NTD by gas-tight syringe. At 5.5 min intervals, 100 μL headspace samples were removed and injected into a GC-TCD (Thermo) equipped with carbosieve S-II 100/120 column (Sigma) using Ar as carrier gas. Headspace H_2 was quantified by comparison to H_2 standard curve. All measurements were conducted at room temperature.

Oxygen inactivation assay

Oxygen inactivation was assayed as described previously.[74] Briefly, the NTD (8.8 μM) in 2 mL buffer C was placed in a septum-sealed 20 mL glass vial. The vial was brought of the glovebox and at time zero the septum was removed, exposing the protein

solution to air. At intervals of 0, 1, 2.5, 5 and 10 min, samples were removed and residual activity was measured using methylene blue H_2 uptake assays.

H_2O_2/O_2 reduction steady-state measurements

Reduction of H_2O_2 and O_2 were determined by using an adaptation of a NADH reduction assay[156] with *Tm*NROR and *Dv*Rd as electron mediators. Oxidation of NADH was monitored by the decrease in absorbance at 340 nm (ε = 6.22 mM^{-1} cm^{-1}) upon addition of CTD in Buffer C. Initial NADH peroxidase rates were measured in an anaerobic (10-14 °C) glovebox with an Ocean Optics USB 2000+ spectrophotometer. Optimized conditions were determined by varying concentrations of *Tm*NROR and *Dv*Rd[190] using H_2O_2 as substrate. Final assay conditions were 0.2 mM NADH, 0.1 mM EDTA, 5-750 μM H_2O_2 (ε_{240} = 43.6 M^{-1} cm^{-1}),[191] 5 μM *Tm*NROR, 50 μM *Dv*Rd and 0.1 or 0.05 μM CTD listed in the order of injection. O_2 reduction assays were measured in 1 mL rubber septum-capped (SubaSeal, Sigma) quartz cuvettes using air-saturated Buffer C at 12°C (~280 μM O_2) with an Agilent 8453 spectrophotometer. Assay conditions were the same as H_2O_2 reduction assays with the following exceptions: 5-280 μM O_2 and initiated by injecting CTD (final concentration 0.1 μM) using gas-tight syringe. Background H_2O_2 and O_2-dependent NADH consumptions were subtracted from assays with CTD.

Reconstitution of hydrogenases with synthetic H-cluster

$[(Et_4N)_2\text{-}\{Fe_2[(SCH_2)_2NH](CO)_4(CN)_2]$ (**1**) was synthesized under a nitrogen atmosphere on a Schlenk vacuum as described previously.[192-195] Hydrogenase constructs were reconstituted by incubating 50 μL of immature protein solution under strictly

anaerobic conditions in 300 µl of 0.1 M potassium phosphate buffer (pH 6.7) with 2 mM sodium dithionite (NaDT) and a thousand fold molar excess of **1** at 25 °C. Unbound inorganic precursor was removed and reconstituted holo-protein simultaneously isolated by size-exclusion chromatography using a NAP-5 column (GE Healthcare).

Electrochemistry

Electrochemical experiments were performed in an anaerobic glovebox under a nitrogen atmosphere (Vacuum Atmospheres) using an autolab electrochemical analyzer employing GPES software. A single compartment, temperature-controlled electrochemical cell was used with platinum wire as the counter electrode, a Ag/AgCl reference electrode, and a rotating pyrolytic graphite edge (PGE) electrode (area 36π or 1π cm^2). Reported potentials are corrected to the standard hydrogen electrode (SHE) using $E_{SHE} = E_{Ag/Ag^+} + 0.197$.[88] The electrode was polished with 1.0 µm Buehler deagglomerated alpha alumina, sonicated, rinsed with water and dried in preparation for protein adsorption. To immobilize enzyme on the electrode surface, 1.0 µL of enzyme solution (0.5-5.5 µM) was spotted directly onto the electrode surface and allowed to incubate for five minutes before commencement of electrochemical experiments. The working electrode was rotating at a rate of 2750 rpm in all experiments. To account for irreversible loss of immobilized enzyme activity from denaturation or dissociation from the electrode surface, currents are, in some cases, normalized to the current of the same film measured at pH 7.0. In short, activity was evaluated at pH 7.0 both before and after the desired experiment, and data are normalized such that the average activity at 0 V at pH 7 is 1.

H_2-dependent reduction of CTD

Assays were prepared in 1 mL septum-capped (SubaSeal, Sigma) quartz cuvettes in H_2-saturated buffer C. Purified CTD or *E. coli* Fdx (25 μM) were added via gas-tight syringe and spectra were acquired for 5 minutes to establish baseline absorbance (Agilent 8453). NTD^e (88 nM) was then added via gas-tight syringe and spectra were acquired for an additional 5 minutes.

Sequence alignments

Homologous sequences were identified by BLAST genome search using *Cs*HydY as bait, with the requirement of at least one rubredoxin-like domain fused to an [FeFe]-H_2ase-like domain. Identified sequences, as of August 2014, were aligned with ClustalW[196,197] using gap open and extension penalties of 10 and 0.2, respectively. Mesquite[198] was used to generate a MrBayes[199,200] Nexus file, and MrBayes was used to calculate a phylogenetic tree using default values. Calculations were run until the split frequency standard deviation was <0.001. FigTree[201] was used to visualize and manipulate the resulting rooted phylogenetic tree.

Experimental section for Chapter IV

Protein preparation

The QuikChange method (Agilent) was used to introduce point mutants (S97A and T221M) into p*NTD-CahydE*, and the mutagenesis was confirmed by DNA sequencing. Plasmids containing the NTD variants were individually transformed in *E. coli* Rosetta2 BL21(DE3) pLysS competent cells harboring p*CahydF-hydG*. Proteins were expressed and purified as described previously (see Chapter II – Experimental Methods for Chapter III).

Solution activity measurements

H_2 oxidation and H_2 production measurements were conducted as described previously (see Chapter II – Experimental Methods for Chapter III).

FTIR

FTIR spectra were collected with a Nicolet 6700 FTIR Spectrometer (Thermo Fisher Scientific) equipped with a liquid nitrogen cooled HgCdTe (MCT) detector, a KBr beam splitter and OMNIC software. The light path, MCT detector and sample chamber were purged with dry nitrogen during the measurements. The IR spectra were collected with a total of 1024 scans of both the sample and the buffer reference at 2 cm^{-1} resolution. The anaerobic sample cell consisted of CaF_2 windows with an approximately 50 μM Teflon spacer (Pike Technologies), with a sample volume of approximately 50 μL. All spectra were recorded at room temperature. Absorbance baselines were adjusted using a manual baseline spline within the OMNIC software package.

Protein-film electrochemistry

Electrochemical experiments were conducted as previously described (see Chapter II – Experimental Methods for Chapter III) using a rotating pyrolytic graphite edge (PGE) electrode with an area of 36π. The electrochemical measurement for K_m as described previously,[202] with slight modifications. 1 atm 100% H_2 gas was switched to 1 atm N_2 at indicated time points. The electrode potential was poised at 0 mV vs SHE to maximize the H_2 oxidation current while minimizing anaerobic inactivation. All studies were conducting in 0.1 M K_2PO_4, 0.15 mM KCl and pH 7.0, unless otherwise stated. The electrode was rotated at 2750 rpm in order to minimize mass transport effects.

Computational modeling

DFT calculations were performed using a diffuse hybrid functional [M06/BS1, BS1=6-31+G(d)(Fe) and 6-31-G] implanted in Gaussian 09.[203] 1-fluorooctane (ε=3.89) was used to solvate models with M06/B21 and SMD solvent corrections. Geometry optimizations were conducted with the above basis set using atomic coordinates of *Clostridium pastueranium* [FeFe]-H_2ase I (3C8Y).[204] Methanethiol was used as a surrogate for $[4Fe\text{-}4S]_H$. A water molecule was modeled into the active site assuming approximately the same position as Ala230.

Experimental methods for Chapter V

Sequence alignments

Rbr homologs were aligned by MUSCLE[205,206] using default parameters and visualized using the JalView2 package.[207] Residues were colored with a 40% sequence

identity cut-off. Determination of secondary structure was predicted by JNET and compared to known structures.

Protein purification

CTD was purified as described previously in Chapter II. After thawing, a slight excess of H_2O_2 was added to CTD. Fully oxidized CTD (1 mL) was loaded onto an analytical S200 gel filtration column (GE LifeSciences) pre-equilibrated in 10 mM MOPS pH 6.8 at room temperature (pH 7 at 10°C). The tetrameric fraction was then pooled and concentrated in spin concentrators (30 kD MWCO, GE LifeSciences) to a final concentration of 21 mg/ml.

Crystallization and data collection

Initial sparse matrix screen were performed in 96-well sitting drop plates (Hampton) at 22°C. Thin plate crystals grew after six-months in 0.1 M Bis-Tris pH 6.5, 0.225 M NaCl and 18% PEG-3350. A round of additive screens (Hampton) using hanging-drap method at room temperature resulted in larger crystals. CTD (21 or 32 mg/mL) in 10 mM MOPS (pH 7), was mixed with optimized well solution [16-19% PEG-3350, 0.225 M NaCl, 0.1 M Bis-Tris (pH 6.5) and 1.5-4% xylitol] in a 1:1 ratio to make 4 µL hanging drops. Crystals large enough for data collection required two to three weeks for growth. Large, thin plate-like crystals grew in space group $P22_12_1$, but with slightly varying cells constants. Before being cryo-cooled, the crystals were cryoprotected in solution mother liquor and 20% PEG-400. After a 30s soak, the crystals were looped and flash-frozen in liquid N_2.

Data collection, processing, structure determination

Data was collected first at an in-house data-collection facility using a Cu-Kα rotating anode generator (Rigaku) and Rigaku R-AXIS IV^{++} detector. Higher resolution data was collected at SSRL beamline 7-1 equipped with a Visex microscope (Jan Scientific) and an ADSC Q315R CCD detector. Images were integrated and scaled with iMosfilm[208] and Aimless of the CCP4 suite[209] was used to process all the data sets.

Phases were determined by molecular replacement with Phaser[210] using 1LKO[180] as search model, and then those coordinates were used as molecular replacement for the SSRL 7-1 data set. Difference electron density and omit maps were manually fit using COOT[211] package and refined using PHENIX,[212] except 5% was used for R_{free} calculations. After several rounds of refinement, the active site was further built using a simulated annealing omit map of the active site to minimize model bias.

Experimental methods for Chapter VI

Sequence similarity network generation

All [FeFe]-H_2ase sequence were obtained from the National Center for Biotechnology Information (https://www.ncbi.nlm.nih.gov/). Input sequences were obtained by standard protein-protein BLAST searches (blastp) using *Clostridium symbiosum* HydY (*Cs*HydY, GI:769118840) from the non-redundant (nr) protein database. Redundant sequences (99%) were removed using CD-HIT,[213] totaling nearly 8000 sequences. No additional manipulation of the sequences was done; no manually truncated sequences were used. The manually curated sequence database, trimmed but not aligned, of [FeFe]-H_2ase sequences were used as nodes (with respective GI numbers)

and edges were generated using the all-by-all BLAST function (expect value E^{-150}) from a local install of the NCBI BLAST suite (v. 2.2.28+) in FASTA format. Initial networks were generated using the Blast2Sim[214] plug-in within Cytoscape (v. 2.8.3)[215] with a BLAST threshold of 0.01. Properties of interest (mainly domain architecture and functional annotation) were identified using Batch Conserved Domain (CD) search tool[216] from NCBI or a MOTIF search (http://www.genome.jp/tools/motif/) using the Pfam database were tabulated manually and overlaid onto the network using the Cytoscape VizMapper plug-in.[215]

Sequence alignments

Identified sub-group sequences were retrieved using Batch Entrez (http://www.ncbi.nlm.nih.gov/sites/batchentrez) and aligned by MUSCLE[205,206] (for <1000 sequences) within JalView2[207] or by Clustal Omega[217] (for >1000 sequences) using the EMBLE-EBI web service.[197] Sequence logos were generated using WebLogo 3[218] (http://weblogo.berkeley.edu/) using default values.

CHAPTER III

A CLASS OF ITS OWN: HydY, FROM CLOSTRIDIUM SYMBIOSUM, IS A H_2-DEPENDENT PEROXIDASE

Introduction

Hydrogenases (H_2ases) reversibly catalyze production or oxidation of hydrogen[3,7,219] and are classified according to their active site metals (NiFe or FeFe). [FeFe]-H_2ases exhibit the highest H_2 evolution rates,[220] and are a target for biological hydrogen production.[83] The active site of the [FeFe]-H_2ase, termed the H-cluster, consists of a standard cubane [4Fe-4S] cluster ($[4Fe\text{-}4S]_H$) and a diiron subcluster ($2Fe_H$) bridged by a cysteine. The irons of $2Fe_H$ are coordinated by CO and CN^- ligands and a bridging azadithiolate.[7] Biosynthesis of the $2Fe_H$ requires three auxiliary maturases, HydE, HydF and HydG.[221,222] Remarkably, insertion of inactive, chemically synthesized $2Fe_H$ complexes *in vitro* generates fully-functional [FeFe]-H_2ases.[60,117] The protein environment clearly influences catalysis, yet studies to elucidate the roles of second-sphere ligands in tuning active site chemistry have only recently been initiated.[118,223,224]

All studies to date[7,34,94,225] have found that [FeFe]-H_2ases are catalytically biased toward H_2 production, pointing to their typical *in vivo* function. For example, the [FeFe]-H_2ases from *Chlamydomonas reinhardtii* (*Cr*) and *Desulfovibrio desulfuricans* (*Dd*) are capable of maintaining H_2-evolution in the presence of an atmosphere of H_2, contrasting with [NiFe]-H_2ases that exhibit strong H_2 product inhibition.[34,225] Recent studies of heteromultimeric, bifurcating H_2ases[15,22,226] have found this class also functions similarly, but couples NADH and ferredoxin oxidation to drive H_2 production.

Additionally, multi-domain [FeFe]-H_2ases have been identified via bioinformatics,[5,14] including fusion proteins with apparent N-terminal H_2ases and C-terminal rubrerythrin domains, but have not been investigated for catalytic activity.

Rubrerythrins (Rbrs) contain rubredoxin-type ($Fe(Cys)_4$) and non-heme, His/Glu ligated diiron sites. *In vivo*, these enzymes appear to function in the reactive oxygen species (ROS) response system in air-sensitive microbes[128] as primary scavengers under anaerobic conditions.[121] Their diiron sites are ligated by pairs of $D/Ex_{29-37}Ex_2H$ motifs, similar to the diiron sites in methane monooxygenase (MMOH) and ribonucleotide reductase (RNR); however, oxygen activation has not been reported for Rbrs.[128] Instead, Rbrs rapidly reduce H_2O_2 ($k_{cat} > 2000$ min^{-1})[156] to water using C-terminal or N-terminal rubredoxin (Rd) sites as electron transfer agents. Additionally, Rbrs that contain N-terminal Rds exhibit a much faster O_2 reduction (O_2R) rate.[152] The mechanism for increased O_2R remains uncertain, and to-date, no di-rubredoxin Rbr has been studied.

Herein, we report on the first investigation of an [FeFe]-H_2ase-Rbr fusion protein, named HydY, from the obligate anaerobe *Clostridium symbiosum*. Our study indicates the N-terminal domain (NTD) of HydY contains [4Fe-4S] and H-cluster sites and the C-terminal domain (CTD) is a Rbr flanked by two Rd sites (Figure III-1). We show that the CTD reduces H_2O_2 at rates similar to typical Rbrs, whereas the NTD exhibits atypical [FeFe]-H_2ases catalysis: H^+ reduction inhibition by H_2 and a catalytic bias toward H_2 oxidation. These catalytic properties contrast starkly with well-characterized [FeFe]-H_2ases and suggest specific protein-tuning features for HydY.

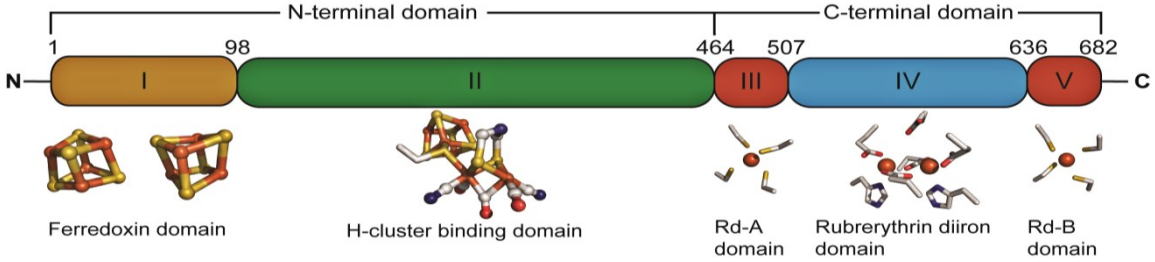

Figure III-1. Cartoon of the domain architecture and metal cofactors identified for *C. symbiosum* HydY. Domains are indicated with colored boxes, with the respective domain numbers inside. Numbering outside boxes indicates amino acid residues of various domains. Residues 1-464 share high sequence identity to group A [FeFe]-H_2ases, and will be referred to as N-terminal domain (NTD). The NTD contains domain I, the ferredoxin domain (a pair of [4Fe-4S] clusters, F-clusters), and domain II, the H-cluster ([4Fe-4S]-$2Fe_H$) domain. Residues 465-682 have sequence identity to Rbrs, and will be referred to as C-terminal domain (CTD). Domains III and V appear to encode rubredoxin (Rd) domains; domain IV appears to encode a diiron domain most similar to Rbrs. Here, Rbr will refer to just the diiron active site (and not the flanking mononuclear iron Rd sites) to simplify the nomenclature. Standard nomenclature refers to Rbr as a diiron site with a C-terminal Rd, whereas reverse-Rbr refers to a diiron site with a N-terminal Rd. No previously characterized Rbr contains both N- and C-terminal Rds.

Moreover, we provide evidence that HydY domain activities are coupled; indicating HydY has an unprecedented H_2-dependent peroxidase function.

Results

HydY from *C. symbiosum* (*Cs*HydY, WP_044902140.1) was codon optimized for *E. coli* and overexpressed without the $2Fe_H$ biosynthetic enzymes HydE, HydF and HydG. This immature form of the enzyme ($HydY^{IM}$) was anaerobically purified and appeared to form a dimeric species (Figure III-2). $HydY^{IM}$ bound 15 ± 1 Fe and 12.3 ± 0.2 S^{2-} per protein based on colorimetric analysis, where was close to the stoichiometry predicted by motif analysis (16 Fe and 12 S per protein; Figure III-1). The electronic

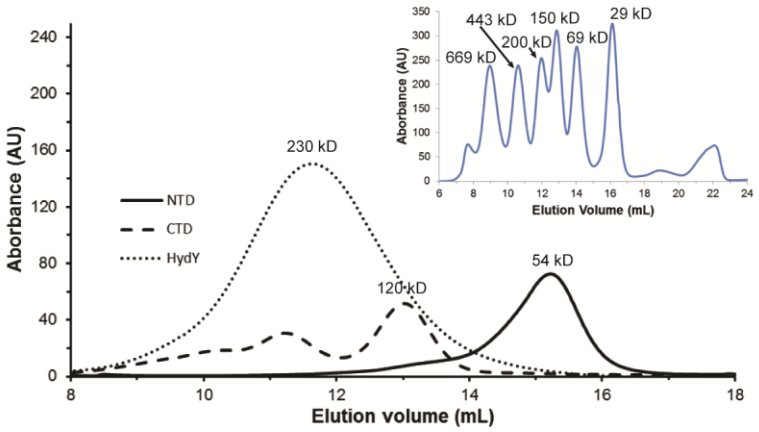

Figure III-2. Analytical gel filtration reveals quaternary structure of HydY constructs. NTD (1 mg/mL, solid line) elutes at its calculated molecular weight (54 kD). CTD (1 mg/mL, dashed line) elutes as a tetramer (120 kD; monomer MW = 28 kD). HydY^{IM} (5 mg/mL, dotted line) elutes at molecular weight of 230 kD (monomer molecular weight 80 kD), indicating a trimer. Based on oligomers formed from the synthetic constructs, HydY likely is an elongated dimeric species, causing it to elute at slightly larger molecular weight. All runs are the average of at least two experiments. Inset indicates standards run to estimate molecular weight of HydY constructs.

absorbance spectrum of HydY^{IM} (data not shown) revealed broad features from 300 to 500 nm, consistent with charge transfer bands for [4Fe-4S] clusters.

To evaluate the catalytic activity of HydY^{IM}, we immobilized it on a pyrolytic graphite edge electrode. When an enzyme is adsorbed to an electrode, the current response is proportional to turnover frequency. Figure III-3 shows a cyclic voltammogram from a HydY^{IM}-coated electrode in the presence of 0.15 mM H_2O_2. At reducing potentials below approximately +0.1 V (all potentials are reported relative to SHE), a catalytic current is observed, indicating reduction of H_2O_2 by HydY^{IM}. The response on a freshly polished electrode under the same experimental conditions does

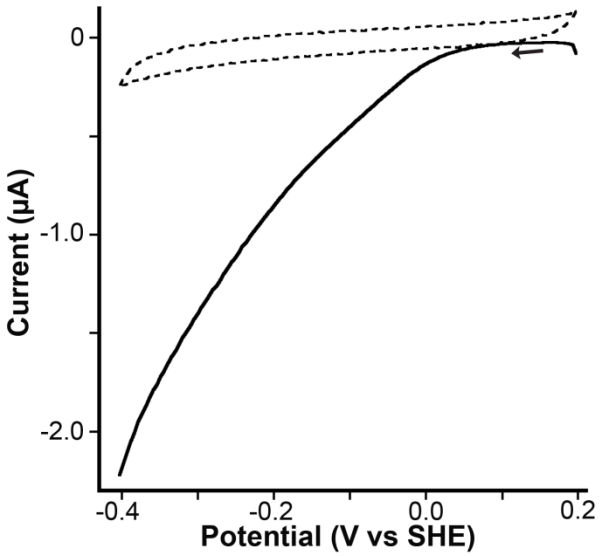

Figure III-3. Potential dependence of electrocatalytic reduction of H_2O_2 by $HydY^{IM}$. The black trace shows the current of the cyclic voltammogram of $HydY^{IM}$ in the presence of 0.15 mM H_2O_2. The dotted line is the response of a freshly polished electrode without a protein film. Cyclic voltammograms are obtained at a potential scan rate of 20 mV s^{-1} and electrode rotation rate of 2750 rpm in mixed buffer at pH 7. The arrow indicates the starting point and direction of potential cycling.

not show catalysis, demonstrating that enzyme is absolutely required for catalytic activity. Furthermore, the catalytic activity depends on [H_2O_2] at low concentrations (Figure III-4). Additionally, the potential at which a catalytic current was obtained (E_{onset} = +100 mV) designated the generation of a species capable of either peroxidase activity or electron transfer, and this potential was similar to midpoint potentials measured for Rbrs.[150] Together, these results support the ability of $HydY^{IM}$ to catalytically reduce H_2O_2 (peroxidase activity). We hypothesized that this peroxidase activity was initiated at the CTD, which contains apparent Rbr and Rd centers.

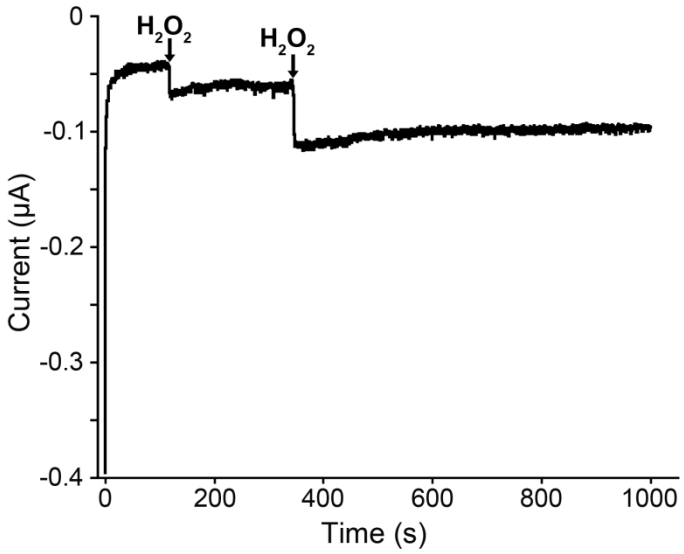

Figure III-4. HydY^{IM} shows time-dependent scavenging for H_2O_2. Chronoamperometry of Hyd^{IM} absorbed onto a rotating PGE electrode poised at -0.3 V in the presence of 0.2 mM H_2O_2. Multiple injections of 0.15 mM H_2O_2 (marked by arrows) electrocatalytic response to additional substrate. Other experimental conditions include: electrode rotation rate 2750 rpm and buffer pH of 7.0.

Spectroscopic and functional characterization of the CTD

Yields of HydY^{IM} were exceedingly low (< 1 mg/15 L of E. coli culture), preventing efforts to spectroscopically characterize this protein. *Cs*HydY is annotated to contain multiple [4Fe-4S] clusters as well as three other non-heme iron centers, thus efforts to characterize the iron centers would likely result in overlapping spectroscopic signals, limiting potential insights. In an effort to aid characterization of HydY and increase yields of protein, a synthetic construct of the C-terminal domain (CTD) of *Cs*HydY (residues 465-682, Figure III-1) was cloned. The CTD has high sequence identity to Rbrs with C-terminal Rds (*D. vulgaris* Rbr, 41%) as well as Rbrs with N-

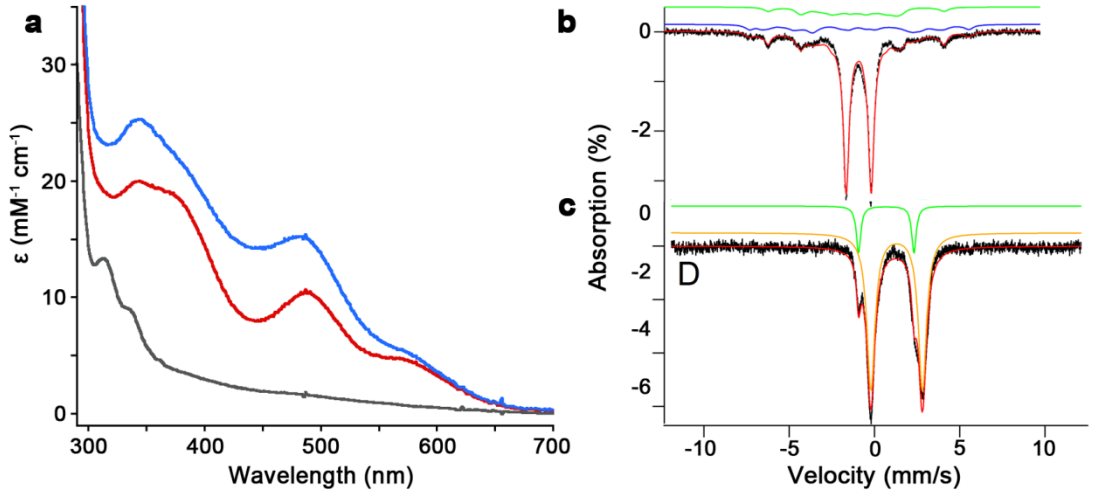

Figure III-5. Spectroscopic evidence that the CTD (HydY residues 465-682) contains Rbr and Rd iron sites. a) Electronic absorbance of CTD_{ox} (red), CTD_{ox} after addition of 1 M NaN_3 (blue), and CTD_{red} (grey). Mössbauer of 0.75 mM ^{57}Fe-CTD in oxidized (b) and reduced (c) states. The red lines are simulated spectra of the total components, while other colors represent simulations of individual components (see Supplemental Table 1). The oxidized samples were prepared by addition of 4 equivalents of H_2O_2. The reduced samples were prepared by addition of 2-fold excess of dithionite in the presence of 50 µM methyl viologen (as redox mediator).

terminal Rds (*C. acetobutylicum* reverse-Rbr, 32%). Thus, we hypothesized that the CTD could be expressed as an independent domain. In solution, the CTD appeared mostly tetrameric, with a propensity to oligomerize, especially if purified in air (Figure III-2). Incubation of the higher order oligomer of CTD with DTT, a reductant, resulted in reformation of the tetrameric state, consistent with reduction of disulfides. Quantification of protein-bound iron by colorimetric analysis revealed 4.1 ± 0.3 Fe/protein (expected 4 Fe/protein) from n = 3 preparations of this protein construct.

Spectroscopic properties of the CTD are reminiscent of both Rd and Rbr centers (Figure III-5). UV-vis spectra from oxidized CTD (CTD_{ox}) include characteristic features of Rbrs at 340, 492 and 575 nm, with a shoulder at 378 nm (Figure III-5a, red

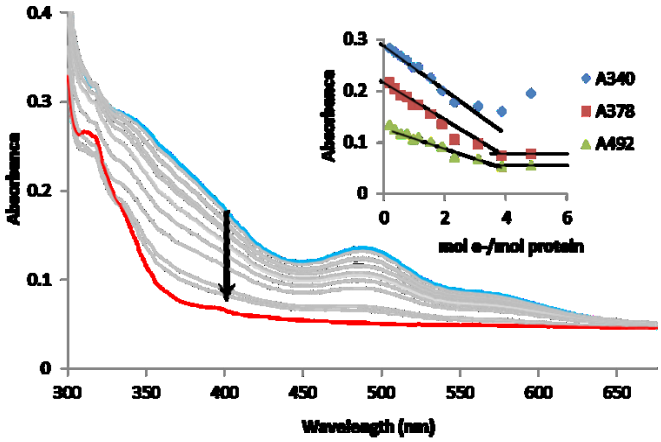

Figure III-6. Reductive titration of oxidized CTD by dithionite. Four reducing equivalents (2 mol dithionite) are required to completely bleach chromophores associated with oxidized CTD.

trace).[150,227] Sodium azide is often used as a probe for diiron site; coordination of azide to the diiron site results in an increase in the high-energy features. Addition of 1 M buffered sodium azide resulted in increased ε at 340 and 490 nm (Figure III-5, blue trace). The UV-vis spectrum of reduced CTD (CTD_{red}) is largely featureless in the visible region with a weak absorbance band at 320 nm, which is consistent with other reduced Rd sites (Figure III-5, gray trace).[156] A reductive titration revealed that four electrons were sufficient to fully reduce CTD_{ox} (Figure III-6).

Low temperature and low field Mössbauer spectrum of ^{57}Fe-enriched CTD_{ox} (Figure III-5b) consisted of a three species in a 2:1:1 ratio. The central doublet had parameters typical of similar to other oxygen-bridged diiron centers, such as Rbr, MMO and RNR (Table III-1).[150,228-230] The magnetic features were simulated at two S = 5/2 sites, with mostly equal intensity (Figure III-5b, blue and green traces). Simulated parameters of these sites fit with one tetrahedral ferric site with four cysteine sulfur

Table III-1. Mössbauer parameters of CTD in comparison with similar iron-binding proteins.

Protein	Oxidized			Reduced			ref
	δ (mm/s)	ΔE_Q (mm/s)	Area (%)	δ (mm/s)	ΔE_Q (mm/s)	Area (%)	
HydY-CTD	0.55	1.66	57	1.3	3.02	75	this work
	0.23	0.72	20	0.74	3.2	25	
	0.51	0.58	23	1.3	3.02		
Rbr	0.52	1.38	-	1.3	3.14	-	150,228
	0.53	1.74	-				
Rd	0.25	0.75	-	0.70	3.15	-	150
MMOH	0.5	1.07	-	1.30	3.14	-	229
RNR-R2	0.55	1.62	-	1.26	3.13	-	230
	0.45	2.44	-			-	

donors. The other site is best simulated with ferric iron coordinated primarily by 5 or 6 O/N donors (Table III-1). A low-temperature low-field Mossbauer spectrum of the fully reduced protein exhibited two quadrupole doublets of unequal intensities (Figure III-5c). The dominant double had parameters typical of diferrous clusters and the other double was best simulated to parameters of reduced Rd centers ((Table III-1). Unexpectedly, the diferrous cluster accounted for 75% of the Fe absorption and Rd site only 25%. This difference in Fe adsorption indicates that one Fe site, likely a Rd site, has mostly O/N

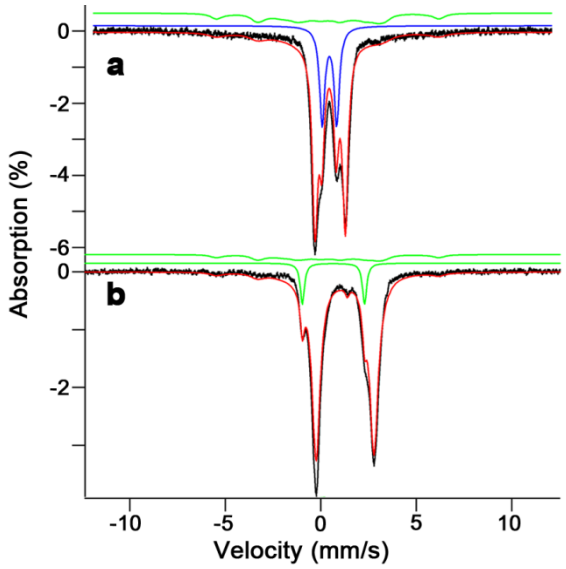

Figure III-7. Mössbauer spectra of ^{57}Fe-CTD. Spectra of 0.75 mM ^{57}Fe-CTD (a) oxidized state recorded at 150 K (b) and a partially oxidized sample recorded at 5 K and 0.05 mT field. The red lines are simulated spectra of the total components, while other colors represent simulations of individual components (see Table III-2).

ligation that has similar parameters to diferrous clusters. These observations suggest one of the putative Rd-like was destabilized in some manner during ^{57}Fe reconstitution, or one Rd-like site ligates iron in a non-classical fashion, *i.e.* ligation to metal with non-sulfur ligands.

To resolve incongruities in the metal centers, further Mössbauer studies were undertaken. First, a Mössbauer spectrum of ^{57}Fe-CTD$_{ox}$ at 150K was acquired to delineate the two magnetic features observed at low temperature (Figure III-7a). The dominant doublet had parameters consistent, but slightly shifted, from a typical oxo-bridged diferric cluster (Table III-2). The less intense doublet had parameters consistent

Table III-2. Mössbauer parameters of ^{57}CTD.

Site	δ (mm/s)	ΔE_Q (mm/s)	Γ (mm/s)	% (spectrum)	$A_{x,y,z}/g_n\beta_n$ (kG)	D (cm^{-1})	E/D	η
$[Fe^{III}\text{-O-}Fe^{III}]$	0.53; ox 100 K 0.51; ox 150 K	1.60; ox 100 K 1.58; ox 150 K	0.35; ox 100 K 0.35; ox 150 K	50; ox 100K 50; ox 150K 2%; semi	---	---	---	---
$[Fe^{II}\text{-O-}Fe^{II}]$	1.29; semi	3.03; semi	0.53; semi	52 of 77% semi	---	---	---	---
$Fe^{III}(Scys)_4$	0.23; ox 5K 0.23; ox 100K 0.23; ox 150 K	0.72; ox 5K 0.72; ox 100K 0.72; ox 150K	0.34; ox 5K 1.0; ox 100K 1.0; ox 150K	20; ox 100K 20; ox 150 K 13; semi	-60, -88, -148 ox 5K; ox 100 K; ox 150 K; semi	0.12	0.24	3.6
$Fe^{II}(Scys)_4$	0.68; semi	3.26; semi	0.26; semi	9; semi	---	---	---	---
$Fe^{III}(O/N)_4$	0.47; ox 100 K 0.45; ox 150K	0.76; ox 100K 0.75; ox 150 K	0.33; ox 100 K	25; ox 100K 25; ox 150 K	-300, -156, -183 ox 5 K	0.12	0.24	10
$Fe^{II}(O/N)_4$	1.29; semi	3.03; semi	0.53; semi	25 of 77% semi	---	---	---	---

with ferric iron coordinated by 5-6 O/N ligands. The ferric iron site for the Rd-centers appears hidden within the spectral baseline. We conclude that at 150 K, the O/N ligated iron species collapses in the fast-relaxation limit, while the Rd center is transitioning between fast and slow relaxation limits. Additionally, we prepared a partially oxidized sample by adding 1.5 equivalents of H_2O_2 to $^{57}CTD_{red}$. Incubation of substrate resulted in the color change from colorless (reduced CTD) to a light pink color (partially oxidized CTD). No attempts were made to purify excess reductant from $^{57}CTD_{red}$, and the partially oxidized sample was not purified after incubation with substrate. The

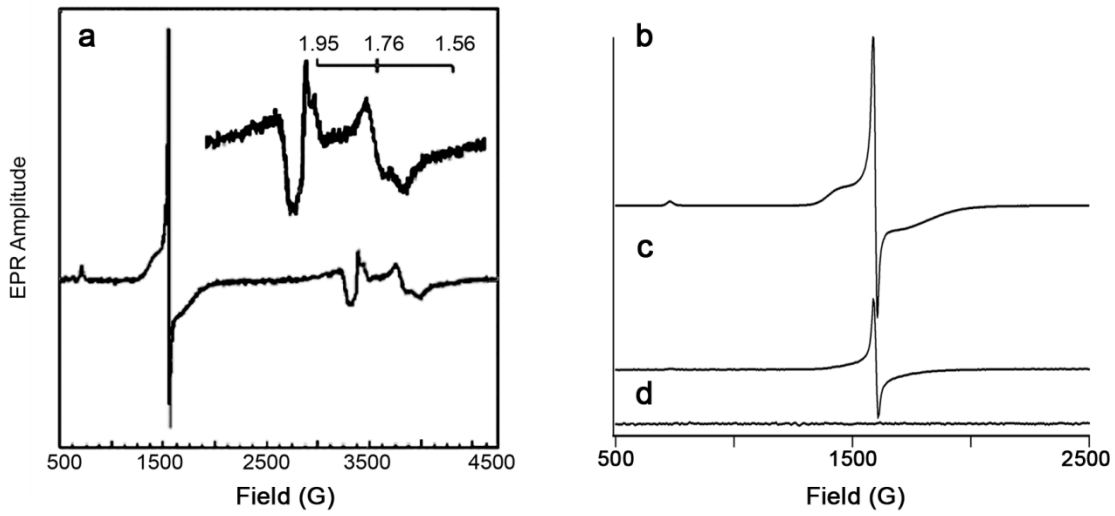

Figure III-8. CTD contains multiple iron binding sites. EPR spectrum of as-isolated CTD (a) or ^{57}CTD in oxidized (b), partially oxidized (c) and fully reduced (d) states. Parameters for EPR measurement were: sample temperature, 10K; microwave frequency, 9.43 GHz; microwave power, 0.519 mW.

resulting Mössbauer spectrum at low temperature and low field exhibited three partially overlapping quadrupole doublets and some magnetic (S = 5/2) species (Figure III-7b). The major doublet had parameter typical of diferrous iron clusters, implying that all the iron centers were re-reduced by the Rd-like sites upon substrate addition, especially evidenced by small (~4%) absorption typical of oxo-bridged diferric iron clusters (Table III-2). The other observed doublet arose from the classical diferrous Rd site. Magnetic features were also simulated, but due to the weak features observed, it is unclear of these sites represent the sulfur-ligated or O/N ligated mononuclear iron site.

To further characterize the iron sites of CTD, EPR spectra were collected. The as-isolated CTD yields a weak, rhombic S = ½ EPR signal with g-values of 1.95, 1.76 and ~1.56 (Figure III-7a). This $g_{ave} < 2$ signal arises from antiferromagnetically coupled

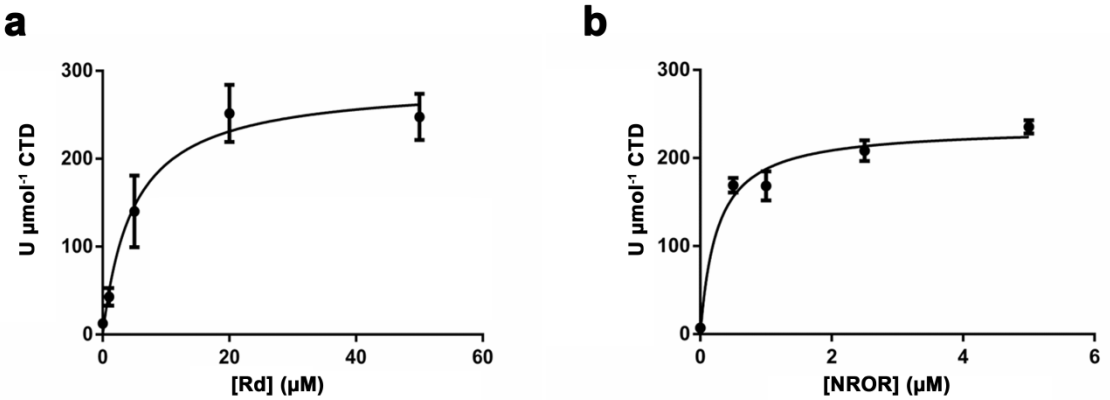

Figure III-9. Consumption of H_2O_2 by CTD is dependent upon Rd and NROR concentration. a) The rate of NADH oxidation dependent upon rubredoxin (Rd) concentration, saturating with 50 µM Rd. A Michaelis-Menten fit was applied to give the following parameters: k_{cat}, 380 ± 40 min^{-1}; K_m, 8 ± 2 µM; k_{cat}/K_m, 8 ± 2 x10^6 M^{-1} s^{-1}. b) The rate of NADH oxidation saturated with 5 µM NADH:Rd oxidoreductase (NROR). The data was fit with the Michaelis-Menten equation to give the following parameters: k_{cat}, 230 ± 10 min^{-1}; K_m, 0.25 ± 0.07 µM; k_{cat}/K_m, 1.5 ± 0.43 x10^7 M^{-1} s^{-1}. All assays were performed at 10-12°C, following loss of NADH signal (see Materials and Methods), with 0.1 mM H_2O_2 and 0.5 µM NROR (a) or 0.5 µM Rd (b). One unit is defined as 1 µmol H_2O_2 reduced per minute (1 µmol NADH reduced 1 µmol H_2O_2). Background consumption of NADH was subtracted from measured rates.

pair of high-spin Fe^{III} (S = 5/2) and Fe^{II} (S = 2) ions, and is a hallmark feature of diiron proteins with O/N ligation, such as Rbr. High-spin iron(III) accounts for g-values of 4.3 and 9.4, attributable to $Fe^{3+}(Cys)_4$ sites in Rds. However, the as-isolated CTD appears to contain two types of overlapping g = 4.3 signals, implying there may be two slightly distinct Rd sites, or Rd sites close enough to perturb individual signals. Indeed, EPR of $^{57}CTD_{red}$ contains only the 'sharp' g=4.3 signal (Figure III-8b), while the fully oxidized contains both g = 4.3 signals (Figure III-8a). The EPR and Mössbauer results support a model that includes four irons per CTD, including a diiron oxo site, a classical Fe^{III} rubredoxin site, and a mononuclear high-spin $Fe^{III}(O/N)_{5-6}$ site.

Taken together, high sequence identity, metal content and results from multiple spectroscopies provide clear evidence that the CTD contains two types of metal centers: a Rbr-like diiron site and two mononuclear iron sites, one similar to Rd-like and one with mostly O/N ligation. Further studies are required to resolve the identity of this third iron site.

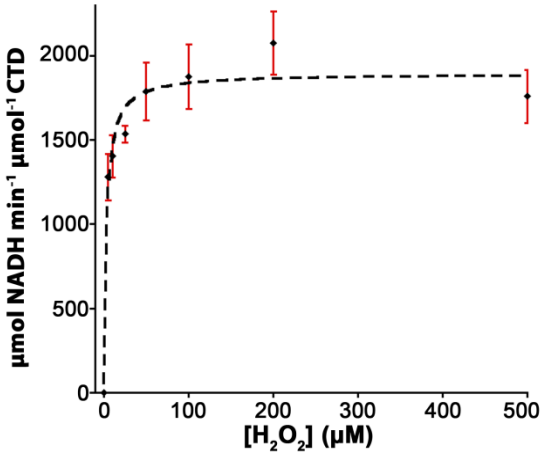

Figure III-10. The CTD is an efficient H_2O_2 reductase. Steady-state reduction of H_2O_2 was investigated using an in vitro system of 0.2 mM NADH, 5 µM NROR, 50 µM Rd, and 0.1 µM CTD The decrease of NADH absorbance (ε_{340} = 6.22 mM^{-1} cm^{-1}) was used to measure initial rate of H_2O_2 consumption after injection of the CTD. Data was fit to the Michaelis-Menten equation to yield the following kinetic parameters: k_{cat}, 1890 ± 70 min-1; K_m, 3.0 ± 0.8 µM; k_{cat}/K_m, 1.1 ± 0.3 x107 M^{-1} s^{-1}. All assays were performed at 10-12°C. Background consumption of NADH was subtracted from measured rates.

Functional characterization of CTD

Rbrs function as terminal components of NADH peroxidase or oxidase systems, reducing substrates to water dependent on Rd and Rd:NADH oxidoreductase (NROR).[156] The peroxidase rate, which was monitored via consumption of NADH at 340 nm, of CTD was heavily influenced by the concentrations of Rd and NROR, saturating at 50 and 5 μM, respectively (Figure III-9). Under these optimized conditions, peroxidase activity at 10 °C of CTD revealed the following parameters: k_{cat}, 1890 ± 70 min^{-1}, K_m for H_2O_2, 3.0 ± 0.8 μM and k_{cat}/K_m, 1.1 ± 0.3 x10^7 M^{-1} s^{-1} (Figure III-10). The measured k_{cat} was similar to the fastest reported Rbr peroxidase rates measured by others (>2000 min^{-1} at room temperature),[156] though CTD would likely be faster at the higher temperatures used in those experiments. Additionally, the K_m only represents an upper limit estimate due to the insensitivity of following NADH consumption by absorbance (5 μM NADH corresponds to an absorbance change of 0.03). Next, assays were performed under identical conditions except air-saturated buffer (~0.28 mM O_2) replaced H_2O_2. The NADH consumption rate for O_2 reduction was only 10 min^{-1}. This rate was only slightly above background NADH consumption without enzyme and was orders of magnitude slower than the measured peroxidase activity of CTD. Thus, the CTD prefers H_2O_2 as a substrate over O_2, similar to other Rbrs.[128]

Spectroscopic and functional characterization of the NTD

The NTD of *Cs*HydY (residues 1-464, Figure III-1), which has high sequence identity to monomeric [FeFe]-H_2ases (Dd, 44%; Cr, 38%), was also expressed as an independent construct. NTD was prepared in the absence (NTD^{IM}) or the presence (NTD^{e}) of hydrogenase maturases.[102] Proteins derived from both NTD-expressing constructs are monomeric (Figure III-2), and contain 10.5 Fe and 11 S^{2-} per protein. The electronic absorbance spectrum of NTD exhibited features consistent with Fe-S clusters (Figure III-11). Dithionite-reduced NTD^{IM} also has an S = ½ EPR signal with temperature and power saturation properties consistent with [4Fe-4S] clusters (Figure III-10). Taken together, the NTD appears to bind three [4Fe-4S] clusters.

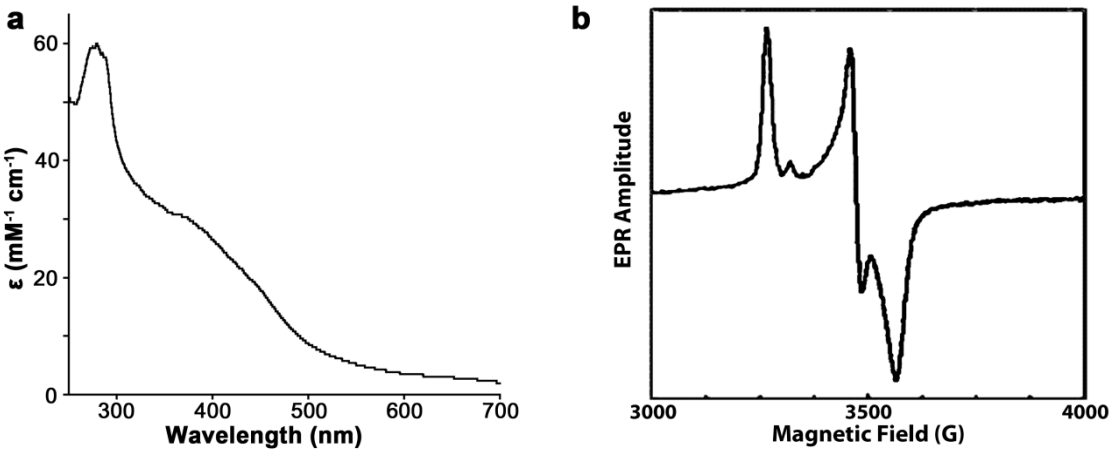

Figure III-11. Spectroscopic investigation of the NTD^{IM}. a) Electronic absorbance of as-isolated NTD^{IM} (25 μM) reveals broad absorbance features between 300 and 500 nm, typical of Fe-S centers. b) EPR spectrum of reduced NTD^{IM}. Parameters for EPR measurement were: sample temperature, 10K; microwave frequency, 9.43 GHz; microwave power, 0.519 mW. Sample was prepared by adding excess NaDT to as-isolated NTD^{apo} (150 μM).

Table III-3. H_2ase activity parameters for NTD[e] and various other [FeFe]-H_2ases.

	HydY	*Cp*II	*Cp*I	*Dd*	*Ca*	*Cr*
Molecular weight (kD)	54	54.7	62	45.8	64	53
Turnover number (min^{-1}), H_2 evolution	2.4 ± 0.2	9.1	5683	8000	1800	880
Turnover number (min^{-1}), H_2 oxidation[e]	4,000 ± 260[a,b]	34,000[c]	24,000[c]	38200[c]	NR	5
K_m, H_2 (μM)	60 ± 20	30	200-390	NR	460[d]	190,500[d]
Ratio (ox/red)	10,000	3,400	4.4	4.8	-	176
References	This work	74	74,231	40	223	232

[a]k_{cat}, determined by varying [H_2]
[b]Assays conducted at pH 7.0
[c]Assays conducted at pH 8.0
[d]K_m determined with PFE (ref 95)
[e]Determined using methylene blue

NTD[e] shows atypical [FeFe]-H_2ase catalytic behavior.[40] In a standard assay with methyl viologen (2 mM), the NTD exhibited H_2 uptake molecular activity of only 25 U/μmol NTD[e] (U = μmol dye consumed min^{-1}), orders of magnitude slower than rates measured for [FeFe]-H_2ases isolated from native source[231] or from recombinant systems.[223,232] The H_2 consumption rate depended on methyl viologen concentration, saturating at 0.2 M (data not shown). NTD[e] steady-state kinetics under these conditions exhibited a k_{cat} of 320 min^{-1} and K_m for H_2 of 20 μM (Table III-3). Interestingly, replacing methyl viologen for 0.15 mM methylene blue increased the H_2 consumption

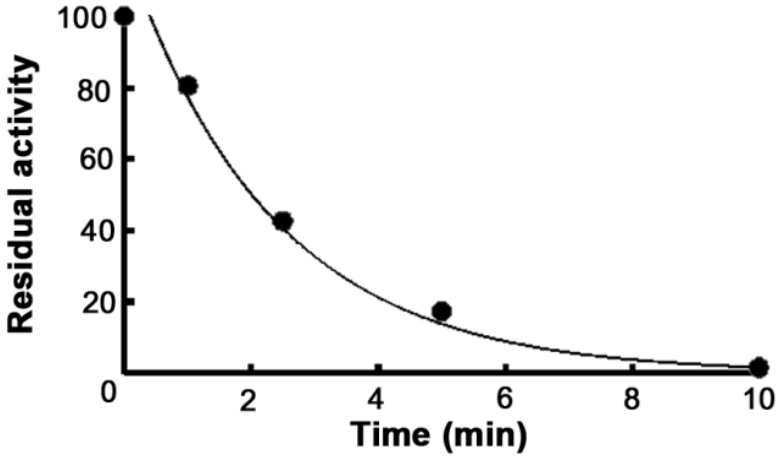

Figure III-12. Inactivation of NTD^{e} by O_2. NTD^{e} (2 mL) in buffer C in a septum-sealed dram vial (20 mL) was stirred by stir plate incubated at 22 °C. At zero time, the septum was removed to expose NTD^{e} to air. At the designated intervals, samples were analyzed for residual H2 uptake activity (see Materials and Methods). Data was fit to exponential model, yielding a fit y=119.7e-0.433x and a t1/2 of 1.44 minutes.

rate 12.5 fold (4,000 min^{-1}) and only marginally affected the K_m (60 μM). Additionally, NTD^{e} displayed marginal H_2 production, with a specific activity of 130 U/mg protein. Similar catalysis has been described for another [FeFe]-H_2ase, the H_2-uptake *C. pasteurianum* H_2ase II (*Cp*II, 58% identity to HydY).[74] The lowered H_2 production activity of NTD^{e} had no effect on O_2 inactivation rates (Figure III-12), similar to inactivation rates observed for numerous other [FeFe]-H_2ases.[74,233]

Electrochemical investigation of HydY^{s} and NTD$^{e/s}$

Figure III-13 shows that NTD^{e} electrocatalytically reduces protons and, in the presence of hydrogen, oxidizes hydrogen. In the absence of hydrogen, negative current attributable to proton reduction is observed at potentials below that of the H^+/H_2 couple (Figure III-13a, gray). Upon introduction of an atmosphere of H_2, several changes in the

voltammetric response are noticeable (Figure III-13a, black). First, proton reduction current is significantly decreased, suggesting that H_2 is a strong product inhibitor for proton reduction. Such activity is well known for [NiFe]-H_2ases but has not been previously reported for an [FeFe]-H_2ases.[96] Second, at oxidizing potentials, a large

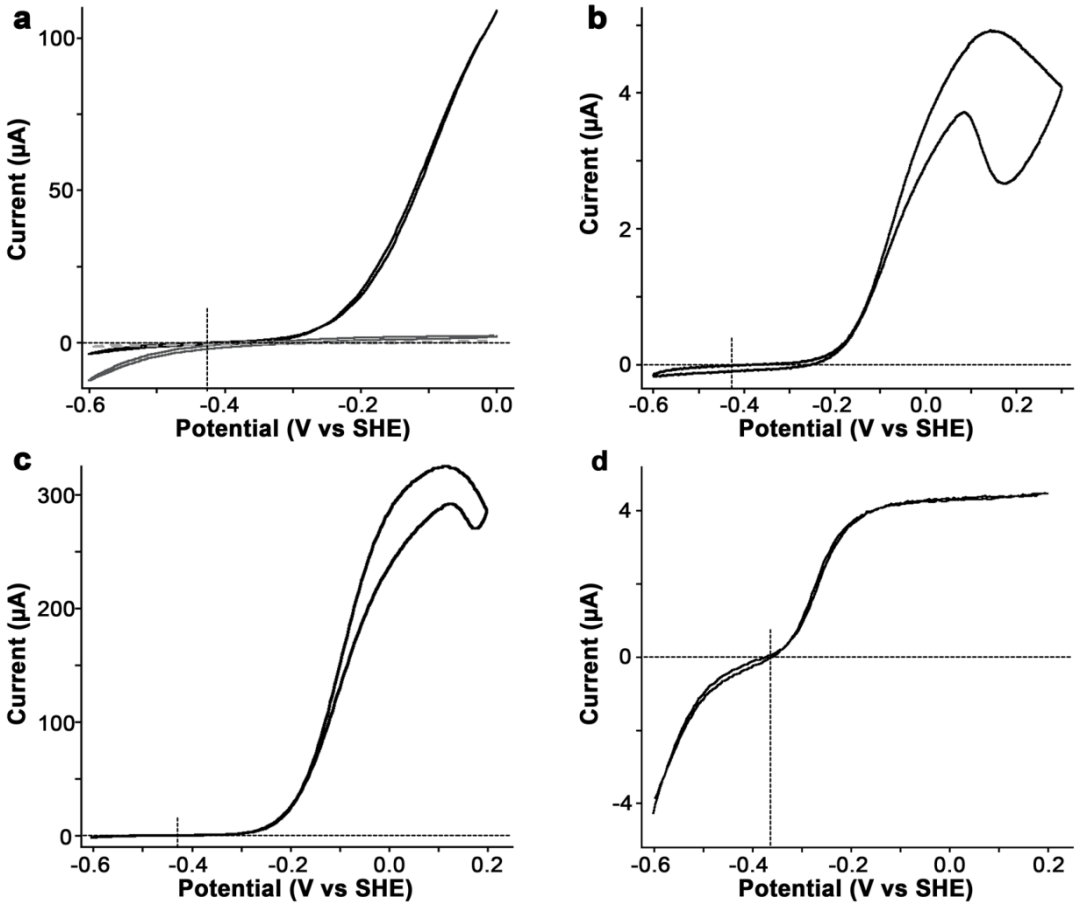

Figure III-13. *Cs*HydY is biased toward H_2 oxidation. a) NTD^e under continuous sparging of 1 atm 100% H_2 (black trace, 0.78 mM) and 1 atm N_2 (gray trace) with 5 mV s^{-1} scan rate. The light gray dotted scan is an electrode under the same conditions that has not been exposed to enzyme. b) NTD^s under 1 atm 100% H_2. $HydY^s$ under 1 atm of c) 100% H_2 or d) 1% H_2. Other experimental conditions include: electrode rotation rate 2750 rpm and buffer pH 7.0. The horizontal line indicates zero current and the vertical line indicates the H^+/H_2 couple at pH 7.0 and 1 atm 100% H_2 (-420 mV, a-c) or 1% H_2 (-350 mV, d).

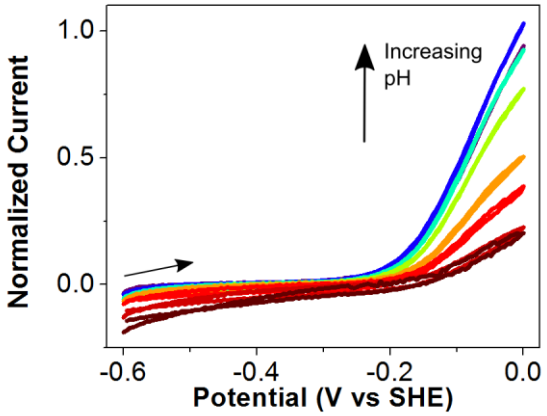

Figure III-14. Catalytic cyclic voltammograms for NTD^s adsorbed to a PGE electrode over a range of pH values. The pH values shown are 8.0, 7.5, 6.5, 6.0, 5.5, 5.0, 4.5, and 4.0. Other experimental conditions include: electrode rotation rate 2750 rpm and potential scan rate of 20 mV s^{-1}. Catalytic signals were normalized such that the average activity at 0 mV at pH 7 is 1. The concentration of dissolved hydrogen is held at 0.78 mM by continuously sparging with 1 atm of hydrogen gas. The black arrow signifies the starting potential and scan direction.

positive current arises from electrocatalytic oxidation of hydrogen. The hydrogen oxidation current is rotation rate dependent at low rotation rates, indicating that catalysis is limited by mass transfer of hydrogen to the electrode surface. Thus, all subsequent experiments were undertaken at a high electrode rotation rate (2750 rpm).

Additionally, oxidative catalysis is not observed until the experimental potential is approximately 100 mV more oxidizing than the H^+/H_2 couple. This excess potential is referred to as overpotential. Although a requirement for considerable overpotential for hydrogen oxidation has been reported for some oxygen-tolerant [NiFe]-H_2ases, overpotential has not been previously described as essential for catalysis by an [FeFe]-

H_2ase.[34] As suggested by solution assays of NTD^e, the voltammetric experiments demonstrate considerably higher rates for hydrogen oxidation than H_2 production. At the most extreme potentials assayed, H_2 is oxidized 5-25 times faster than it is produced under reducing conditions (depending on whether reduction is assayed in the presence or absence of hydrogen). Such an extreme electrocatalytic bias towards H_2 oxidation has not been reported previously for an [FeFe]-H_2ases. It is worth noting that electrocatalytic activity depends on pH (Figure III-14), and thus the magnitude of the bias is also pH dependent.

To ensure this atypical electrocatalytic profile was due only to HydY-specific tuning, NTD^{IM} and HydY^{IM} were reconstituted with $[(Et_4N)_2\{Fe_2[(SCH_2)_2NH](CO)_4(CN)_2]$ (**1**, see Methods)[117] to yield synthetically matured enzyme (NTD^s and HydY^s, respectively). By extending experiments to more extreme oxidizing potentials and slower potential scan rates, both constructs undergo anaerobic, oxidative inactivation at high potentials (Figure III-13b,c). The hydrogen oxidation current peaks at approximately +100 mV and then decreases at higher driving forces, i.e. more oxidizing potentials. This suggests that oxidation of the active site produces a catalytically incompetent state, as has been described previously other for [FeFe]-H_2ases.[34]

Figure III-15 shows E_{switch}, an apparent thermodynamic feature that defines this process in terms of the reactivation observed when potentials are returned to more reducing values. E_{switch}, the point at which -di/dE attains a local maximum, is not a reduction potential for the active site but instead represents a convolution of active site

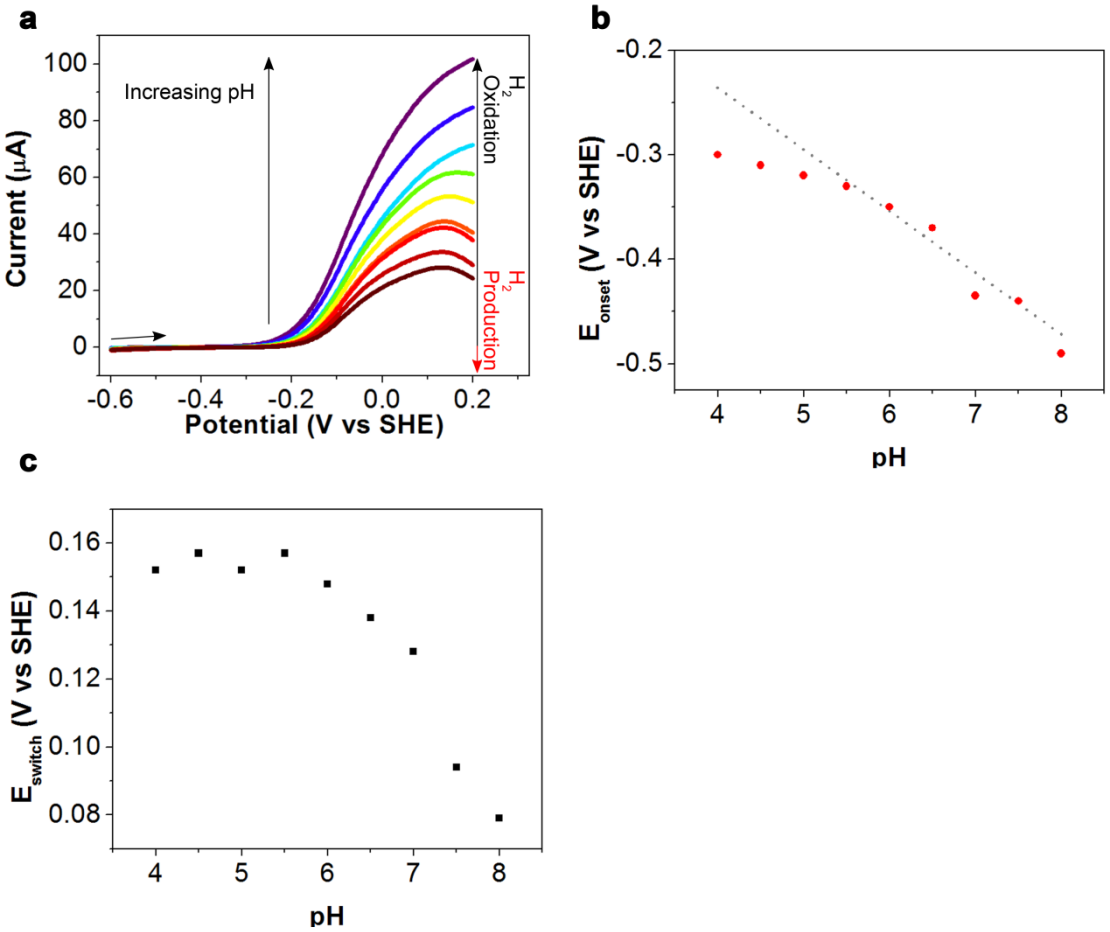

Figure III-15. Cyclic voltammograms of HydY^{s} adsorbed to a PGE electrode over a range of pH values. a) Reverse, reductive sweep of HydY^{s} electrochemical activity at pH values 8.0, 7.5, 6.5, 6.0, 5.5, 5.0, 4.5, and 4.0 (forward, oxidative scan omitted to better reveal onset potential). b) Potential of H_2 oxidation onset as a function of pH; the grey diagonal line indicates the expected equilibrium potential for the $2H^+/H_2$ couple pH dependence. The onset potential (E_{onset}) is defined as the zero-current intercept. c) pH dependence of anaerobic, oxidative inactivation for HydY^{s}. The switch potential (E_{switch}) was obtained from the inflection point of the reductive reactivation area, determined from the derivative (-d*i*/dE) of the reverse scan.

thermodynamics and kinetics of reductive reactivation. Oxidative inactivation/reductive reactivation of HydY/NTD is pH dependent with more inactivation observed as lower pH values. This is the opposite of the trend usually observed for hydrogenases and suggests the active site chemistry of HydY may be unique. Interestingly, the rate of

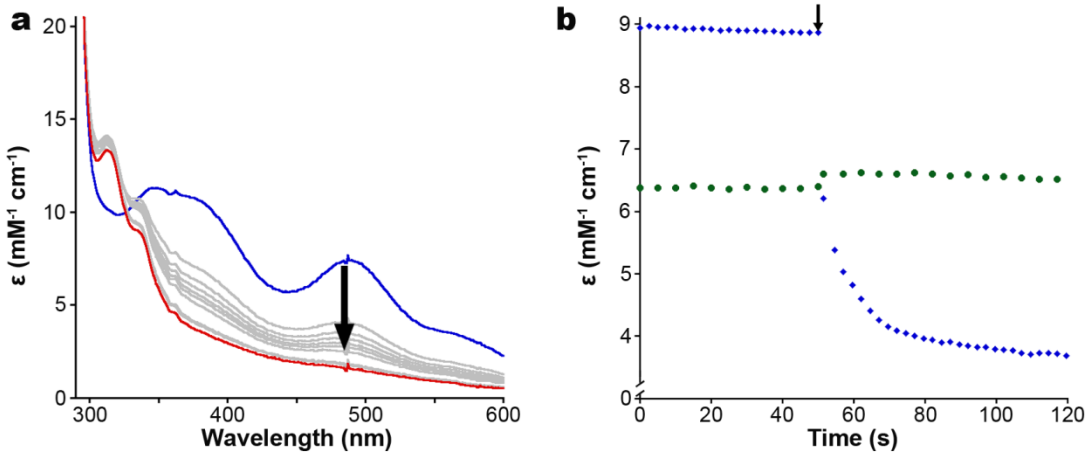

Figure III-16. H_2-dependent reduction of CTD by NTD^e. a) The CTD_{ox} (20 µM, blue trace) in H_2-saturated exhibits no changes in spectral features. Upon anaerobic addition of NTD^e (88 nM), spectral features of oxidized CTD dissipate, replaced with features consistent with reduced CTD. b) Kinetic analysis of a) monitored at 490 nm for CTD (blue diamonds) or 456 nm for *E. coli* Fdx (green circles).

anaerobic inactivation had a local minimum at pH 7.0, suggesting that the inactivation process was primarily a kinetic process. Furthermore, E_{onset} for H_2 oxidation does not follow a Nerstian decay (Figure III-14b).

In a 1% H_2 environment (Figure III-13d), HydY^s showed similar magnitudes of H^+ reduction and H_2 oxidation currents, indicating that the apparent H_2 inhibition constant (K_i^{H2}) for HydY must be below a 1% H_2 atm. The oxidative current is significantly decreased as well, suggesting that the K_m for H_2 is above 1% H_2. The concentration of dissolved H_2 under these conditions (~8 µM) agrees with the K_m measured by dye-coupled assays (20-60 µM) These results indicate HydY displays inhibition like [NiFe]-H_2ase, and K_m for H_2 higher that [NiFe]-H_2ase but lower than [FeFe]-H_2ase. Additionally, HydY^s requires minimal overpotential under 1% H_2 atm. This result suggests that the rate limiting step for catalysis is governed, at least, by active

site chemistry. However, a residual slope near the H^+/H_2 couple (-360 mV) suggests electron transfer also contributes to the rate-limiting step.[98,234]

H_2-dependent reduction of the CTD by NTD^e

We tested whether the activities of the N- and C-terminal domains of HydY can be coupled by combining the independently expressed and purified domains *in situ* (Figure III-16). Anaerobic incubation of CTD_{ox} (25 μM) in a H_2-saturated buffer (~0.78 mM) does not cause a change in the absorbance spectrum (blue trace). On the other hand, an additional anaerobic injection of NTD^e (88 nM) results in the loss of CTD_{ox} absorbance peaks and formation CTD_{red} features characteristic of reduced Rd centers (red trace). The change in absorbance at 490 nm indicates that injection of NTD^e resulted in near immediate reduction of CTD_{ox}, suggesting NTD^e directly reduces CTD (Figure III-15b). To evaluate whether NTD^e could reduce additional protein substrates, it was also incubated with *E. coli* Fdx, a [2Fe-2S] cluster-binding protein that functions in one-electron transfer processes. No spectral changes of Fdx were detected. This implies that reduction of CTD by NTD is: 1) dependent upon H_2 and not mediated by spurious dithionite from NTD purification; and 2) not a general process since Fdx was unable to be reduced by NTD^e. Overall, the rapid reduction of a >250-fold molar excess of CTD_{ox} is consistent with reducing equivalents originating from dissolved H_2.

Bioinformatic analysis of HydY homologs

We next used BLAST to identify HydY homologs. We filtered the BLAST hits by requiring that the hits be fusion protein with the conserved H-cluster motifs and at least one Rd domain. In all, 40 HydY homologs were identified (Figure III-17).

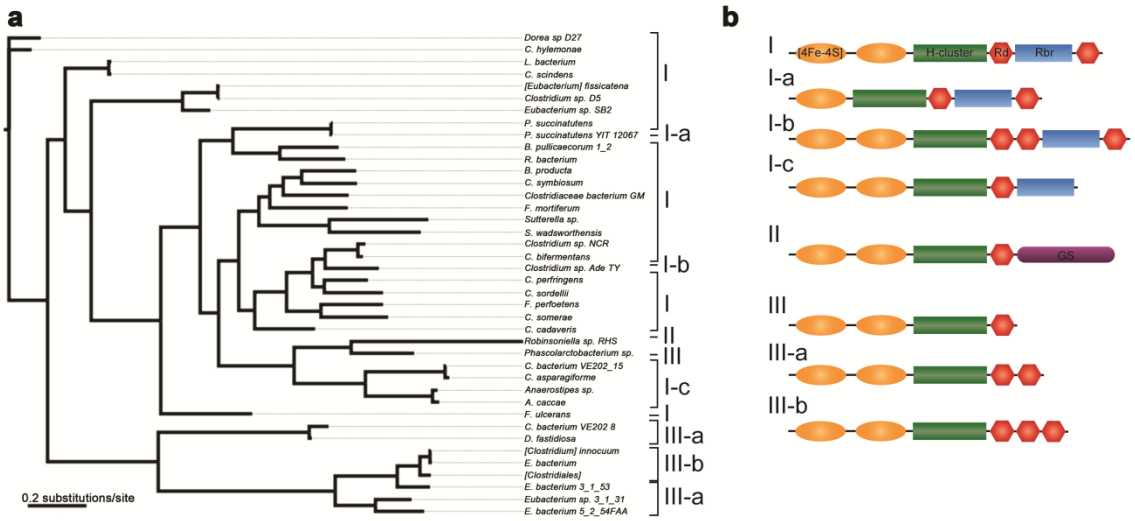

Figure III-17. Phylogenetic grouping of modular HydY homologs. a) Phylogenetic tree of CsHydY homologs identified by BLAST (December 2015) calculated using MrBayes (scale bar: 0.2 substitutions per site, 15000000 generations sampled every 1000 generations with an average standard deviation of split frequencies <0.0002) and visualized with FigTree. Homologs of HydY were identified in Firmicutes, Fusobacteria and Proteobacteria. b) HydY homologs are highly modular and separate into three classes. Class I contains [4Fe-4S] cluster, H-cluster, Rd and Rbr binding domains. Sub-classes of Class I (a-c) retain a C-terminal rubrerythrin domain, but vary in putative electron transfer domains. The class II HydY homolog has a C-terminal domain with high sequence identity to glutamate synthase domain. Class III homologs contain only varying numbers of Rd domains and lack putative C-terminal redox active sites.

Homologs of *Cs*HydY are scattered throughout *Firmicutes*, *Fusobacteria* and δ-*Proteobacteria*, with the *Clostridia* order (35 homologs) mostly represented. Distinct classes (I, II and III) of HydY homologs were identified. Class I is the most common, with motifs similar to that of *Cs*HydY (Figure III-I). Deviations from this architecture, such as missing the second Rd motif but retaining the Rbr domain, were classified as I-A, B or C (Figure III-17). Class II HydY sequences contained alternate C-terminal domain fusions other than Rbr, such as a glutamate synthase (GS) domain in HydY from *Robinsellia sp*. RH5. GSs synthesize glutamate from glutamine and α-ketoglutarate, requiring external electrons from either ferredoxin or NAD(P)H.[77] Lastly, Class III

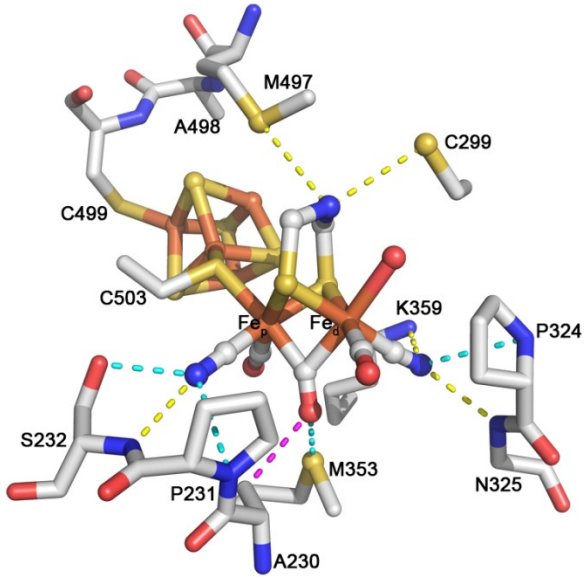

Figure III-18. Representation of the H-cluster in *C. pastuerinium* HydA1 (*Cp*I; PDB:3C8Y) with important protein interactions. Hydrogen bonds are shown in yellow. Protein residues within van der Wall's contact are depicted in cyan. Hydrophobic interactions (A230 to bridging CO) are shown in pink. Note, the bridgehead of the azadithiolate was modeled as oxygen, and was colored blue to represent currently accepted bridgehead nitrogen.

HydY sequences lacked additional redox active sites and variable numbers of Rd domains, thus the electron donor/acceptor is ambiguous.[5,14]

Sequence analysis of all identified HydY homologs and CpII revealed marked differences within second-shell motifs for binding H-cluster and [4Fe-4S] clusters. Three conserved motifs provide second-shell interactions for the H-cluster: P1, TSCCPxW; P2, $MPCx_2Kx_2E$; and P3, $ExMACx_2GCx_2GGGxP$ (Figure III-18). HydY homologs contain conserved substitutions within canonical H-cluster binding motifs and a third in a previously unidentified region (Figure III-19). All HydYs and *Cp*II have completely conserved P1 sequences. Within the P2 motif, a conserved

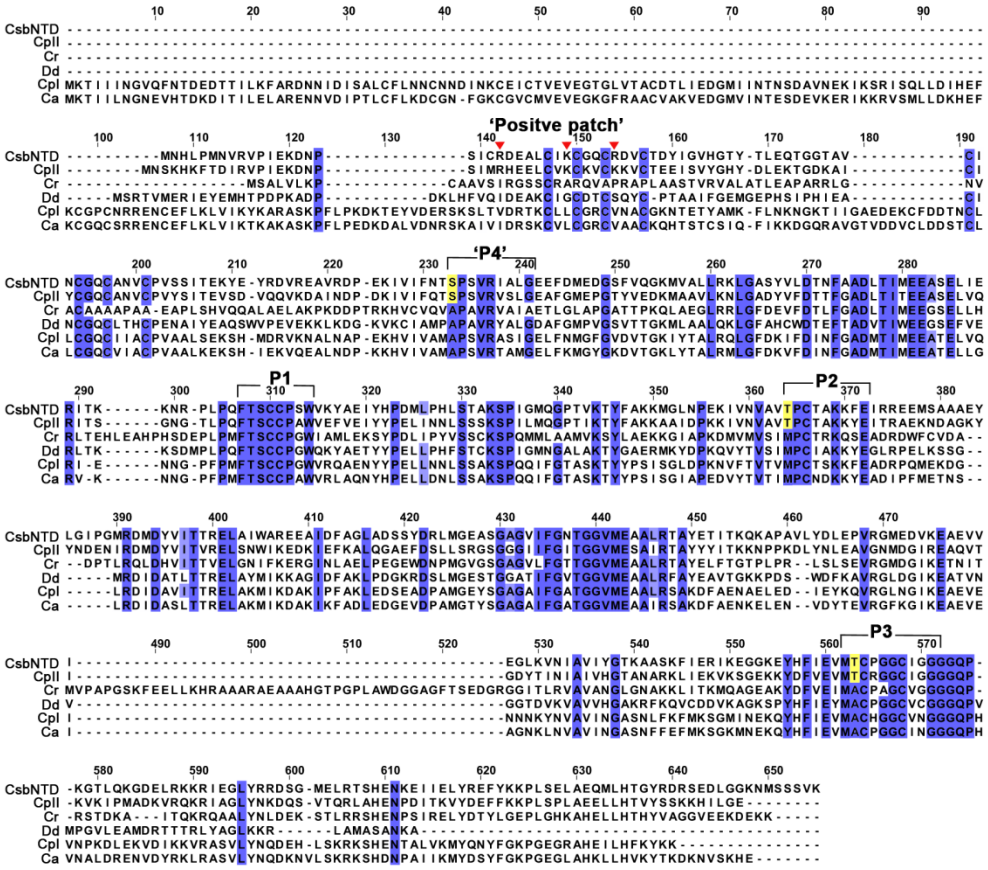

Figure III-19. Sequence alignment reveals conserved substitutions near H-cluster and [4Fe-4S] cluster motifs. Alignment of N-terminal domain of *Cs*HydY with structurally characterized [FeFe]-H_2ases *C. reinhardtii* (*Cr*), *D. desulfuricans* (*Dd*) and *C. pasteurianum* I (*Cp*I) or biochemically characterized [FeFe]-H_2ases *C. acetobutylicum* (*Ca*) and *C. pasteurianum* II (*Cp*II). MUSCLE alignments were visualized by Jalview and residues are colored by sequence identity, with intensity color increment of 100%. Conserved motifs for the H-cluster domain are boxed: P1,TSCCPxW; P2,MPCxxKxxE; P3, ExMACxxGCxxG; and previously unidentified 'P4,' APxVR. Both *Cp*II and HydY show similar substitutions in P1, P3 and P4 (yellow boxes) motifs. A 'positive patch' of Arg and Lys residues (red triangles) within the F-cluster domain is also found in HydY and *Cp*II.

substitution of Met to Thr was found in all identified HydY homologs (Figure III-20b). This methionine residue (M353, all numbering according to PDB:3C8Y[204]), is positioned beneath the μ-CO, and is within van der Walls contact (Figure III-18). A mostly conserved Ala to Thr substitution was also identified in the P3 motif, which is

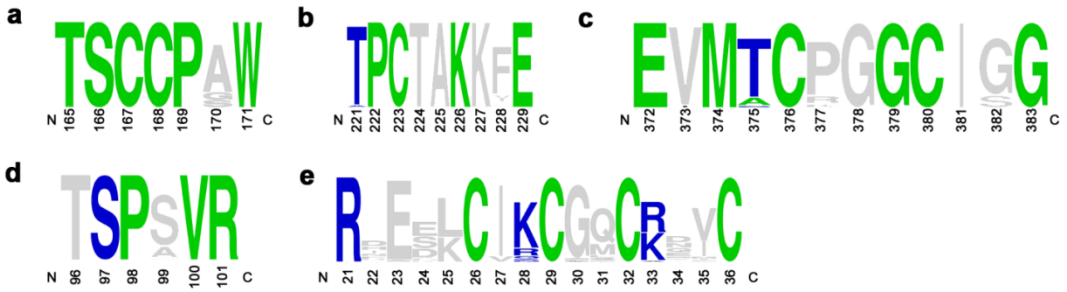

Figure III-20. Sequence logos of HydY homologs reveal conservation of hydrophilic substitutions within H-cluster and F-cluster motifs. Green one letter codes indicate conservation in HydY that are identical to well-characterized [FeFe]-H_2ases. Blue codes indicate conservation in HydY homologs that are different in typical [FeFe]-H_2ases, and grey indicate variable regions. b) P1 motif is completely conserved. c) P2 motif contains a mostly conserved Thr substituted for Met, which is within VDW contact of bridging CO (PDBID: 3C8Y). d) P3 motif contains a mostly conserved Thr→Ala substitution, which would be near the cubane cluster of $[4Fe\text{-}4S]_H$. e) HydY homologs contain completely conserved Ala→Ser substitution. This Ala is within 3 Å of bridging CO. f) A positive patch of mostly conserved Arg/Lys/Gln near a [4Fe-4S] motif.

positioned near the cubane cluster of the H-cluster (Figure III-20c). In addition, another important sequence near the H-cluster was identified, which we call P4: APxVR. A230 is positioned beneath the μ-CO, which provides a hydrophobic pocket near the H-cluster. A conserved Ser substituted for Ala in all HydY and CpII sequences (Figure III-20d). These hydrophilic substitutions near the H-cluster could likely have drastic effects on catalysis.[223] Lastly, additional 'positive patch' variants were identified within the F-domain that could cause substantial attenuation of redox potentials of one, or both, clusters within the F-domain (Figure III-20e). Indeed, the two [4Fe-4S] cluster potentials of CpII, which contain the positive patch substitutions in the F-domain, were determined to be -180 and -300 mV.[235]

Discussion

We have reported on the first study on a homodimeric [FeFe]-H_2ase rubrerythrin fusion from the anaerobe *C. symbiosum*, called HydY, which performs two seemingly dichotomous reactions: H^+ reduction/H_2 oxidation and H_2O_2 reduction. The CTD of HydY is the site for H_2O_2 reduction, and is a highly efficient peroxidase (k_{cat}/K_m 1.1x10^7 M^{-1} s^{-1}). Multiple spectroscopic tools indicate that the CTD binds a diiron site, with Mössbauer assigning it as a rubrerythrin-like. The NTD of HydY has high sequence identity (38-44%) to the well-studied [FeFe]-H_2ase, such as Cr or Dd, and is the site for hydrogenase activity.

Using a coupled biochemical and electrochemical approach, HydY (via the CTD) was found to catalytically reduce H_2O_2. Rbrs preferentially react with H_2O_2 and sluggishly reduce O_2.[128] A recent report with a reverse domain orientated Rbr, i.e. Rd-Rbr, was found to have an increased reactivity with O_2, but still maintained substrate preference for H_2O_2.[152] No di-rubredoxin, to our knowledge has been reported. Cyclic voltammograms with $HydY^{IM}$, in the presence of H_2O_2, show catalytic, reductive currents at potentials ≤ +100 mV (Figure III-3). The E_{onset} measured for $HydY^{IM}$ is much more negative than those measured for typical Rbrs. Reductive titrations with *Dv*Rbr have determined mid-point potentials +150 to +230 mV for either the diiron or FeS_4 Rd-like sites.[150,227] Rd proteins, i.e. those not found as chimeras with Rbrs, have mid-point potentials of ~ 0 mV.[150] This hints at a lowered reduction potential for the CTD. Further work must be done to understand this apparent negative redox potential shift.

Our results indicate HydY functions differently than standard [FeFe]-H_2ases: H^+ reduction is inhibited by H_2 and it readily consumes H_2. Solution assays with methyl viologen (-450 mV) present the case that HydY is a poor catalyst for both H^+ reduction and H_2 uptake. Replacing the electron donor with methylene blue (+12 mV) makes HydY a more active enzyme for H_2 oxidation. Reports by Adams and Mortenson show *Cp*II also show this same 'bias' toward H_2 oxidation, where *Cp*II was speculated to be a poor H^+ reduction catalyst because H_2 removal was rate limiting.[74] Cyclic voltammograms of HydY further enhance the understanding of this reactivity. Under 1 atm of H_2 and near the H^+/H_2 couple (-420 mV), the maturated HydY constructs show minimal catalytic currents. At +20 mV, all the maturated HydY constructs show near maximal oxidative currents. These results illustrate that HydY requires an overpotential for H_2ase activity indicating that electron transfer is rate-limiting,[98] contrasting with standard [FeFe]-H_2ases.[7]

The electrochemical results presented for HydY contrast with those of typical [FeFe]-H_2ases. For example, HydY displays a bias for H_2 oxidation (25) that is likely due product (H_2) inhibition. Under similar conditions, standard [FeFe]-H_2ases have reported biases of 0.4 (hydrogen oxidation/protein reduction activities) for *Ca* and 2 for *C*r, whereas standard a [NiFe]-H_2ase displayed a bias of ~12 and O_2-tolerant varieties were even more biased toward H_2 oxidation.[98] The mechanism for bias is complex,[98,234] but appears to not be influenced by active site chemistry. $HydY^s$ and NTD^s display anaerobic reactivation (E_{switch})[85] values of +120 mV. E_{switch} is a qualitative parameter[34,236] used to describe anaerobic oxidative inactivation observed for H_2ases. In

comparison, under similar conditions E_{switch} values for Dd[FeFe]-H_2ase were +10 mV, while O_2-tolerant [NiFe]-H_2ases were +100 mV.[34] E_{switch} was originally hypothesized to be over oxidation for [FeFe]-H_2ases, similar to $H_{ox}^{inactive}$,[94] but a recent study suggests anaerobic inactivation involves a more complex mechanism.[237] Regardless of the species formed under oxidizing conditions, HydY and standard [FeFe]-H_2ases display clearly different electrocatalytic profiles.

Tuning activity of [FeFe]-H_2ases is mediated by active site residues.[223] In fact, recent studies of apo and maturated *Cp*I with various synthetic $2Fe_H$ complexes[118,238] indicate the protein matrix induces the H-cluster into the active, 'rotated' isomer.[239] Interestingly, substitutions of Leu for Met in P2 or P3 resulted in a drastic decrease in activity.[223] Additionally, recent spectroscopic[240] and electrochemical[237] investigations support a model for H-cluster isomerization. Mechanisms for these isomerizations remain unclear, but highlight the importance of second-shell interactions for H-cluster stability and catalytic activity. HydY homologs contain conserved substitutions with H-cluster and [4Fe-4S] cluster binding motifs (Figures III-19&20). We hypothesize that variants identified herein are the determinants for marked catalytic differences of HydY, and likely *Cp*II, with positive patch substitutions largely affecting the catalytic bias.[98]

We propose that *Cs*HydY acts in recycling H_2[5] generated by prototypical [FeFe]-H_2ases[3] and transfers reducing equivalents directly to the CTD active site for H_2O_2 reduction (Figure III-21). Typical anaerobic bacteria operate under reducing redox potentials, allowing for multiple copies (4 in *C. symbiosum*; 6 in human pathogen *C. perfringens*) of [FeFe]-H_2ases to presumably be active in H_2 production; HydY would be

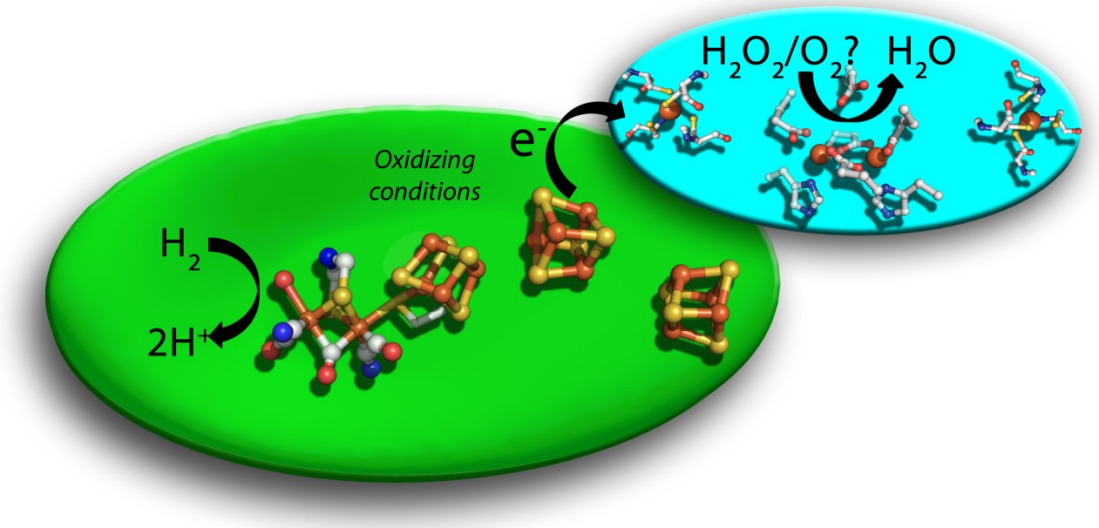

Figure III-21. Model of H_2-dependent peroxidase role of HydY. Under typical, reducing cellular conditions, HydY is inactive. An oxidative shift (caused by ROS) activates the NTD and triggers oxidation of excess H_2 that was generated during anaerobic metabolism. Reducing equivalents recycled from H_2 are directly transferred to CTD for H_2O_2, and maybe O_2, reduction.

inactive under these typical cellular conditions. ROS stress, however, would disrupt anaerobic metabolism and shift cellular potentials more positive, signaling for oxidative stress response via perR and similar genes.[124] This oxidative shift would trigger HydY for H_2 oxidation, consequently allowing for efficient H_2O_2 scavenging by the CTD. Upon removal of ROS, the anaerobe would return to reducing, homeostatic conditions and HydY would be inactive due to the inhibition of H_2. The conservation of substitutions within H-cluster binding motifs suggests that all HydYs function similarly. We hypothesize that HydY enzymes catalyze H_2-dependent reduction of H_2O_2 (Class I) or an unknown substrate (Class III). The class II HydY from *Robinsellia sp*. RH5 contains a glutamate synthase (GS) domain would use H_2 as a reductant, in lieu of NAD(P)H or reduced ferredoxin.

Overall, we have characterized a novel [FeFe]-H_2ase rubrerythrin fusion, called HydY, that is biased toward H_2 oxidation. Our evidence suggests that HydY is capable of transferring reducing equivalents generated from H_2 oxidation directly to the rubrerythrin domain for H_2O_2 reduction, i.e. H_2-dependent H_2O_2 reduction. We have identified possible determinants for the bias and apparent overpotential requirement of HydY. Elucidating and understanding the factors that tune H_2ase chemistry may lead to the better design of small molecule compounds that could have greater implications in energy production.

CHAPTER IV

INVESTIGATION OF SECOND-SHELL CONTRIBUTIONS FOR HYDY CATALYSIS

Introduction

Hydrogenases reversibly catalyze conversion of dihydrogen into protons and electrons, with many that exhibit turnover frequencies exceeding 1,000 s^{-1}.[219,220] The three classes of hydrogenases (H_2ases) are named by the metals employed at the active site, nominally [FeFe]-, [NiFe]- and [Fe]-H_2ases Though phylogenetically distinct,[2,3] H_2ase active sites are characterized by their low oxidation and spin states stabilized by unique CO and CN^- ligands. The [FeFe]-H_2ase is the superior catalyst.[38]

The active site of [FeFe]-H_2ases, as originally revealed by the Peters, *et al*[241] and Nicolet, *et al,*[67,242] utilizes a complex organometallic cofactor called the H-cluster, comprised of a cubane [4Fe-4S] cluster ($[4Fe\text{-}4S]_H$) bridged by a cysteine thiolate to a diiron subcluster ($[2Fe]_H$). These irons are referred to as proximal (Fe_p) or distal (Fe_d), relative to their position to the cubane cluster. Each iron of the $[2Fe]_H$ coordinates a terminal CO and CN^-, along with a bridging CO, and a bridging dithiolate ligand (Figure 1). This pendant ligand has been modeled as a propandithiolate[241,243], dithiomethylether[244], and dithiomethylamine. Theoretical[245], spectroscopic[246], and, most recently, biomimetic[60] studies have unequivocally proven the bridgehead atom to be nitrogen. Spectroscopic results have found that exogenous CO inhibits [FeFe]-H_2ases by binding to the open coordination site of Fe_d, indicating this is the active site metal. The CN^- ligands are likely held in place by H-bonds from the protein backbone, while the

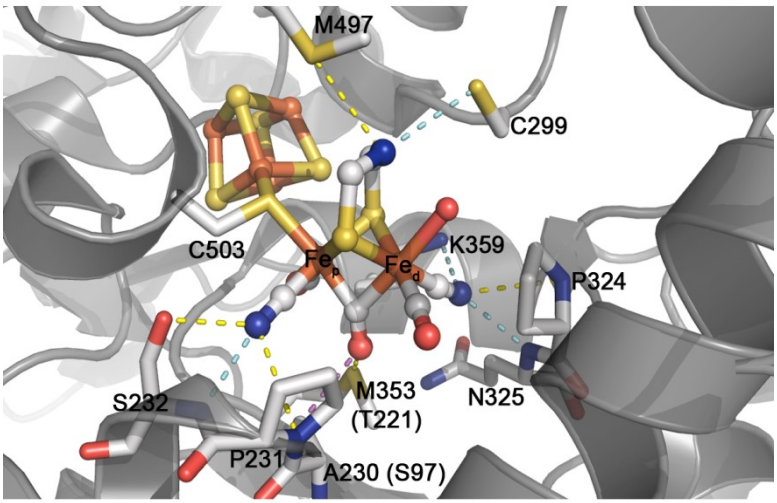

Figure IV-1. Crystallographic model of the [FeFe]-H_2ase active site taken from the structure of *Cp*I (PDB 3C8Y). Interactions from protein to $[2Fe]_H$ are depicted as: yellow, polar interactions; blue, hydrogen bonds; magenta, hydrophobic interactions. Note, the bridgehead was changed from O to N to reflect current literature.

CO ligands are free within relatively hydrophobic pockets (Figure IV-1).[238,241,247] Four highly conserved motifs within this protein pocket – TSCCPxW (P1), $MPCx_2Kx_2E$ (P2), $ExMACx_2GCx_2G_3xP$ (P3) and APx_2R (P4) – contribute second-shell interactions to the $[2Fe]_H$. Mutation of Cys within P1 has revealed it as the likely proton donor,[223,233] whereas substitutions of Leu for Met in P2 or P3 or Arg for Lys in P2 resulted in drastically decreased H-cluster incorporation.[223]

The mechanism of [FeFe]-H_2ases stem mostly from contributions using FTIR and EPR spectroscopy. Both $[4Fe\text{-}4S]_H$ and $[2Fe]_H$ are redox active. The $[4Fe\text{-}4S]_H$ cycles between the oxidized $[4Fe\text{-}4S]^{2+}$ and EPR-active reduced $[4Fe\text{-}4S]^{+}$ states, whereas the $[2Fe]_H$ can either be: overoxidized, Fe(II)Fe(II); oxidized Fe(I)Fe(II); or reduced, Fe(I)Fe(I). Only the oxidized $[2Fe]_H$ state is EPR active. Spectroscopic studies

indicate the catalytically active, resting state forms of [FeFe]-H_2ases are the H_{ox} ([4Fe-4S]$^{2+}$Fe(I)Fe(II)) and H_{red} ([4Fe-4S]$^{2+}$Fe(I)Fe(I)) states,[7] each that bear characteristic FTIR bands. An additional state, the so-called H_{sred},[248] consists of [4Fe-4S]$^{+}$Fe(I)Fe(I) state. H_{sred} accumulates in some [FeFe]-H_2ases[248,249] and is likely transiently formed during catalysis. A simple proton-coupled mechanism, then, can be assumed to form a hydride intermediate [Fe(I)Fe(II)(H^-)] followed by the formation of H_2, forming a transient (Fe(I)Fe(II)H_2) species.[245]

We recently reported on [FeFe]-H_2ase fusion protein, called HydY, which had near uni-directional H_2 uptake activity, contrasting with typical [FeFe]-H_2ases. All HydY homologs contain conserved substitutions in conserved H-cluster domain binding residues. We speculated that the conserved Ala to Ser mutation in P4 (S97, numbering according to HydY residues) and Thr to Met in P2 (T221) significantly contributed to the unique properties observed for HydY. We found that these conserved residues within the second-shell sphere of $[2Fe]_H$ appear to tune catalysis of the H-cluster by H-bonding directly to CO and CN^- ligands. We speculate that the μ-CO is the 'hotspot' for [FeFe]-H_2ase catalysis.

Results

FTIR Spectroscopy

The N-terminal domain (NTD) of HydY was purified and exhibited a similar catalytic bias as previous batches (turnover number for H_2 oxidation of 4,500 min^{-1} and 2.4 ± 0.2 min^{-1} for H_2 production). To examine the potential molecular determinants for this surprising lack of H^+ reduction for HydY, Fourier transform infrared (FTIR)

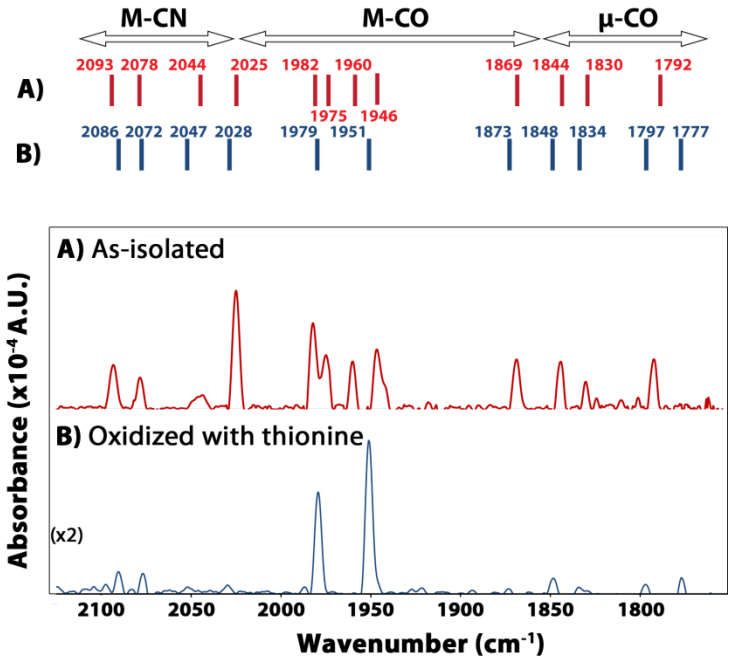

Figure IV-2. FTIR spectra NTD in as-isolated (a) and oxidized (b) conditions. All spectra were subtracted from reference sample with buffer only. Experimental conditions: temperature, 21 °C; resolution, cm^{-1}; number of sample scans, 1024; protein concentration, 700 μM.

spectroscopic analysis was performed. The IR spectrum in the 1750-2150 cm^{-1} range identifies stretching modes for CO and CN^- of the $[2Fe]_H$, and these ligands are sensitive to redox state of the H-cluster. [FeFe]-H_2ases are incredibly sensitive to O_2, and HydY appears no different. A reductant, sodium dithionite (NaDT), is added to purifications of HydY to minimize O_2-induced inactivation. As-isolated NTD[e], which contained 2 mM NaDT, produced a complex FTIR spectrum (Figure IV-2). The obtained spectrum displayed major stretching modes that are similar to an H_{red}-like state. This includes a bridging CO (μ-CO) at 1792 cm^{-1} and terminally coordinated CN ligands at 2093 and 2078 cm^{-1}. However, expected stretching modes for terminal CO ligands (1916-1935 and

1891-1894 cm^{-1})[7,250-252] are not present. Instead, multiple lower energy stretching modes (1830-1869 cm^{-1}) and higher energy modes (1960-2025 cm^{-1}) are observed. These stretches are most similar to those detected for inactivated states of *Dd*,[253] but have not been reported for clostridial H_2ases.[254] This spectrum suggests as-isolated NTD^e, in the presence of NaDT, exists primarily either in H_{red} or H_{inact}. The concentration of NaDT used was only in slight excess to protein (800 μM), and O_2 induced inactivation cannot be ruled out since the FTIR spectrometer used was outside of the glovebox.

To deconvolute the multiple states observed for the as-isolated sample, NTD^e was incubated with a ten-fold excess of thionine (E' = 16 mV vs SHE) (Figure V-2b). Previous studies have found addition of thionine results in the formation of H_{ox}.[250,253,255-258] Consistent with these studies, the obtained spectrum of oxidized NTD^e displays stretching modes for terminal CN^- ligands[251] at 2072 and 2086 cm^{-1} and major stretching modes for terminally ligated CO at 1951 and 1979 (H_{ox} terminal CO stretching modes typically 1940 and 1965 cm^{-1})[7,251,253]. The stretching mode for the μ-CO was detected at 1797 cm^{-1}, several wavenumbers blue-shifted compared to previously reported values.[7,253] Weaker stretching modes were also detected from 1834, 1848, 1873, 2028 and 2047 cm^{-1} that are difficult to assign. It is currently unclear if these peaks correspond to authentic stretching modes or represent poor data analysis. Taken together, these initial FTIR studies on NTD^e suggest that second-shell contributions near the $[2Fe]_H$ influence stretching modes for CO and CN^- in manners not observed for classical [FeFe]-H_2ases.

Table IV-1. Solution activity measurements for NTD and variants.

	H_2 oxidation		H^+ reduction	
Variant	Turnover number (min^{-1})	% of WT	Turnover number (min^{-1})	% of WT
NTD -WT	4500	100	2.4 ± 0.2	100
NTDS97A	600 ± 50	13	5.8 ± 0.1	240
NTD97A/T221M	400 ± 100	8.9	ND[a]	-

[a]ND, not determined.

Solution characterization of NTD substitutions

The NTD of *Cs*HydY, and all HydY homologs, contains multiple hydrophilic substitutions within conserved motifs of [FeFe]-H_2ases. The Met residue within P2 ($MPCx_2Kx_2E$) resides beneath the μ-CO in structures of [FeFe]-H_2ases, and the Ala residue within the so-called P4 motif appears to create a hydrophobic pocket at the μ-CO as well. HydY homologs have a Met to Thr substitution in P2 and an Ala to Ser substitution in P4. In order to investigate the role of these conserved substitutions in catalysis, we attempted to 'evolve' *Cs*HydY back to a typical [FeFe]-H_2ase by creating single (S97A) and double (S97A/T221M) NTD mutants. The purified variants both exhibited the expected amounts of Fe and S atoms (11 and 12, respectively) and appeared to migrate as monomers on gel filtration columns, similar to native NTD.

Solution activity measurements of the NTD variants revealed dramatic differences compared to native NTD (Table IV-1). In the standard methylene blue assay with H_2-saturated buffer, the S97A variant exhibited a H_2 oxidation turnover number of

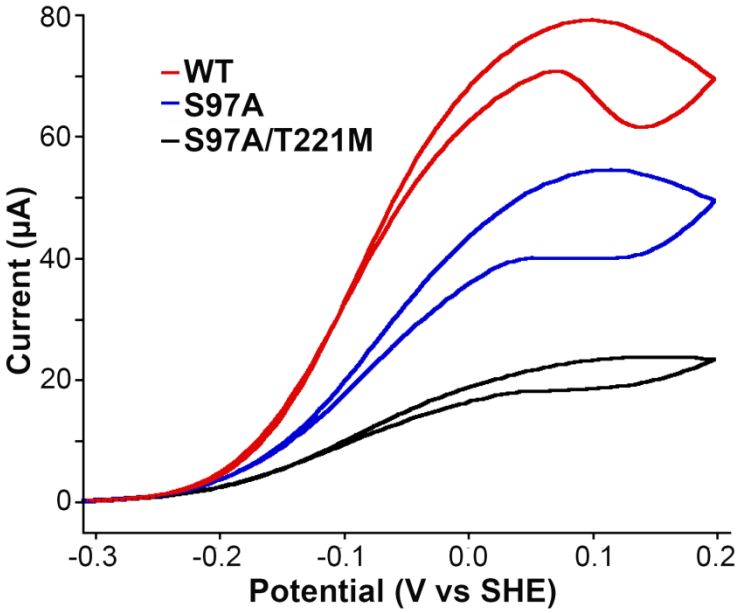

Figure IV-3. HydY variants exhibit starkly different electrocatalytic profiles. A new batch of purified wild-type HydY (red) shows activity similar to that reported previously. NTDS97A (blue) and NTDS97A/T221M (black) display decreased resistance to oxidative inactivation and decrease H_2 oxidation activity. Experimental conditions include: electrode rotation rate 2750 rpm, 1 atm 100% H_2, 5 mV s^{-1} scan rate, and phospate buffer pH 7.0.

600 ± 50 min^{-1}. This is 13% of the wild-type activity. The double NTD variant, S97A/T221M, exhibited even slower H_2 oxidation turnover number (400 ± 100 min^{-1}), or 8.9% of the wild-type activity. Interestingly, the H_2 evolution activity of S97A increased 2.4 fold (5.8 ± 0.1 min^{-1}). We were unable to consistently measure H_2 evolution for the double mutant, however. The changes in activity for these variants can be explained by substitutions in the active site resulting in poor $[2Fe]_H$ incorporation or directly impacting catalysis.

Interrogation of NTD constructs by PFE

PFE was used to further investigate the roles of active site substitutions. In the presence of H_2, positive currents representing H_2 oxidation were not observed until the potential was ~+100 mV more positive than the $2H^+/H_2$ couple (E_{eq} = -420 mV vs SHE at pH 7.0), as described previously for *Cs*NTD (Figure IV-3). No H^+ reduction is observed due to the small redox window (-300 to + 150 mV vs SHE). At more oxidizing potentials, all NTD variants undergo anaerobic inactivation and then reductive reactivation as the potential is swept to more reducing conditions. This rate of anaerobic inactivation occurs most significantly for NTDS97A/T221M (black), then NTDS97A, and finally wild-type NTD (red). This suggests that all NTD constructs form an inactivated species, but evolving NTD back to a traditional [FeFe]-H_2ase results in a protein that is more susceptible to anaerobic inactivation. Oxidative inactivation/reductive reactivation is also pH dependent for the active site substitution constructs, with more inactivation occurring at lower pH, as observed for wild-type NTD (Figure IV-4). Surprisingly, NTDS97A/T221M begins to show fairly significant H^+ reduction currents in these studies (Figure V-4b). This indicates that the conserved active site substitutions favor the enzymes toward H_2 oxidation.

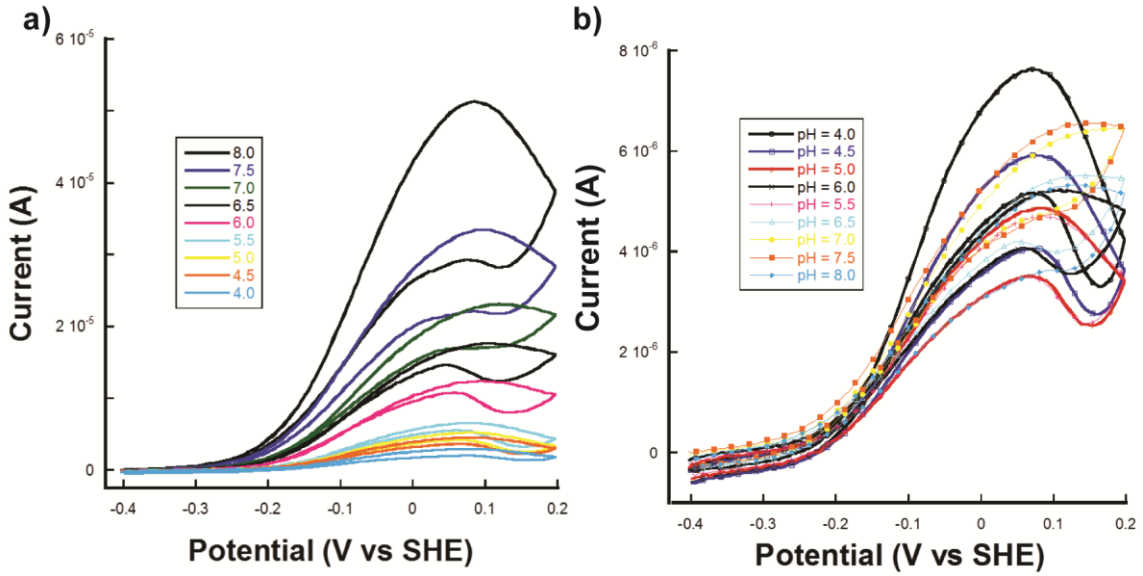

Figure IV-4. Electrocatalytic profiles of NTDS97A (a) and NTDS97A/T221M (b) vs pH in the presences of 1 atm of 100% H_2. The legend indicates the pH of the 0.1 M phosphate buffer with 0.15 M KCl. Other experimental conditions include: electrode rotation rate 2750 rpm and a 5 mV s^{-1} scan rate.

Previous studies of HydY suggested that the conserved second-shell substitutions resulted in an [FeFe]-H_2ase that had a lower H^+ reduction inhibition constant for H_2 and a significantly higher K_m for H_2 than typical [FeFe]-H_2ases. We used time-dependent PFE to measure the apparent K_m for H_2 for the NTD constructs.[83,96,202] In a typical PFE experimental set-up, an H_2ase is absorbed onto a rotating electrode that is submerged in a buffer with H_2 directly bubbling into the apparatus. Under these conditions, if the potential is set to favor oxidation of substrate, and H_2 gas is switched to N_2 or Ar gas, then the measured current can be described by equation 1: $i_{max} = \frac{i(t)}{1+\frac{K_m}{C_{H2}(0)}\exp(t/\tau)}$ where i(t) is the current at any given time, K_m is the Michaelis-Menten complex, $C_{H2}(0)$ is the concentration of H_2 at time point zero (~0.78 mM at 1 atm 100% H_2), and τ is the time

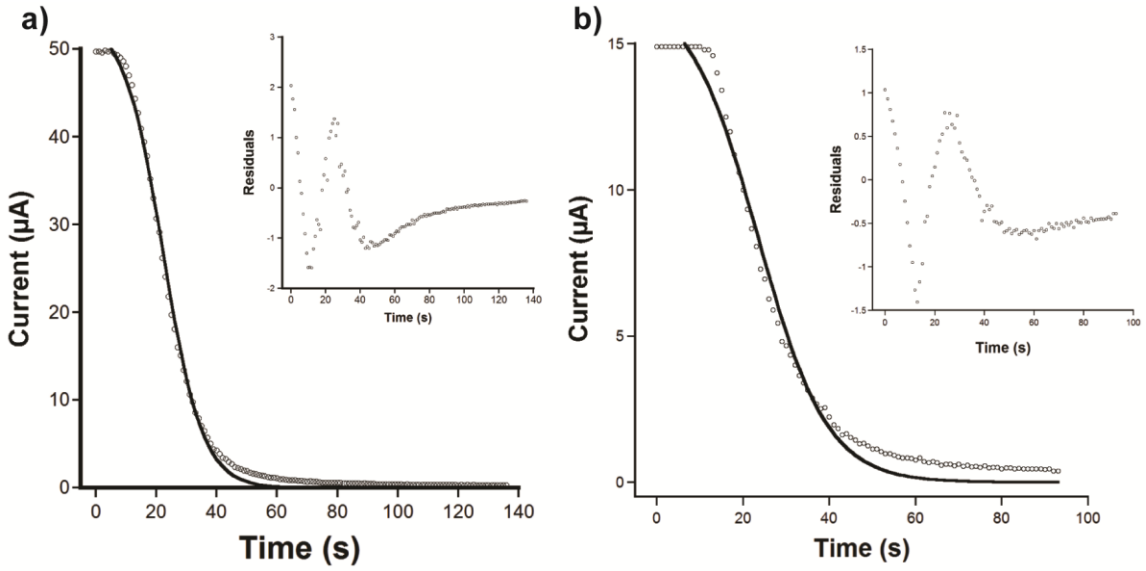

Figure IV-5. Transient catalytic current measured for H_2 oxidation by wild-type HydY (a) and NTDS97A/T221M (b), following the electrochemical cell being flushed with N_2. Inset reveals the residual plot after fitting with equation IV-1. Experimental conditions: *E*, 0 mV; rotation rate, 2750 rpm; temperature, 21°C.

constant for H_2 to dissipate from the electrode surface and diffuse out of the electrochemical cell.[96,202] Indeed, a sigmoidal response is observed for both HydY and NTDS97A/T221M (Figure V-5). For wild-type HydY, an average K_m of 13 ± 2 μM was measured, whereas NTDS97A/T221M was found to increase four-fold to 43 ± 8. As can be seen from the residual plots (Figure V-5, inset), the fits for this data show systematic errors, suggesting this model does is not accurate in depicting this data. No K_m was reproducibly fit for NTDS97A. However, this data further suggests that active site substitutions effect chemistry at the $[2Fe]_H$.

Computational investigation for hydrophilic active site substitutions

Figure V-6 displays our computational model of the H-cluster before H_2 formation. Using the coordinates from PDB 3C8Y, the geometries were optimized

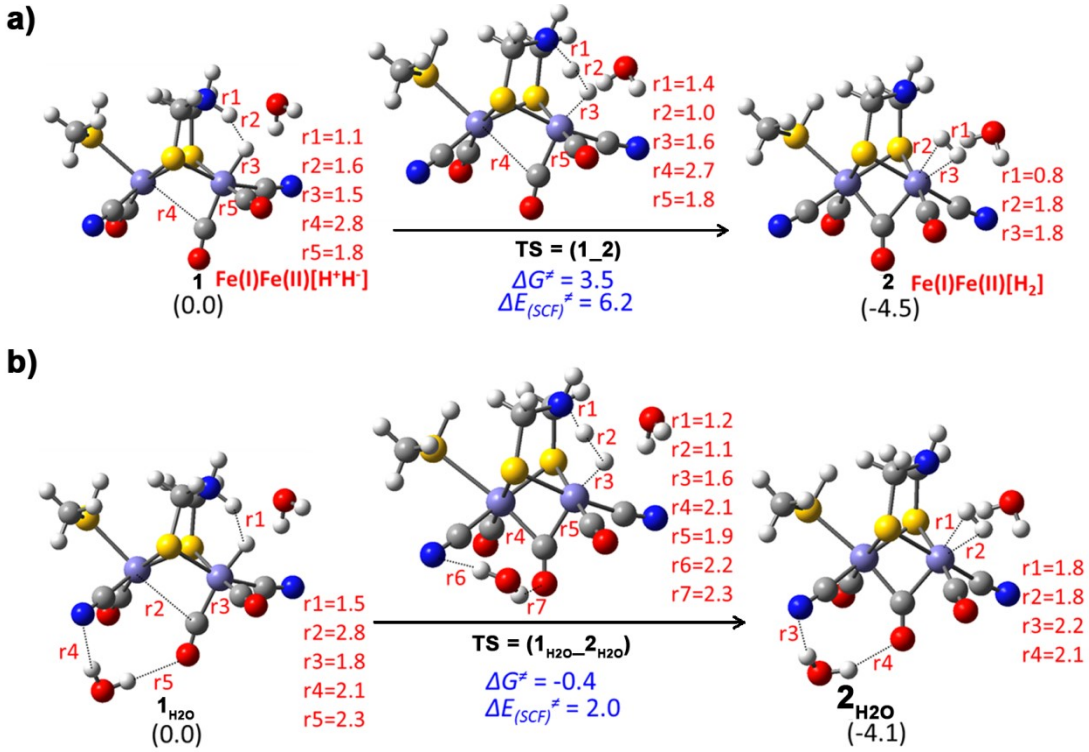

Figure IV-6. Optimized structures of Fe(I)Fe(II)[H$^-$] in wild-type (a) and with water (b) modeling NTDS97. The labels r1-r5 refer to bond distances in Å, and energies are in kcal/mol.

assuming [Fe(I)Fe(II)(H$^-$)] state in wild-type conditions (**1**, Figure V-6a). HydY contains an Ala to Ser substitution (S97), located near the μ-CO X-ray structures (Figure IV-I). This Ser substitution was modeled into the active site as a water molecule, and then geometry optimized (**1$_{H2O}$**, Figure V-6b). The bond distances for this transient hydride complex are remarkably similar, including the distances for Fe$_p$---μ-CO (2.8 Å) and Fe$_d$---μ-CO (1.8 Å). The relative energies of the protonated adduct, analogous to [Fe(I)Fe(II)(H$_2$)] (**2** and **2$_{H2O}$**, respectively), and the transition state are similar. Additionally, there is relatively little difference in the energy between **2** and **2$_{H2O}$**.

Surprisingly, the transition state energy for $\mathbf{2_{H2O}}$ (-0.4 kcal/mol) is significantly decreased compared to **2**. This result suggests that H-bonds near the $[2Fe]_H$ affect active site chemistry by making H_2 cleavage more favorable.

Discussion

The active site of [FeFe]-H_2ases appear finely tuned for its activity: reversibly producing and consuming H_2. Using only iron, this metallocofactor amazingly tunes the acidity of iron through a complex process of π-accepting and σ-donating abiotic CO and CN^- ligands for thousands of turnovers per second.[7,259] The CN^- ligands are likely held in place by H-bonds from the protein backbone, while the CO ligands are free within relatively hydrophobic pockets.[238,241,247] The unique pendant amine[7,60] of the $[2Fe]_H$ is positioned to act as a general base during catalysis.[245] Relatively little information exists for second-shell interaction of the $[2Fe]_H$, though. Mutational studies indicate a cysteine near the pendant amine functions as a general base.[223,233] Substitutions of conserved methionines for leucines in the $[2Fe]_H$ resulted in drastically decreased solution activity, but no substantive effect in electrochemistry, suggesting decreased H-cluster incorporation. Additionally, loss of a conserved lysine in the P2 motif resulted in no incorporation of H-cluster whatsoever.[223] Clearly, the environment around the H-cluster facilitates this enzymes' catalysis, but mutagenesis studies have only revealed minor contributions[58] of the second-shell interactions.

Analysis NTD, and several engineered variants, indicates that second-shell contributions to the CO and CN^- ligands of the $[2Fe]_H$ result in large perturbations in spectroscopic and catalytic properties. H-bonding residues in HydY cause a shift in

FTIR stretching modes, and loss of H-bonds causes a substantive change in observed catalytic rates. Neither wild-type HydY nor NTDS97A display much H^+ reduction or reversible catalysis;[98] however, NTD97A/T221M begins to display near reversible catalysis. Interestingly, PFE of the NTD variants also resulted in an increased susceptibility to oxidative inactivation, with NTD97A/T221M inactivating like traditional [FeFe]-H_2ases.[34,83] This indicates second-shell contributions from the protein influence catalytic properties of the cofactor.

FTIR of NTD in reduced and oxidized reveals unsuspected stretching modes. Bands in the as-isolated state were attributed to the H_{red} state [Fe(I)Fe(I)], however additional stretching modes were observed from 1830-1869 cm^{-1}, as well as modes from 2025-2044. These stretches lie between a terminal CO and μ-CO and terminal CN/CO stretching frequencies (Figure IV-2). We tentatively assign these peaks to effects of H-bonding to the $[2Fe]_H$. No FTIR data was collected on mutants of NTD, so further work is needed to better understand this interaction.

Computational modeling of H-bonding interactions near the $[2Fe]_H$ indicate a significant effect upon catalysis. Modeling of a single water molecule near the μ-CO resulted in apparent H-bonds to both CN^- ligated to Fe_p (2.1 Å) and μ-CO (2.3 Å). Such an interaction aids in the interpretation of shifted IR vibrational signatures for both CO and CN^-. Additionally, the transition state for H_2 formation decreased from 3.5 kcal/mol to -0.4 kcal/mol (Figure IV-6). This results suggest that a hydrogen bond near the μ-CO of the $[2Fe]_H$ causes the [FeFe]-H_2ase to be a uni-directional enzyme by significantly decreasing the activation energy for cleave of the dihydrogen bond. While potentially

aligning with both the solution and electrochemical results, further studies are needed to fully understand the mechanistic implications of the conserved substitutions found in HydY homologs.

We have undertaken additional studies to elaborate the mechanistic determinants for the catalytic bias of HydY homologs. Suspected H-bonding residues conserved in HydY were found to affect not only IR vibrational signatures of CO and CN^- ligands, but also catalytic properties that can be explained by withdrawing electron density of the H-cluster, therefore favoring H_2 oxidation. Since HydY contains a μ-CO, additional studies mimicking this interaction with small molecules may lead to the development of more stable rotated $[2Fe]_H$ mimics[239] that may have implications for hydrogen-based fuel cells.

CHAPTER V

STRUCTURAL INVESTIGATION OF CTD

Introduction

Life emerged on Earth some 3.5 billion years ago, when the early biosphere was highly reducing, containing mostly methane, dihydrogen and carbon dioxide and lacked significant O_2 concentrations, very different than it is today.[260] Following the transformative 'Great Oxidation Event' roughly 2.4 billion ago,[261] the biosphere shifted to a much increased oxygen atmosphere, driven mostly by oxygenic photosynthesis from cyanobacteria. This increased presence of O_2 significantly shifted the metabolic pathways of existing bacteria, and likely gave rise to entirely new metabolic pathways. Concomitant with the rise of oxygen was also the rise of deleterious reactive oxygen species (ROS), i.e. superoxide, hydrogen peroxide and hydroxyl radical.[136] Life then required antioxidant systems and enzymes to protect against the side effects of now living in oxygen.

Aerobic bacteria and higher organisms harness the oxidizing potential of O_2, but production of ROS is still a strong possibility.[120-122] A large number of enzymes are utilized by these organisms to avoid ROS-induced death. These systems mainly include superoxide dismutases and catalases, but also a large class of various peroxidases that reduce H_2O_2 using external reducing equivalents.[127] For anaerobic bacteria, that is bacteria that lack oxidative phosphorylation metabolic pathways, encountering O_2 arrests growth and often leads to cellular death.[120,127,262] Anaerobic bacteria, then, appear to use an 'all hands on deck' approach to survive O_2 exposure. Along with the above

mentioned antioxidant enzymes, strict anaerobes also employ two enzymes specific to anaerobes, namely superoxide reductase (SOR) and rubrerythrin (Rbr).[127,128,263] Superoxide reductase reduces superoxide, instead of regenerating the dangerous O_2 molecule, whereas Rbr functions as a peroxidase.[128,136,148] Recent observations reveal these two proteins act *in vivo* in concert, where the H_2O_2 produced from SOR is reduced directly by Rbr. A bevy of *in vivo*[121,124,143,152,158,160,161,164,264] and *in vitro*[152,156,164,167] results affirm that Rbr functions as an NADH-dependent peroxidase, in the presence of NADH:rubredoxin oxidoreductase and a rubredoxin (Rd) (equation **12**).

$$NADH + H^+ + H_2O_2 \rightarrow 2\ H_2O \qquad (\mathbf{12})$$

Rubrerythrins are characterized by their combination of domains, both of which contain a metal center. The smaller metal-binding domain, classically located at the C-terminus, contains a $Cx_2Cx_{10}Cx_2C$ that binds a single, tetrahedral iron atom. A recently identified N-terminal Rd Rbr protein (called reverse Rbr or RevRbr) was identified that is up-regulated upon O_2 stress. The larger domain, classically located at the N-terminus, is comprised of four helix bundle domain with two pairs of $Ex_{29\text{-}37}Ex_2H$ motifs that ligate a non-heme, oxo-bridged diiron site similar to methane monooxygenase (MMOH) and ribonucleotide reductase (RNR). However, no homologous O_2 activation chemistry has been reported for Rbr. Instead, numerous studies present evidence that the diiron site reacts specifically with H_2O_2 (millisecond to second time scale) and to a much lesser extent O_2 (minutes time scale).[154,155] The RevRbr was shown to have an increased reactivity to O_2 in comparison to classical Rbr, and the molecular basis for this increased

reactivity is currently unknown. The function of the Rd domains, either N- or C-terminal, is presumed to transfer electrons to the diiron site during catalysis.

The mechanism of rubrerythrins is deduced mostly from the crystal structures.[128,169] The iron sites of Rbr are surprisingly high (E' > +200 mV vs SHE)[150,228], so the resting state of Rbrs is diferrous. In the diferrous state, the coordination geometry is pseudo-octahedral, with two bridging Glu residues, axial histidines and two axial solvent molecules (Figure V-1). Upon oxidation, Fe1 is shown to 'toggle' 2.2 Å, replacing a histidine (His off) with the 7th Glu (Glu on). This redox-dependent toggling must occur at least as fast as the turnover number (up 2,000 min^{-1}) and has been observed at cryogenic temperatures.[179,265] This redox toggle has only been observed in Rbr homologs and can be considered a defining characteristic of this protein family.[128] Additionally, a water molecule bridges the diiron site, which was confirmed by ENDOR to be an oxo-bridge in the diferric state.[266] This extra glutamate, E97 (numbering according to 1RYT[267]), appears vital to stabilization of the diferrous-dihydroperoxo intermediate.[128,169] Substitution of the E97 to alanine resulted in a complete loss of peroxidase activity, with an increased autooxidation with oxygen.[155] Also, no high-valent ferryl species have been reported for Rbr, and oxidized Rbr appears to show no additional reactivity to oxygen or hydrogen peroxide.[128,154,155] Overall, the mechanism of hydrogen peroxide reactivity with substrate involves oxidation of the diferrous center to a diferric iron center, ensuant with Fe1 toggling to Glu-on and His-off ligation geometry. The diferric center then contains a bridging oxo-species, that, after

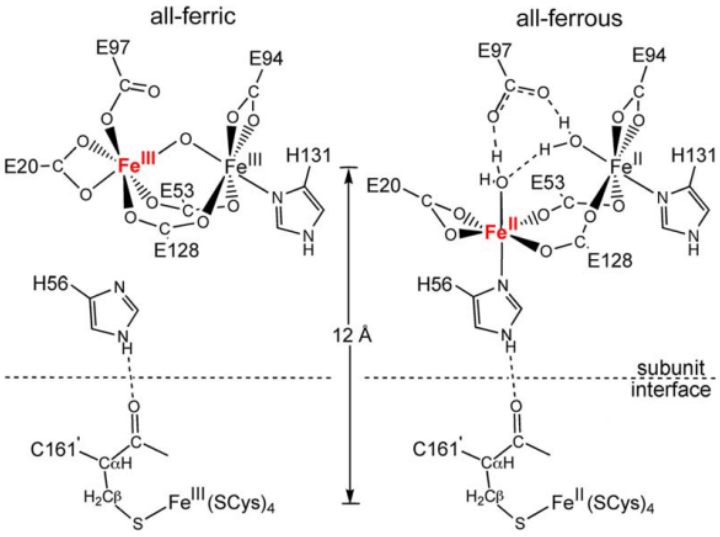

Figure V-1. Depictions of Rbr active site based on diferric and diferrous structures. The redox toggling Fe (Fe1 is depicted in red. Main chain atoms are not depicted for clarity. Reprinted from the Journal of Inorganic Biochemistry, 100, Kurtz, DM, Avoiding high-valent iron intermediates: Superoxide reductase and rubrerythrin, 679-693, Copyright 2006, with permission from Elsevier. http://www.sciencedirect.com/science/journal/01620134

two, one electron transfers from the Rd domain, returns to diferrous and the oxo is protonate to make water.

Recently, we reported a fusion protein from *Clostridium symbiosum* called HydY, which contained a C-terminal four-helix bundle domain, flanked by two Rd-like domains. The CTD of HydY was spectroscopically confirmed to contain an oxo-bridged diferric center, most similar to Rbr-type proteins. However, Mössbauer parameters of the other iron centers were most consistent with the assignment of one classical Rd-like center, and one non-classical. The non-classical Rd center was best fit with mostly O/N ligation, and perhaps one sulfur ligation.

To further understand of the iron centers of CTD, we determined the crystal structure to 1.77 Å. Surprisingly, the structure of CTD revealed the first reported case of bacterial Rbr with three dimensionally domain swapped dimer. Additionally, one of Rd domains was hydrolyzed during crystallization. The structure confirms the diiron center of CTD is most similar to Rbr, and the C-terminal Rd is likely the classical Rd observed by Mössbauer.

Results

Sequence alignment of rubrerythrins

A MUSCLE alignment of all Rbr homologs characterized *in vitro* with *Cs*CTD reveals relatively little conservation amongst Rbr homologs (Figure V-2). At a threshold of 40% sequence identity, only the metal-binding residues appear conserved. Rbr proteins contain two types of iron binding sites: a non-heme, diiron site and a four cysteine rubredoxin-like site. CTD contains two Rd-like $Cx_2Cx_{21-12}Cx_2C$ motifs at both the N- and C-terminus of the Rbr protein, unlike previously characterized Rbr homologs. Previous studies of CTD of *Cs*HydY identified the diiron to be similar to oxo-bridged diiron centers, and functional assays highlighted the CTD to be an efficient peroxidase. The non-heme, diiron site of CTD contains a pair of $Ex_{30-35}Ex_2H$ motifs sandwiching a conserved 7th Glu found within helix 3 of the core four-helix bundle. Classical Rbrs also contain a large linker between helices 2 and 3. CTD also has this 7th Glu in helix 3, but contains a shortened linker between these two helices. The linker between helices 2 and 3 of *Pf*Rbr is also comparatively short, and its crystal structure revealed a domain-swapped dimer.[169,170] Interestingly, *Clostridium acetobutylicum* (*Ca*) encodes for at least

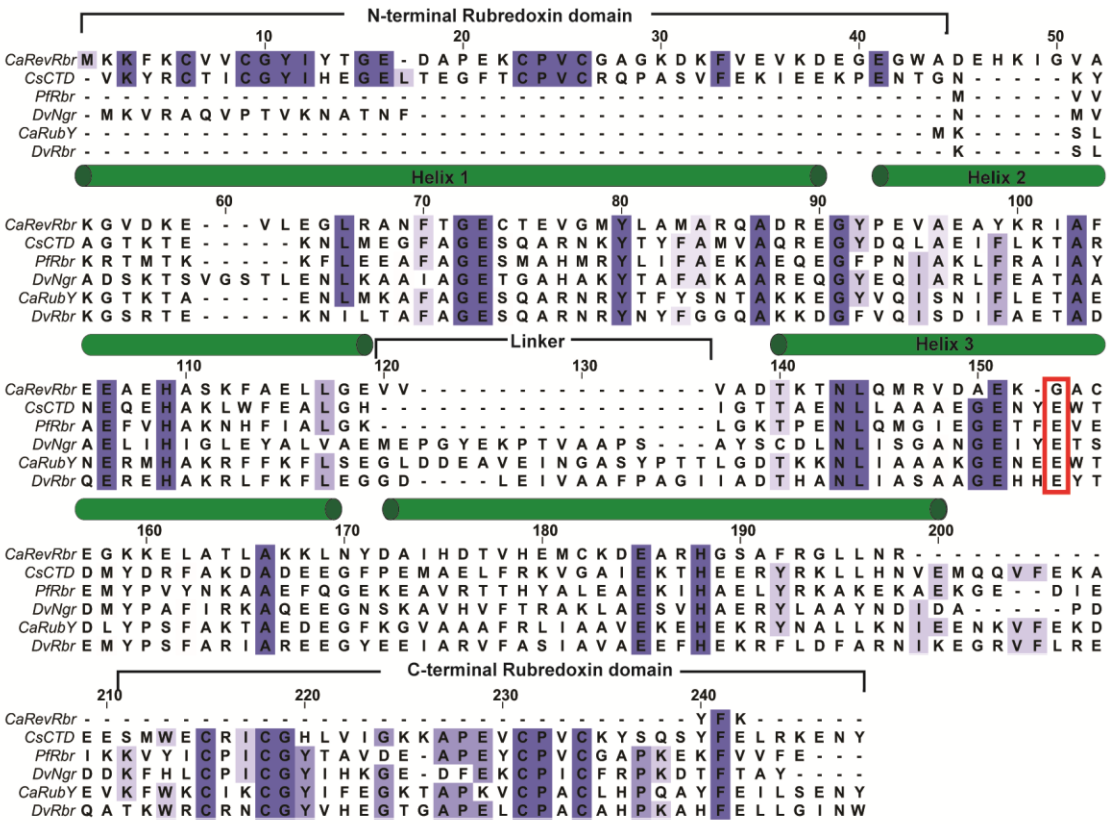

Figure V-2. Sequence alignment of Rbr homologs and *Cs*HydY-CTD. Coloring based on a 40% sequence identity threshold. Red box highlight the 7th Glu characteristic of Rbr proteins.

two Rbrs: a classical one, called RubY, and non-classical RevRbr.[152] RevRbr appears to be missing the extra, 7th Glu in helix 3. This alignment also reveals conservation of a few non-metal binding residues, namely Tyr near the active site, which are thought to be important in H-bonding to active site residues, stabilizing their orientation.[267,268] Based on this the multiple sequence alignment, the shortened linker between helices 2 and 3 will likely influence the fold of CTD, but no clear active site substitutions appear likely candidates to explain the catalytic efficiency observed for HydY.

Table V-1. Data collection and refinement statistics for *Cs*CTD.

	CTD Cu-K_α	CTD SSRL BL7-1
Data collection and processing		
Space group	$P22_12_1$	$P22_12_1$
Cell dimensions	53.99, 63.08, 113.38	54.49, 64.06, 113.31
Wavelength (Å)	1.54180	1.12708
Resolution	2.50	1.77
Total unique reflections	13,192	39,548
Completeness (%)	95.1 (94.1)	100 (100)
Redundancy	6.4 (6.4)	7.7 (7.7)
<I/σI>	9.3 (2.3)	14.2 (3.9)
R_{merge} (%)	15.9 (77.2)	9.1 (44.2)
$CC_{1/2}$ (%)	99.1 (88.2)	99.8 (94.4)
Model refinement		
R-work (%)	17.4	14.02
R-free (%)	24.2	17.20
Fe atoms	6	6
Water molecules	100	363
PEG-400	-	2
RMS (bonds) (Å)	.007	.009
RMS (angles) (°)	0.972	1.13
Ramachandran favored (%)	97.1	98
Ramachandran Outliers (%)	0.0	0.0
Average *B*-factor (Å^2)	32.48	19.96
Protein		18.11
H_2O		31.41
Fe		12.84
PEG-400		40.03

Overall fold

Crystals of CTD were first obtained after 6 months from sparse matrix screens. Optimized crystallization conditions (0.1 mM Bis-Tris pH 6.5, 0.225 M NaCl, 18% PEG-3350 and 3% xylitol) requiring only weeks for crystal growth.. The structure of CTD was determined by molecular replacement using oxidized *Dv*Rbr (PDB entry: 1LKO; sequence identity, 41%) as a search model. The structure was refined to 2.50 Å resolution with a R_{work}/R_{free} of 17.4/24.2 and reasonable geometry (Table V-1). Additional, higher diffracting crystals were identified by increasing the protein concentration (21 mg/ml to 32 mg/mL). Phases were determined for a 1.77 Å CTD data set using the previously refined CTD structure as a search model for molecular replacement, and the structure was refined to a R_{work}/R_{free} 14.0/17.2, again with reasonable geometry.

CTD adopts a four-helix bundle fold characteristic of the Rbr-family, with two metal atoms bound in the center of the helix (Figure V-3). Helix 3 contains a 20° kink near the dimetal center (called π-helix); this distortion is typical of Rbrs and contains the so-called 7^{th} Glu. The crystal structure also revealed a C-terminal fold that contains a mononuclear metal center. This fold is typical of Rd-like domains. The metal ions were assigned as iron based on the bound metal content (3.8 Fe/monomer CTD) and the occupancies were individually refined. The iron atoms bound at the Rd sites occupancies were 100%, while the diiron sites occupancies were 65 and 70% for site 1, and 67 and 75% for diiron site 2.

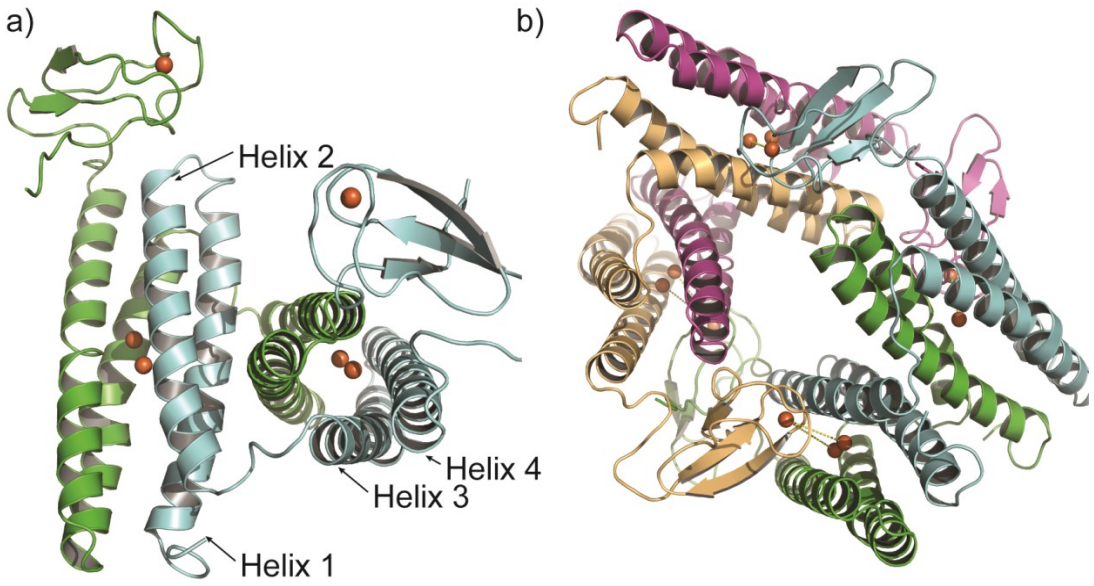

Figure V-3. Overall fold adopted by CTD. a) Represents the domain-swapped dimer found in the asymmetric unit. Each subunit is colored differently for clarity. b) Tetramer of formed from extensive contacts within the crystal.

CTD adopts a domain-swapped dimer in the crystal structure (Figure V-3a). Helices 3 and 4 from subunit one creates a four-helix bundle with helices 1 and 2 from subunit two, and vice versa for the other half of the dimer. This domain-swapping is a ramification of the shortened linker between helices two and 4. The diiron site, then, is ligated across the dimer interface. Residues from both subunits (E145, E179, H182/ E84, E117 and H120) contribute to the active site. This is the first structure of a domain-swapped Rbr from bacteria. Domain swapping has been characterized for two Rbr homologs from thermophilic archaea,[169,170,269] and was speculated to be important for increased thermostability. Domain-swapping occurring in a mesophile such as *Clostridum symbiosum* implies that this architecture is a more general phenomenon than previously suspected.

Unexpectedly, the structure of CTD did not reveal the N-terminal Rd (Rd_A). There is no residual density for any additional domains. Moreover, crystal packing analysis reveals that there is insufficient room for this domain in the unit cell. We suspect that the Rd_A site was hydrolyzed (or proteolytically cleaved) during the crystallization trials. Crystals of CTD first grew over a period of months from a film of red/brown precipitate. Rd sites with irons are ruby red in color, so it is possible that the precipitate within the crystal drop is mostly the hydrolyzed Rd_A domain. Furthermore, SDS-PAGE of crystallized CTD ran at a much smaller molecular weight (22 kD) than solutions of CTD (28 kD). How, and, to a larger extent, why Rd_A was cleaved during crystallization is unclear, though, it must be stressed that CTD is a synthetic construct of a much larger protein. Perhaps the designed construct was destabilized in a manner that destabilized N-terminal Rd domain, making it more susceptible to hydrolysis.

Subunit interactions

Though the asymmetric unit contains dimeric CTD, there are extensive contacts within the crystal that forms tetramer (Figure V-3b). The tetramer is best described as a dimer of dimers, with individual dimers adopting a twisted, head-to-head fold mediated by helices one and two from subunit one and helices three and four from subunit two. In this conformation, the Rd domains are separated by too great an intersite distance (>30 Å) for efficient electron transfer (Figure V-3a). The diiron centers in this conformation are surprisingly close (22 Å). The tetramer interface is best described as a head-to-tail conformation, mediated mostly by Rd domains (Figure V-3b). The shortest intersite iron distance comes from this tetramer, placing the Rd domains close enough (10-12 Å) for

efficient electron transfer pathways. The relevance of this tetramer is in agreement of the calculated molecular weight judged by analytical gel filtration (110 kD). However, the functional relevance of the tetrameric Rd placement is difficult to judge without the presence of the Rd_A domain

Comparison of the Rd_B of CTD suggests conformational mobility of the rubredoxin sites. An overlay of the classical *Dv*Rbr (PDB entry 1RYT) with CTD (C-α r.m.s.d = 1.089 Å) reveals both Rd domains are positioned like caps at the bottom of four-helix bundle (Figure V-4). In 1RYT, a dimer is formed through a head-to-tail type conformation. However, for the domain swapped dimer found in thermophilic archaeal *Pf*Rbr (PDB entry 3MPS), the random coil extending from the four-helix bundle to the Rd domain is extended, allowing for an intersite distance from Rd to diiron site of 11 Å. CTD and *Pf*Rbr structures are quite similar (C-α r.m.s.d = 0.9 Å). This large movement

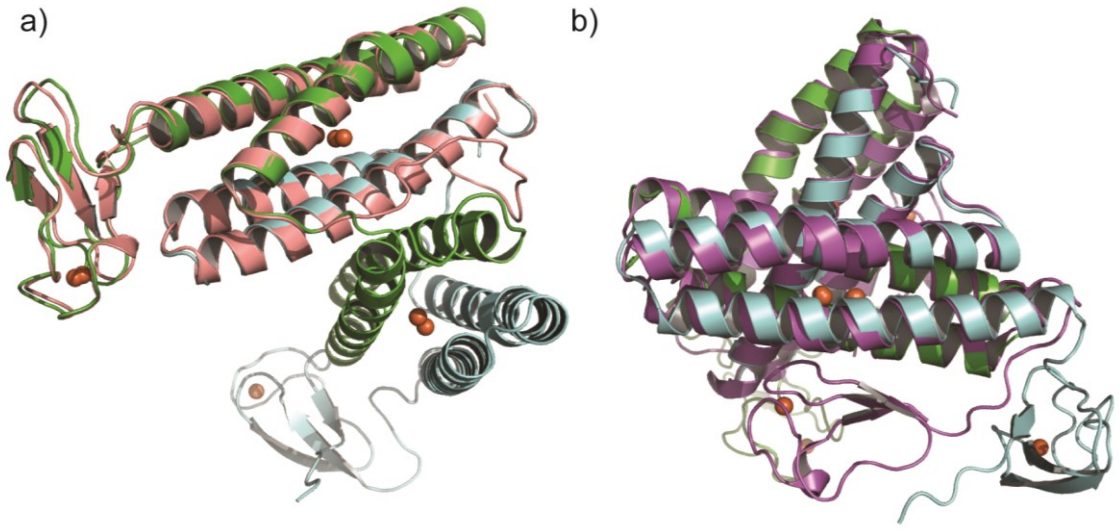

Figure V-4. Overlays of Rd_B domain of CTD (green) with oxidized *Dv*Rbr (a, salmon) and reduced *Pf*Rbr (b, purple).

of domains between various homologs suggests the Rd domains conformation is fluid, and crystallization could trap a particular conformation. However, the Rd domains have not shown redox dependent conformational changes.

The diiron site

The diiron sites of CTD display a significantly different structure than classical Rbrs. As seen from the 2Fo-Fc map, the two iron atoms have slightly distinct coordination geometries (Figure V-5). Fe1 is best described as pseudo-square pyramidal, while Fe2 is approximately octahedral. The diiron site is comprised of residues spanning the dimer interface. Fe1 is coordinated by a terminal, bidendate E145, bridged by E179

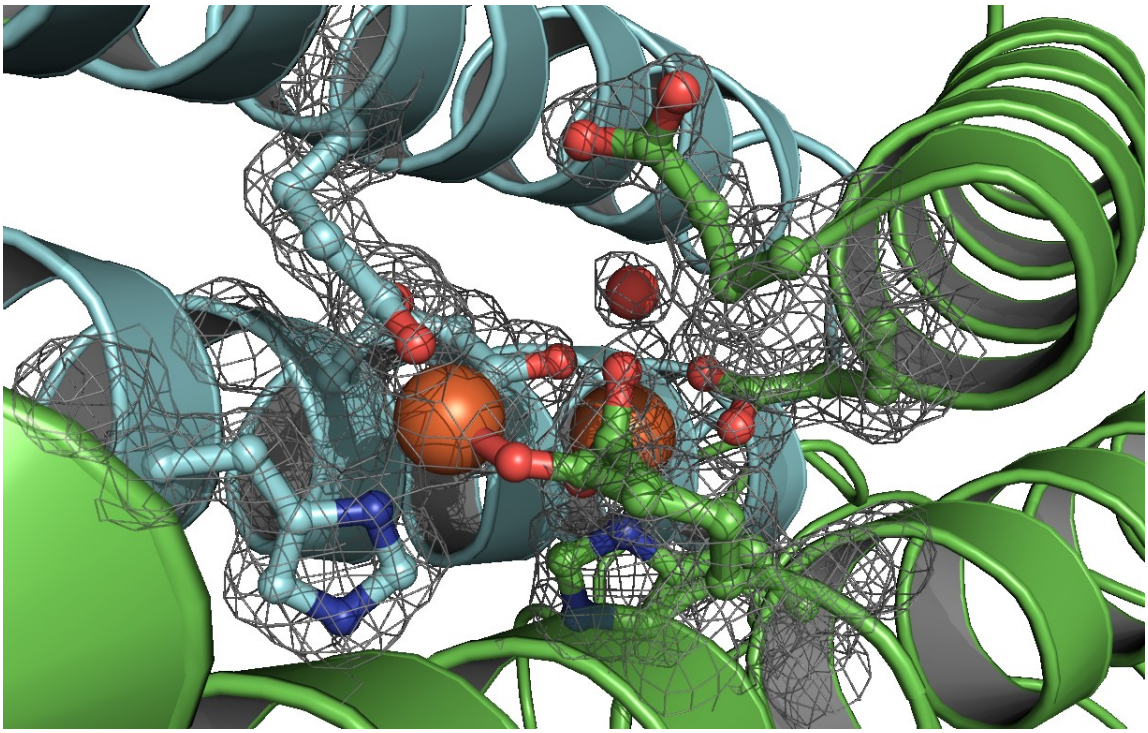

Figure V-5. $2F_o - F_c$ map reveals the active site of CTD. Clearly from this structure, the 7^{th} Glu (E148) is rotated away from the active site, not coordinating either iron atom. Fe1 is represented as the leftmost iron.

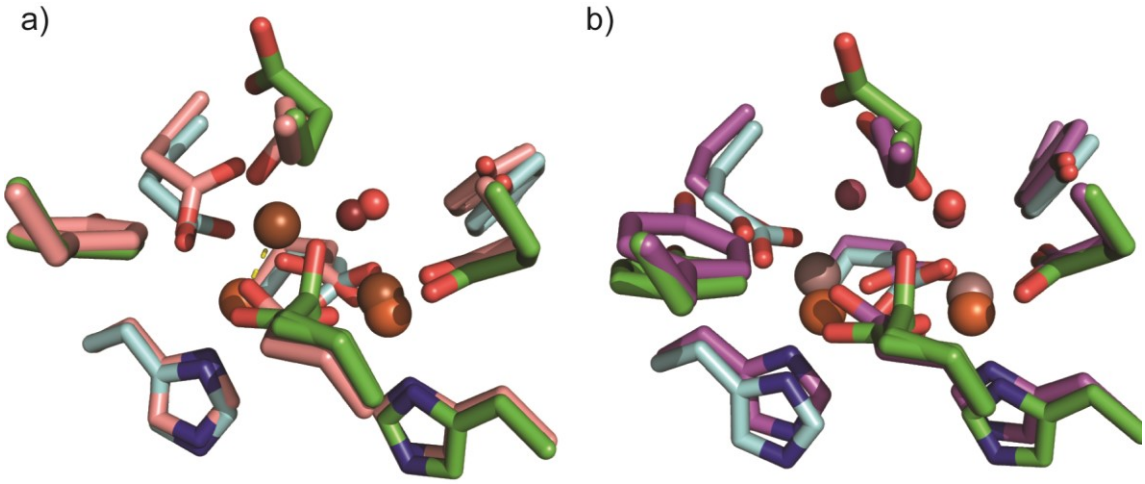

Figure V-6. Overlay of the CTD diiron site (green, cyan) with oxidized *Dv*Rbr (a, salmon) and reduced *Pf*Rbr (b, purple). Main chain atoms are omitted for clarity. Iron and water atoms are discolored slightly to specify which structure to which they belong

and an axial H182 from subunit 1. Fe1 also shares a bridging E117. Along with E117, Fe2 is ligated by a terminal, bidentate E84, an axial H120, and a water. Unexpectedly, E148, the 7th Glu, is rotated away from the active site, interacting with solvent. There is no residual density to place this mechanistically important glutamate residue near either iron within the active site. The terminal, bidendate Glu residues are hydrogen-bonded to conserved Tyr residues (Y153 from subunit 1 and Y91 from subunit 2). These tyrosine residues are speculated to be important for positioning the active site. The iron centers do not appear to be fully occupied as the sites refined to occupancies of 65% and 70%, respectively. Lastly, the bridging E179 was modeled in two different conformations: a bridging and monodentate to Fe2. The relative occupancies of E179 were not individual refined, however. Both diiron active sites appear quite similar in the crystal structure.

Since CTD was oxidized with slightly excess H_2O_2 before being brought out of an anaerobic atmosphere and crystalized in air, CTD was expected to be in an oxidized

state. No electron density is present between the diiron centers and the distance between Fe1 and Fe2 is 3.8 Å, which are inconsistent with the presence of bridging oxo species.[267] This is surprising as the ^{57}Fe-reconstituted CTD_{ox} had Mössbauer parameters consistent with an assignment of a bridging-oxo species.

To further understand this discrepancy between the CTD diiron site, this active site was overlaid with Rbr in both oxidized and reduced diiron states. First, a comparison of CTD with oxidized *Dv*Rbr (Figure V-6a). The diiron site of CTD (Figure V-6a, green and cyan) is in great agreement of backbone Cα of oxidized *Dv*Rbr (Figure V-6a, salmon) with an RMSD of 0.615 Å. However, the geometries of irons are completely different. In the oxidized *Dv*Rbr structure, Fe1 is ligated by the 7th Glu (Glu-on) and the histidine is not coordinating a metal (His-off). Additionally, water is modeled as bridging the irons. The Fe1-----Fe2 distance is ~3.2 Å and is consistent with a diiron center bridged by an oxo species.[267] In comparison, the Fe1 of CTD has moved 2.2 Å to adopt a His-on/Glu-off conformation, and as a result, the diiron distance is 3.8 Å. To compensate for this movement, a terminal Glu rotates ~70°, with both oxygen atoms in equatorial geometry positions. Furthermore, the bridging glutamate ligands are in different conformations as well, with the 7th ligating Fe1 in the *Dv*Rbr structure, whereas the corresponding Glu in the CTD structure adopts a conformation away from the active site. There are no appreciable differences at Fe2.

In comparison, an overlay of reduced *Pf*Rbr and CTD are in great agreement (Figure V-6b). Both iron sites have an Fe1----Fe2 distance of ~3.8 Å and the absence of a bridging oxo species.[128] While the sites are similar, Fe1----F1 distance are moved by

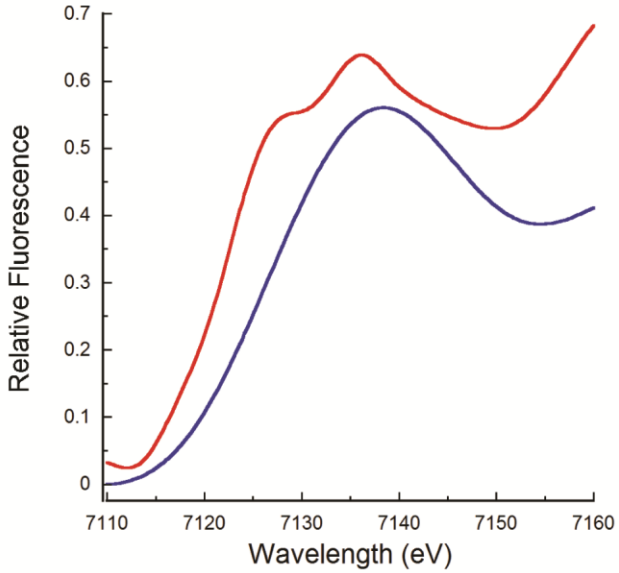

Figure V-7. X-ray fluorescence data of a CTD crystal before (blue) and after (red) data collection at SSRL beamline 7-1 reveals x-ray photoreduction.

~0.3 Å. This Fe1 movement is likely dictated by a slight movement of the iron ligating residues. The 7th Glu of *Pf*Rbr, despite reduction, is still rotated toward the iron centers, interacting with two solvent molecules. These similarities of the CTD active with reduced Rbr imply that CTD was reduced from the synchrotron radiation. Indeed, X-ray absorbance on another CTD crystal displays a shift in the Fe-edge from 7138 eV before data collection, to 7136 eV with pre-edge features at 7128 eV (Figure V-7). This X-ray absorption data gives further credence that CTD was phootoreduced. No absorbance data was collected during data collection, however.

Solvent canyon

All diiron sites of Rbr are highly solvent accessible, and the diiron site of CTD is no different. Two water molecules were modeled near the diiron active site. A channel,

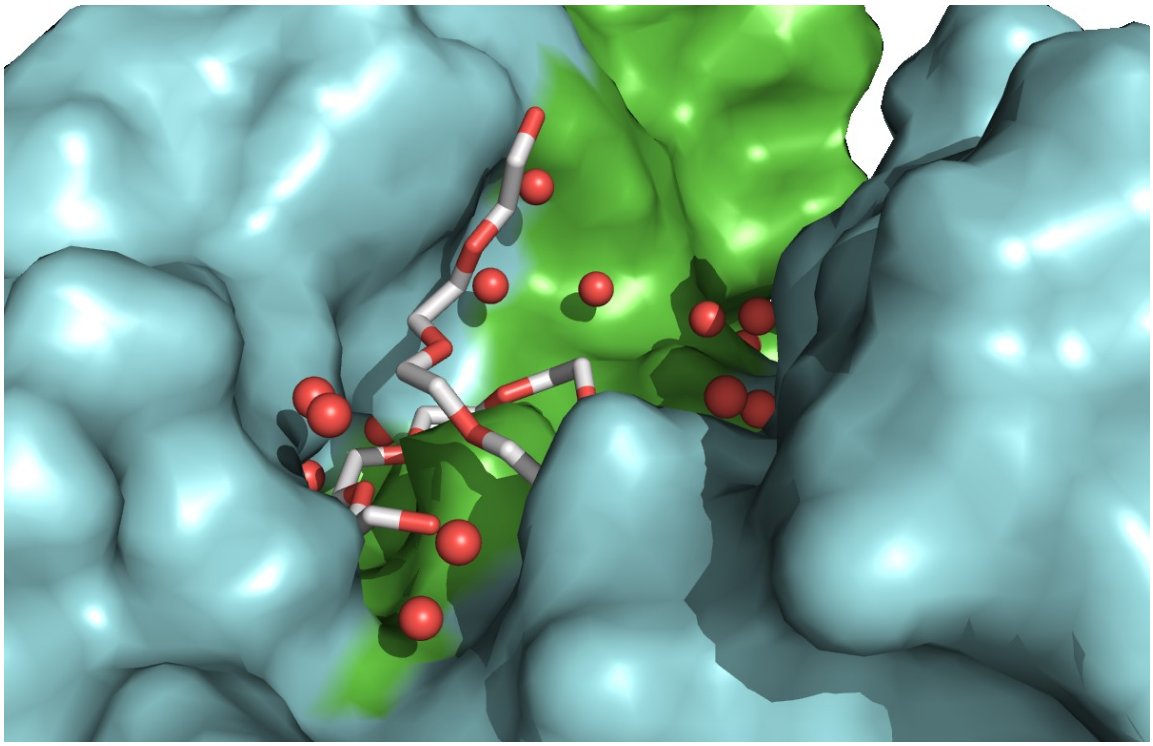

Figure V-8. Surface representation of the CTD dimer reveals a solvent canyon near the diiron active site. Multiple coordinated waters are found here, along with a PEG-400. The blue and green surfaces represent subunit 1 and 2, respectively.

only 7 Å long, leads directly from these waters at the active site to the surface. Immediately outside is a solvent canyon, filled with many ordered waters (Figure V-8). Additionally, PEG-400 molecules were modeled near both active site that interact with surface exposed lysine residues. A 30 second soak of mother liquor plus 20% PEG-400 was used as a cryogenic protectant. This indicates the solvent canyon exchanges readily, and may aid in explaining the high catalytic efficiency observed for CTD.

Discussion

HydY was found to consist of two domains: an N-terminal [FeFe]-H_2ase and a C-terminal rubrerythrin. The CTD of HydY appears to be comprised of two Rd-like sites

flanking a diiron site, most similar to Rbrs. This CTD construct was found to have the highest catalytic efficiency ($1.7x10^7$ M^{-1} s^{-1}) and a k_{cat} at least as fast (1870 min^{-1}) as those reported for *Dv*Rbr (estimated to be 2000 min^{-1}). As an attempt to understand the molecular details of this increased reactivity with H_2O_2, a structure of CTD was refined at 1.77 Å resolution to a R_{work}/R_{free} 14.0/17.2. Unlike classical Rbr proteins, CTD adopts a domain-swapped dimer and is the first Rbr from a bacterial species that uses this fold. This domain swapping is a consequence of a shortened linker between helices 2 and 3. Domain swapping in Rbr may be more pronounced than previously suspected,[169] especially since *Ca*RevRbr contains the same shortened linker. The implications for domain swapping remain unclear, though Dillard and coworkers[169] suggested this fold might have increased Rbr to tolerance to stresses, such as increased thermostability. The thermostability of the CTD construct has not yet been determined. Certainly, this explanation fits the original finding of domain-swapped Rbr homologs in thermophilic archaeal species.[169,269] *Ca*RevRbr was found to be induced by both O_2 and increased temperature, causing some to speculate it was a general heat-shock protein.[124,162,270] Perhaps the domain swapping observed in CTD, and speculated in *Ca*RevRbr (Figure 1), allows these proteins to function during various cellular stresses, including ROS stress.[152] The observed three dimensional domain swapping observed for the CTD may also explain why full-length HydY is difficult to prepare in significant quantities. Surely, expressing an 80 kD protein in *E. coli* is arduous, but also requiring two 80 kD proteins to domain-swap for a stable fold is even more demanding.

We were initially intrigued by the di-Rd domains of CTD and suspected the additional Rd_A domain was one determinant for the high catalytic efficiency of CTD. No di-Rd Rbr has been structurally characterized to-date, and unfortunately this study was unable to provide that information. It appears the Rd_A domain was hydrolyzed *in situ* before crystallization. It is tempting to speculate that Rd_A would occupy the opposite side of the four-helix bundle, allowing for electron transfer to the diiron site from either face. This is given credence by the position of the Rd domain in the tetramer and the position of the remaining N-terminal peptide. However, the role of Rd_A remains unclear. Additional studies where other CTD constructs are generated, such as the one observed in the crystal structure, Rd_A and the diiron domain or simply the diiron domain only, and characterized biochemically and biophysically would greatly enhance the understanding of the roles of Rd domains.

Comparison of the diiron site of CTD with other Rbr indicates photoreduction at the iron sites. Crystals of CTD were prepared in the oxidized state, and Mossbauer parameters collected previously were consistent with the assignment of μ-oxo bridge species in the diferric state. The structure of CTD determined to 1.77 Å resolution, however, clearly indicates no μ-oxo species (Figure #). Instead, a single water molecule was modeled as ligating Fe2, with an open coordination site on Fe1. Additionally, Fe1 is ligated by His182, instead of the expect His off/7th Glu on identified in many oxidized Rbr homologs.[168-170,173,179,180,267,269,271] The location and ligation of Fe1 intimates all the irons of the active site are reduced. Indeed, this suspicion of X-ray photoreduction (XPR) from synchrotron radiation was confirmed on an additional CTD crystal (Figure

#). XPR has been documented for *Dv*Rbr[179] and appears to be a general issue with X-ray structures of metalloproteins.[272-274] Reduction of the iron centers during the course of data collection at 100 K explains the His182-on ligation as well as the lack of an oxo-bridging species. Additionally, Rbr active sites are quite plastic in regard to redox state, thus the structure of CTD likely represents some average of oxidize, partially-reduced and fully-reduced diiron active sites. The heterogeneity of the active site is reflected in the modeled dual-conformations of ligating residues and compounds our interpretation of the CTD active site.

Despite the observed XPR, the position of E148, the 7th Glu, in CTD is intriguing. E148 is rotated to interact with solvent, instead of ligation to or near the diiron center.[169,180] The 7th Glu is mechanistically important, where it is positioned for interactions with the diferrous-dihydroperoxo intermediate.[128,155] The 7th Glu has been speculated to be important for imparting substrate specificity, essentially screening against O_2 binding to the diiron site.[128] Why Glu148 adopts this rotation away from the active site remains unclear because no specific interactions with other protein residues are readily discernable. Mutation of the 'extra' Glu in *Dv*Rbr to phenylalanine or alanine resulted in a complete abatement peroxidase activity, and a slow (minute time scale) oxidation of the diferrous center with H_2O_2.[155] A structure of *Dv*RbrE97A indicated the loss of the extra ligating Glu resulted in rotation of the bridging glutamate residues to bidentate and terminal.[275] It should be noted that the coordinates to this structure were never deposited into the RCSB. Also, *Dv*RbrE97A protein preparations bound sub-stoichiometric amounts of iron. Interestingly, *Ca*RevRbr contains a Glu to Gly

substitution at the 7th Glu (Figure V-1). *Ca*RevRbr shows increased reactivity to O_2 in comparison to typical Rbr homologs. A follow-up study where CTD was re-engineered in a manner similar to *Ca*RevRbr would be warranted to determine if those substitutions increased O_2 reduction chemistry.

CHAPTER VI

INVESTIGATION OF THE DIVERSITY OF HYDROGENASES THROUGH PROTEIN SIMILARITY NETWORKS

Introduction

Hydrogenases (H_2ases) reversibly catalyze the reduction of protons to dihydrogen,[7] and are essential to metabolism in a variety of microbial communities.[5,9-11,276,277] The [FeFe]-H_2ase, which employs a unique organometallic diiron cofactor called the H-cluster, is considered the superior H_2ases catalyst[38] due to its high rates of catalytic H_2 production (turnovers > 1000 s^{-1})[219,220] and H_2 consumption (turnovers estimated > 10000 s^{-1}),[40] and this fact was lead to usage in biological fuel cells applications.[219,278-280] High rates of catalysis by [FeFe]-H_2ases depends on influence of the protein framework[223] to modulate active site geometry[239,281,282] and tune chemical properties of the cofactor.[224,283-286] Therefore, understanding the mechanistic implications of the protein framework is paramount to evolving increased H_2 production rates and possible designing more efficient H_2 producing catalysts.

Examination of X-ray crystal structures of the simplest [FeFe]-H_2ase *Chlamydomonas reinhardtii* (*Cr*HydA) or *Clostridium pastueranium* hydrogenase I (*Cp*I, PDB:3C8Y), the largest [FeFe]-H_2ase crystalized to-date, reveal the H-cluster is buried within the protein environment, where the protein provides second-shell interactions with the cofactor. Alignments of the sequences of crystalized proteins and other [FeFe]-H_2ase homologs reveal the conserved binding sites for the H-cluster: P1, TSCCPxW; P2, MPCx_2KKxE; P3, M(A)Cx2xGCx_2GGGQ.[2,3,6] Four cysteine residues

provide ligands to the cubane [4Fe-4S] cluster, and the first cysteine is positioned to act as a general base during catalysis.[7,223,233] Other residues, such as the Met in P2 and the first Lys in P2, provide non-covalent interactions to CO and CN^- ligands, respectively.[223,238] Mutagenesis studies targeting either of these residues led to decreased H-cluster incorporation, and possible affected catalysis.[223] These residues appear to be strictly conserved in all [FeFe]-H_2ases studied to-date.

Recently, a novel [FeFe]-H_2ase-rubrerythrin protein from *Clostridium symbiosum* (*Cs*HydY) was found to display near uni-directional H_2-uptake catalysis and was remarkably tolerant to anaerobic, oxidative inactivation. *Cs*HydY, in this sense, appeared to have catalytic properties reminiscent of O_2-tolerant [NiFe]-H_2ases. We speculated that the protein matrix of *Cs*HydY interacted with the bound H-cluster in a non-traditional fashion. We speculated that conserved substitutions in P2 (Met to Thr) and in another H-cluster binding motif called P4 (typically, APAxVR; first Ala to Ser in *Cs*HydY) resulted in the displayed catalytic bias (see Chapter III).

In this manuscript, the conservation of this unique H_2-uptake biased [FeFe]-H_2ase was surveyed using bioinformatics. Generation of a sequence similarity network of nearly 4000 [FeFe]-H_2ase sequences found a large functional diversity in domain architectures, hinting a possible diversity in chemistry of these sequence homologs. H_2-uptake biased [FeFe]-H_2ase, *i.e. Cs*HydY-like, sequences clustered into a sub-group. Analysis of the second-shell interactions from the protein framework suggested that the *Cs*HydY-like H-cluster interactions may be conserved in most members of this sub-

group. Identified sequences with PAS-like domains fused to [FeFe]-H_2ases also revealed distinct, non-classical H-cluster binding motifs.

Results

Sequence similarity network of [FeFe]-H_2ases

A BLAST search using the sequence of the uni-directional [FeFe]-H_2ase from *Clostridium symbiosum* (*Cs*HydY, GI:769118840) was submitted, and nearly 8000 sequence homologs were identified. An all-by-all BLAST was then performed to create

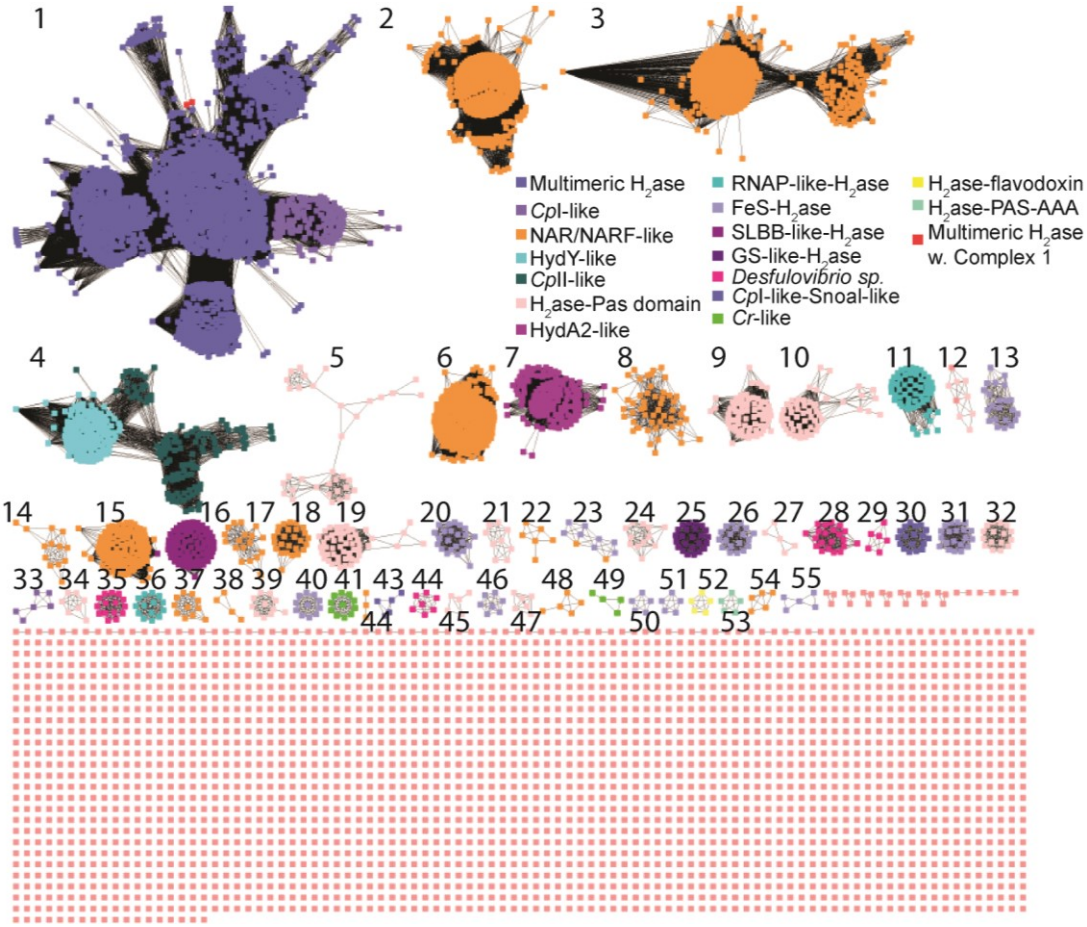

Figure VI-1. Sequence similarity network of [FeFe]-H_2ase sequences using a stringency expect value of E^{-150}.

a sequence similarity network (SSN) at a strict E-value cutoff of 10^{-150}. With this stringency for sequence homology, a total of 55 subgroups could be identified as depicted in Figure VI-I, totaling nearly 4000 sequences. [FeFe]-H_2ase homologs are distributed across bacterial classes (Clostridia, Thermotogae and δ-Proteobacteria), anaerobic protists, green algae and even higher eukaryotes.

Identified H_2ase homologs display a wide-range of modularity for catalysis, as previously described.[3,6,14] The most abundantly identified homologs grouped within

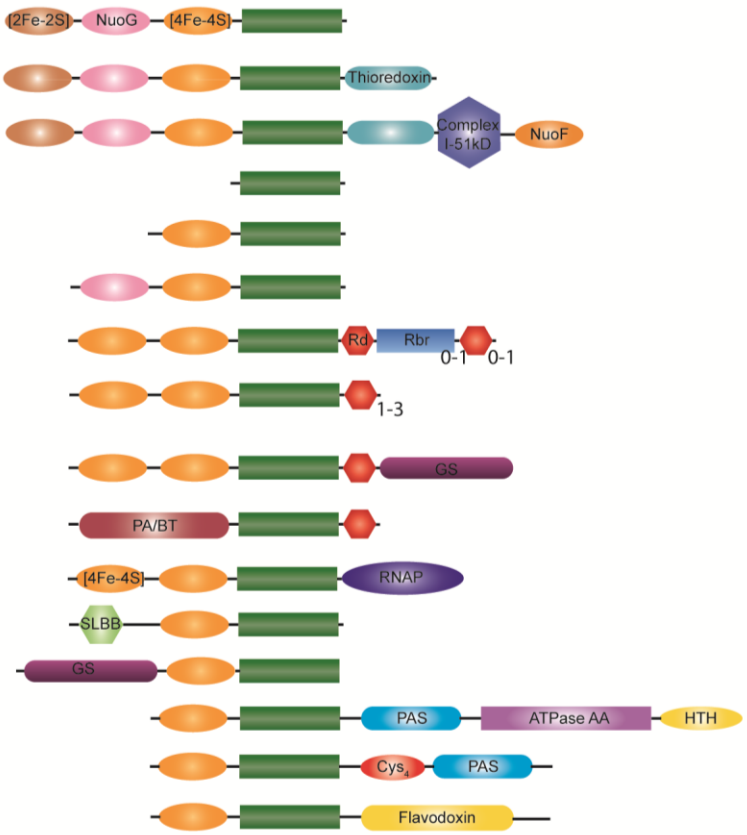

Figure VI-2. Domain architectures of [FeFe]-H_2ase sequences identified from the sequence similarity network. The green box indicates an H-cluster binding domain.

cluster 1, encompassing over half (~1800 sequences) of homologs that grouped within the SSN. The overwhelming majority of these homologs appear to be multimeric H_2ases, confirming a speculation that bifurcating H_2ases are the most representative H_2ase in bacteria (Figure IV-2).[287] The N-terminal ferredoxin-domain (F-domain) appears quite variable, where [2Fe-2S], NuoG-like [4Fe-4S] and typical [4Fe-4S] clusters binding domains are exchangeable. Other predicted domains range from H_2ases with thioredoxin and Complex I-like domains (found in anaerobic protists), glutamate synthase binding domains, rubredoxin/rubrerythrin domains and flavodoxin-like domains. The thioredoxin/Complex I-like domains are hypothesized to take part in metabolism in hydrogenosomes by regenerating NAD^+, suggesting these microbes share a common ancestry with mitochondria.[288] Rubrerythrins are diiron proteins involved in H_2O_2 reduction during ROS stress, and the Rd domain efficiently transfers electrons into the diiron site using external reducing equivalents.[128] *Cs*HydY, which contains these domains, was recently characterized *in vitro* and displayed near uni-directional H_2 uptake catalysis, contrasting with classical H_2ases. It was speculated that HydY catalyzes a H_2-dependent peroxidase reaction. Glutamate synthases (GS) are proteins that use NADH or reduced ferredoxins with co-substrates glutamine and α-ketogluturate to produce two glutamates.[77] Two GS/[FeFe]-H_2ase homologs were identified, one within the HydY cluster (Figure IV-1), which also appears to contain rubredoxin-like (Rd) domain linking the H_2ase to the and another sub-group with no Rd. Based on the need for external reducing equivalents, this fusion protein likely functions similarly to *Cs*HydY, consuming H_2 to produce glutamate. These GS-H_2ase fusions could even

operate in the opposite direction, *i.e*. H_2 production from glutamate, depending on cellular resources. Flavodoxins are electron transfer proteins that bind flavin mononucleotides. Why these H_2ases homologs contain a C-terminal flavodoxin domain is unclear (Figure IV-2).

Additionally, [FeFe]-H_2ase homologs with soluble ligand binding domains (SLBB) and archaeal RNA polymerase domains were identified, that group separately (Figures IV-1 and 2). SLBB domains can be secreted or periplasmic, where they bind some ligand, in some cases even cobalamin, and this ligand is moved into the cell in a ABC-type transporter-dependent fashion.[289] The inclusion of RNAP-like domain with an [FeFe]-H_2ase is perplexing, but further supports the notion of that nature repurposes tools for increased fitness.

[FeFe]-H_2ase homologs also emphasize an evolutionary repurposing of the H-cluster domain. Numerous identified homologs contain PAS-like domains and, in eukaryotes, [FeFe]-H_2ase like domains called nuclear architecture related (NAR) and nuclear prelamin A recognition factor (NARF). PAS domains function as signal sensors, binding some substrate transducing it as a signal for some cellular response. In archaea and bacteria, these domains appear to function in sensing oxygen and redox environments.[290,291] Given the idea of syntrophy for H_2 in microbial environments, this [FeFe]-H_2ase-PAS protein could sense H_2 to turn on H_2-consuming metabolic pathways. Or, alternatively, it could sense ROS stress by binding O_2/H_2O_2 or sense oxidative conditions. It is unclear if this fusion would bind an H-cluster, although non-classical H-cluster motifs were speculated for *Ruminococcus albus*.[70] NAR-like homologs are

thought to be involved in cytosolic Fe-S cluster biosynthesis,[81] and homologs were identified in all higher eukaryotes. NAR/NARF proteins are still poorly understood, and the cluster content of these [FeFe]-H_2ase homologs remains a mystery.

Despite the clear domain modularity of [FeFe]-H_2ase homologs, additional domains do not dictate the sub-grouping of these homologs (Figure VI-1). For instance, both the *Desulfovibrio* sp. and green algae [FeFe]-H_2ases clustered into subgroups, as did the *Cs*HydY homologs. This observation suggests that there are additional determinants for the groupings of H2ases.

Analysis of sub-group 4

To further understand the reasons for this diversity in [FeFe]-H_2ase homologs, sub-group 4 was analyzed in further detail by examining conserved cofactor binding motifs. Cluster 4 was selected because it contains *Cp*II and HydY homologs, which were recently shown to be uni-directional H_2 uptake [FeFe]-H_2ases. This sub-group contains 234 sequences, which should avoid over-interpretation due to the relative size. Second-shell contributions near the H-cluster were speculated to be the determinants for this change in catalysis. Previous studies have attempted similar forays into understanding protein-specific tuning, but only utilized a small sample size, through the lens of characterized [FeFe]-H_2ases *Cp*I and *Cr*HydA1, to understand the influence of the protein matrix.

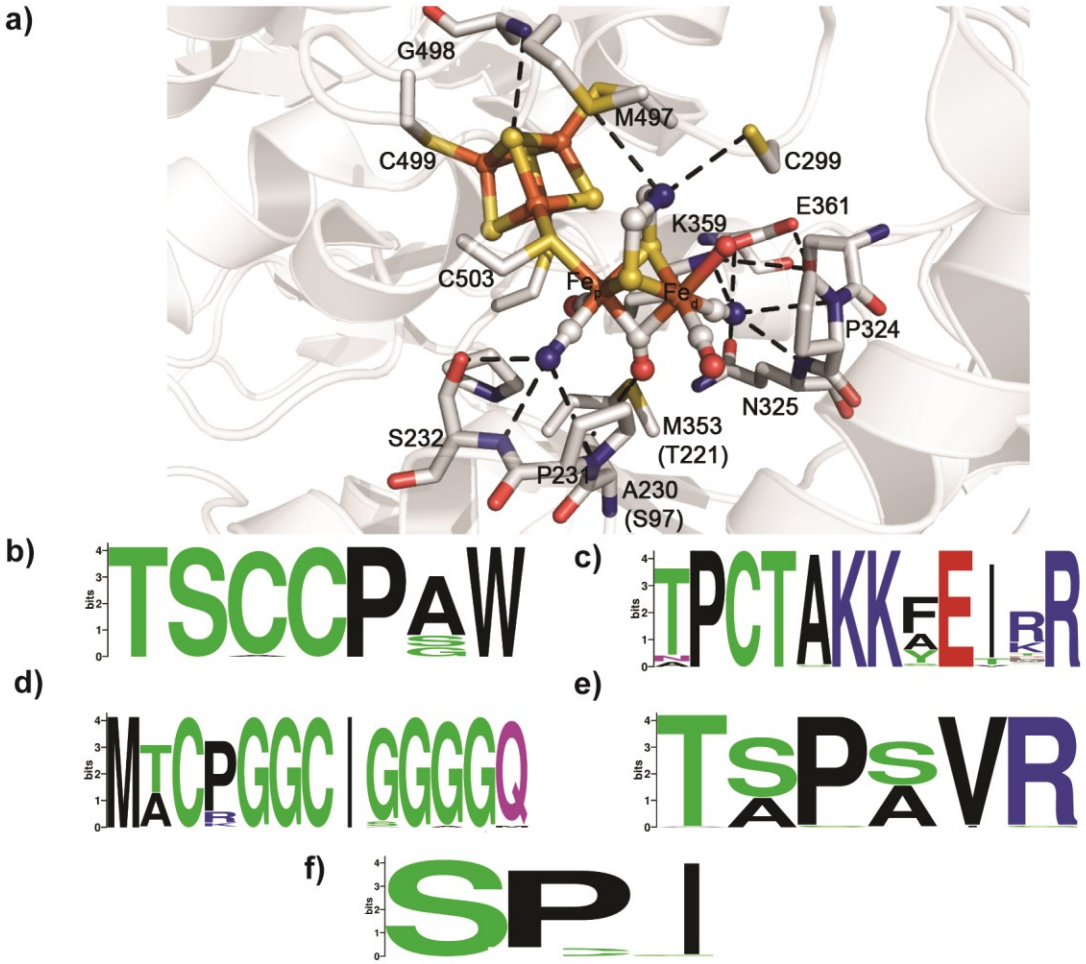

Figure VI-3. Conserved H-cluster binding motifs P1-P4 that provide non-covalent interactions to the cofactor (a). Conserved motifs identified in sub-group 4 of the sequence similarity network of P1 (b), P2 (c), P3 (d), P4 (e) and SPQ (f). Weblogos are colored according to chemical identity. A bit score of 4 indicates a completely conserved residue.

The active site of the [FeFe]-H_2ase is found buried within the protein, formed between several loops and helices. Residues that non-covalently interact with the H-cluster exhibit a high degree of conservation, with these residues specified in a number of studies and reviews (Figure VI-3).[3,6,58,223,233,292] These bioinformatics studies identified three motifs that coordinate the H-cluster: P1, TSCCPxW; P2, MPCx_2KKxE; P3, M(A)Cx2xGCx_2GGGQ. Additional motifs coordinate the H-cluster near the

diatomic ligands, with 'P4' (APAxR) interacting with the bridging CO and proximal CN^- and a SPQ motif interacting with the distal CN^- and H-bonding with other conserved residues.

A MUSCLE alignment of the 234 sub-group 4 homologs agree with this proposed active site conservation; however, there are a few key differences. Within the P2 motif, the conserved M353 (all numbering according to PDB: 3C8Y) is substituted, with 87% Thr, 6% Asn and 5% Ala. Substitutions of this Met residue appears to be specific only to this sub-cluster. Substitution of hydrophilic residues, or small hydrophobic residues, would likely largely affect catalysis, as hypothesized previously (see Chapters III and V). The P3 motif provides Met and Cys residues that interact with the azadithiolate and the cubane cluster, between these residues, Ala is substituted to Thr 57% in sub-group 4. The so-called P4 motif (described previously, Chapter III), occurs before the P1 motif in sequence but described after introduction of P1-P3 motif nomenclature, contains three interactions to the H-cluster. The first Ala creates a hydrophobic pocket for the bridging-CO, and this residue is substituted to Ser 66% of the identified homologs. This Ser was suggested to a determinant for catalytic bias of *Cs*HydY, but the lack of conservation (as was seen in P2) argues otherwise. However, all HydY homologs, annotated based on containing at least a C-terminal Rd, contain this Ser substitution. Other homologs within this group that contain the Ala are all from the class Negativicutes, and these homologs lack Rd domains. Thus, it appears the Ser substitution also is concomitant with a Rd domain. Perhaps the Ser near the H-cluster is important not for catalytic bias, but instead minimizes anaerobic, oxidative inactivation

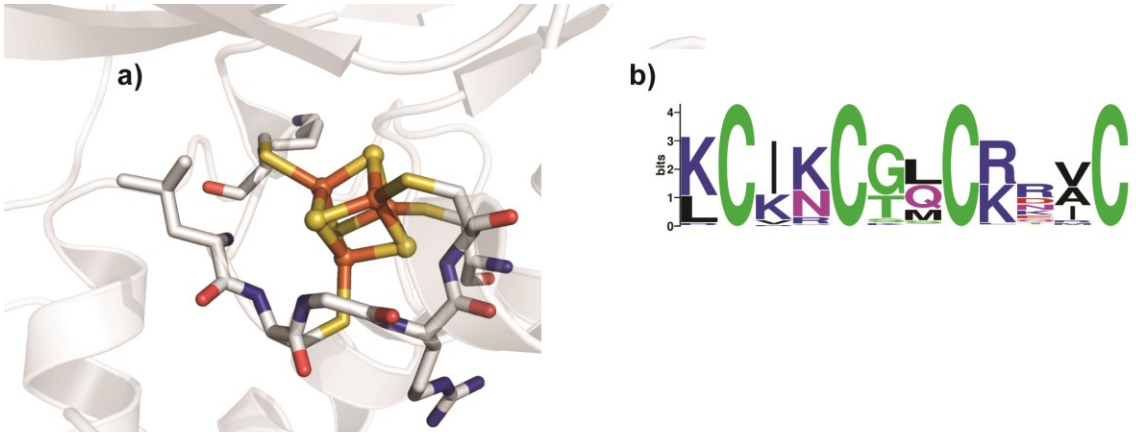

Figure VI-4. Depiction of the [4Fe-4S] cluster from *Cp*I (PDB: 3C8Y; a) and the corresponding positive patch sequence logo from sub-group 4 from the sequence similarity network. Colors of the one letter codes indicate chemical identity, and conserved residues have bit scores of 4.

as monitored by protein film electrochemistry. Furthermore, an additional SPQ motif, which provides interactions with the proximal CN^- through electrostatics of the Pro and main-chain Gln, has a substitution of an isoleucine (97% occurrence) at the Gln residue and Cys (10% occurrence) at the Pro. The Ile likely does not preclude interactions with the CN^-, but the hydrophobic side chain would be inserted into a hydrophilic pocket. This isoleucine substitution would result in the movement of the coil housing the SPQ motif, or hydrophilic residues would require conformational changes. Either scenario would result in a modified H-cluster binding pocket that might affect catalysis.

While the above mentioned active site substitutions might affect catalysis, these substitutions do not explain the overpotential requirement observed in electrochemistry studies. The overpotential was hypothesized to be a result of 'positive-patch' substitutions within the F-domain (Chapter III). As depicted in Figure VI-4, multiple positively charged residues occupy positions near a [4Fe-4S] cluster. Lysine, arginine

and asparagine residues flank all of the conserved Cys residues that are annotated to bind a [4Fe-4S] cluster. These positive charges near the [4Fe-4S] cluster would likely attenuate the potential of the cluster to significantly more positive potentials. Indeed, the redox potential of clusters within *Cp*II were found to be increased to nearly -180 mV, hundreds of mV more positive than typical [4Fe-4S] clusters.[235] Thus, analysis sub-cluster 4 of this SSN suggests the defining motifs of these hydrogenases are likely to H-bonding substitutions within H-cluster binding motifs and positively charged residue substitutions within a [4Fe-4S] cluster, which likely dictates catalytic properties, as suggested previously (see Chapter III).

Analysis of PAS domain proteins

We next analyzed all PAS domains fused to [FeFe]-H_2ases. We hypothesized

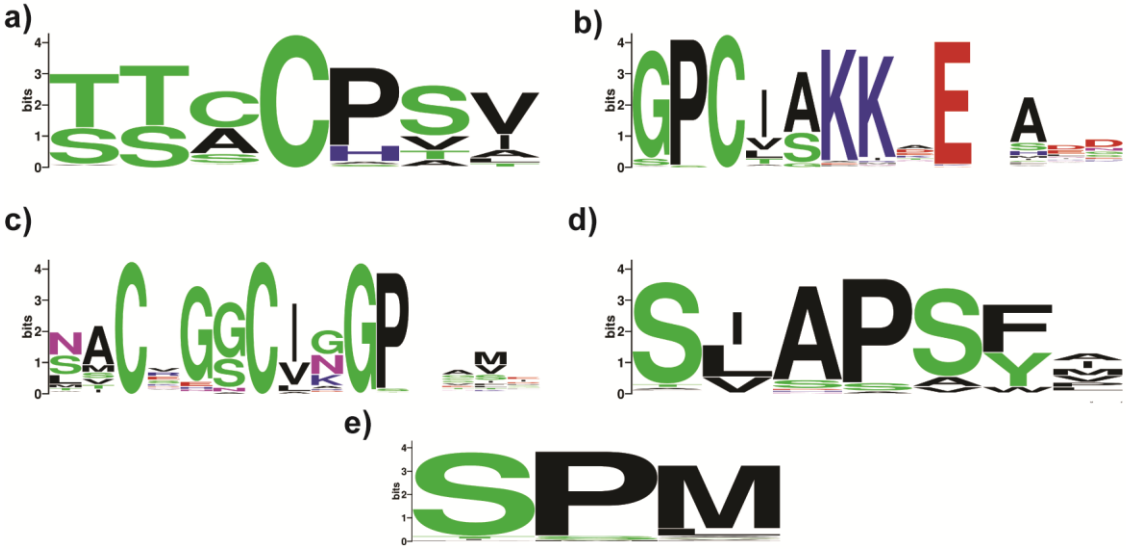

Figure VI-5. Sequence logos proposed H-cluster binding motifs of PAS domain fusions identified. Conservations of substituted residues in P1 (a), P2 (b), P3 (c), P4 (d) and SPQ (e) imply that PAS domains would bind an H-cluster in an usual manner, if at all.

that since PAS domains bind soluble substrates or respond to cellular redox conditions, these homologs would bind the H-cluster in a non-canonical manner in order to facilitate signal transduction.[70] A total of 282 [FeFe]-H_2ase-PAS domain fusions were analyzed. All motifs appear to have significant variability within the H-cluster binding motifs (Figure VI-5). The cysteine residues required to bind the cubane [4Fe-4S] cluster appear to be the only conserved residues, while residues important for coordinating proximal and distal CN^- ligands (K in P2, 94% occurrence and P in P4, 97.5% occurrence) is nearly absolutely conserved. The first cysteine in P1, identified as the general base during the catalytic cycle, only occurs 48.2% in the PAS domain homologs, with Ala (33%) the next most encountered residue, likely indicating PAS domains would lack the ability to catalyze H^+ reduction or H_2 oxidation. Methionine residues in P2 and P3 that stack below and above the H-cluster (Figure VI-5) are also lacking. The P2 Met residue is substituted with Gly (91.8% occurrence), while the P3 Met residues is equally substituted with N/S/L residues.

Discussion

The rapidly increasing NCBI non-redundant database has led to the discovery and annotation of a myriad of hydrogenases, many of them orphans, lacking any information other than sequence identity and similarity of various domains. We have attempted begin the monumental task of assigning functions for these enzymes. Nature has clearly evolved numerous repurposed functions for this old enzyme, and, in a sense, taught 'old dogs new tricks.' [FeFe]-H_2ases, as has been described by numerous others, are highly modular in nature, and this theme appears to underscore the chemical

diversity [FeFe]-H_2ases are capable of undertaking. The newest members of this pack are the uni-directional H_2-uptake [FeFe]-H_2ases. Using SSNs for [FeFe]-H_2ases, it is clear that this sub-group shares some conservation in active site mutants, but also some substitutions specific to groups within the larger sub-group.

A total of 55 sub-groups were identified from this SSN of [FeFe]-H_2ases, consisting nearly 4000 sequences with enough similarity to cluster together under strict conditions (expect values of E^{-150}). The overwhelming majority of these homologs were monomeric or multimeric [FeFe]-H_2ases, but additional domains including SLBB-, RNAP-, GS- and apparent DNA-binding-like domains were identified (Figure VI-2). SLBB domains are believed to excreted or periplasmic, where they recruit a required extracellular molecule, such as cobalamin. While studies are the SLBB fusion protein are needed, it is tempting to speculate that perhaps the evolutionary logic of this fusion is to use a H^+ gradient to transport the soluble ligand. The inclusion of PAS and apparent DNA-binding domains suggests that [FeFe]-H_2ase-like homologs were evolutionarily repurposed to recognize and transduce specific cellular conditions. These domain fusion functions become especially clear due to the recent observation of syntrophic H_2 usage within microbial communities,[5,10,11,70,76,293] highlighting the broader scope of H_2 metabolism within anaerobic and microaerobic organisms.

We focused on active site substitutions within both HydY-like H_2ases and PAS-domain fusions. Conservation of the H-cluster of HydY homologs was clearly evident. Substitutions within the active site and auxiliary cluster motifs suggest these evolved changes may be characteristic of the sub-groups, but further work is needed to further

elucidate the sub-grouping of these [FeFe]-H_2ase homologs. For instance, green algal, *Desulfovibrio* sp and HydA2 homologs segregate into various respective groups. All these homologs appear to bind the H-cluster in a classical manner. Differences within F-domains do not preclude this as a major discriminating factor, but additional factors may also influence the sub-grouping. Putative gas channels, proton transfer relays and electron transfer pathways may be subtly different within the sub-groups, which warrants further inspection using more advanced studies. Inspection of conserved surface residues may also indicate likely electron transfer partners *in vivo*, as would inspection of possible cellular location signals (periplasmic targeting in prokaryotes, organelle-specific sequence in eukaryotes) may also point to the *in vivo* function.

[FeFe]-H_2ase-PAS domain fusions are widespread throughout the SSN. PAS domain fusions, based on the sequence identity within supposedly conserved H-cluster binding motifs, likely do not bind an H-cluster in a classical manner, or if at all. How a signal is recognized, what the signal is, and how the signal is transduced is not clear from sequence analysis, and will require a brave soul to purify and characterize *in vitro*, likely from native source to fully understand how these proteins function.[70]

The identification of a multitude of [FeFe]-H_2ase sub-groups, with the variability of apparent H-cluster motifs, implicates the influence of the protein matrix in dictating catalysis of the H-cluster. The individual influence of protein residues at second- or even third-shell contributions could have unplumbed effects on the chemical nature of the H-cluster. Furthermore, the sub-grouping of the 4000 sequences highlights that there are determinants of [FeFe]-H_2ases that may lead to future phylogenetic grouping and

elucidate the influence of the protein framework on catalysis. Understanding the influence of various evolved [FeFe]-H_2ase homologs may lead to improved small molecule H-cluster mimics that have increased catalytic rates or minimized O_2-induced damage.

CHAPTER VII

CONCLUDING REMARKS

The function-discovery project for the *Cs*HydY, the [FeFe]-H_2ase-Rbr fusion, started out with simple, relatively straightforward questions: 1) Is *Cs*HydY the first O_2-tolerant [FeFe]-H_2ase? 2) If so, then how? And finally, 3) Why does this fusion protein exist? At the time (~2010), recombinant studies with [FeFe]-H_2ases were exploding onto the scientific scene. Exploratory studies had, at the time, recently identified recombinant systems for expressing [FeFe]-H_2ases with the required maturation machinery, HydE, F and G.[102] And now, unraveling the mechanism of [FeFe]-H_2ase biosynthesis appears to be the nouveau research avenue. Before the seminal discovery of the minimal maturation machinery, [FeFe]-H_2ase research relied on purifying material from native sources, limiting diversity of research groups capable of probing this enzyme. Recombinant protein production allowed for increased yield of protein, enhancing the scientific community's understanding of [FeFe]-H_2ase mechanism and function. Sample intensive techniques, such as EPR, FT-IR, protein crystallography and X-ray absorption spectroscopy were now ripe for study with these increased protein yields. Now, researchers were capable of – and this is truly the amazing part to me – choosing to expose their precious preparations of [FeFe]-H_2ases to O_2 in order to elaborate the mechanism of O_2 induced destruction of the H-cluster. At the time I started this project, irreversible damage by O_2 was speculated to result from O_2 diffusion into the active site, where it ultimately led to loss of the cubane [4Fe-4S].[93,294,295] The current model of O_2-based degradation of the [FeFe]-H_2ase active site is now thought to first result in the loss

of the $[2Fe]_H$.[296] We reasoned that if ROS were the source of [FeFe]-H_2ase inactivation, then [FeFe]-H_2ases with the inherent ability to remove such species (a la a rubrerythrin module) might result in a more O_2 tolerant enzyme. In retrospect, these all were somewhat naïve speculations. Rubrerythrins are poor O_2 reduction catalysts, and require external reducing equivalents, in the form of one electron transfers, for catalysis. Any such rubrerythrin based system would eventually suffer the same fate as an [FeFe]-H_2ase. Regardless, a story of *Cs*HydY function eventually came together. Using insights gleaned from giants in the field of H_2ase research, from the pioneers and prolific publishers,[1,7,46,60,67,83,90,117,219,220,248,253] we improved our hypothesis for the function of this truly novel fusion protein. It is on the shoulders of giants in which we can now annotate the function of *Cs*HydY.

Using a coupled biochemical and electrochemical approach, we found that *Cs*HydY is a poor H^+ reduction catalyst and readily consumes H_2, making it the first electrochemical study (initial work with *Cp*II[72,74,235]) of an [FeFe]-H_2ase that was catalytically biased toward H_2 oxidation. In fact, our careful biochemical work agreed with our electrochemical measurements. This catalytic bias discovery was met by significant barriers, namely the (incorrect) assumption that [FeFe]-H_2ases are biased toward H^+ reduction. In fact, [FeFe]-H_2ases are the superior H_2ase catalysts,[38] producing and consuming H_2 at least an order of magnitude faster than their [NiFe]-H_2ase counterparts.[40] Additionally, we found that H^+ reduction *Cs*HydY was inhibited by H_2 and it was much less susceptible to anaerobic oxidative inactivation. This observation did not escape our collaborators, who then reconstituted unmaturated HydY constructs

with synthetic mimics to convince themselves of the result. The fact that enzymes can be matured with biomimetic compounds still astounds me.[60,117] Thus, *Cs*HydY appears to have evolved to function in manner somewhere between that of both [NiFe]- and [FeFe]-H_2ases. Not only this, but we also showed that electrons from H_2 can be transferred from the H_2ase domain to Rbr domain. Because our Rbr construct showed surprisingly high catalytic efficiency when reduced from NADH, we speculated that HydY likely functions as a H_2-dependent peroxidase.

Though we have assigned a putative function for *Cs*HydY, it is by no means an open-and-closed case. The lack of conclusive H_2 dependency on the peroxidase catalysis is an open wound. We speculate that reduction of Rbr domain from dissolved H_2 could be used to reduce ROS, but do not directly, experimental 'prove' the function. We have now designed, and plan to attempt forays with as soon as possible, an assay to test our hypothesis. Using a coupled horse-radish peroxidase assay, we will incubate the HydY constructs with H_2O_2 and various concentrations of dissolved H_2 and measure, indirectly, the amount of H_2O_2 consumed. This will, in theory, allow for direct counting of electrons required to consume H_2. We speculate that HydY will function in a stoichiometric manner, *i.e.* no non-productive turnover of H_2. While these studies might include a possible function *in vitro*, the true function *in vivo* is an enigma wrapped in a mystery. Unraveling the function in a host organism would be the cherry on the proverbial sundae. We have a potential collaborator here at Texas A&M that is willing to help use grow *Clostridium scindens*, which encodes a homolog of HydY. We have envisioned quantitative RT-PCR and h*ydY* gene knock-out studies to elucidate the role

this protein plays in anaerobic bacteria. I believe these studies are paramount to assigning H_2-dependent peroxidase chemistry to HydY.

Using mutagenesis, bioinformatics and computational studies, we have also identified conserved residues that provide second-shell interactions with the H-cluster that are the likely molecular determinants for HydY's catalytic bias. The initial idea of hydrogen bonding donor interacting with CO ligands was difficult comprehend, but it is now clear that these residues act like Lewis acids near the H-cluster. Understanding the fundamental chemistry here and potential implications for biomimetic complexes are natural segues. Clearly, the next frontier for biomimetic compounds will be the rational design and incorporation of controlled second-sphere interactions with catalysts. I believe that the interactions identified in *Cs*HydY will result in incorporation of Lewis acid-like moieties near the bridging CO to stabilize this important ligand. Sequence similarity networks of nearly 4000 [FeFe]-H_2ase sequences lead to the development of 55 sub-group sequences. While there are clear modularity in the domain architectures of these sequences, differences in the domains cannot completely account the sub-groupings of the sequences. Further, more in-depth analysis is warranted to investigate potential surface exposed domains, which might be important for protein-protein interactions, putative gas-channels, H^+ relays or even other nearby active site substitutions that are I mistakenly overlooked. Of all the various domain architectures identified in the [FeFe]-H_2ase SSN, the fusions with SLBB and ATPase AA domains caught my attention. How these enzymes might function continually occupy my thoughts. My hope is that this SSN will spark the curiosity of at least one brave scientist

to investigate their roles. That, or I will just have to do it eventually. The broad swath of potential chemical diversity that are central to [FeFe]-H_2ases astounds me, and underscores the extents to which evolution pushes the repurposing of these old enzymes for new functions.

REFERENCES

1 Stephenson, M. & Stickland, L. H. Hydrogenase: a bacterial enzyme activating molecular hydrogen: The properties of the enzyme. *Biochem J* **25**, 205-214, (1931).

2 Vignais, P. M., Billoud, B. & Meyer, J. Classification and phylogeny of hydrogenases. *Fems Microbiology Reviews* **25**, 455-501, (2001).

3 Vignais, P. M. & Billoud, B. Occurrence, classification, and biological function of hydrogenases: an overview. *Chem Rev* **107**, 4206-4272, (2007).

4 Schwartz E, F. J., Friedrich B. in *The Prokaryotes - Prokaryotic Physiology and Biochemistry* 545-577 (2013).

5 Greening, C. *et al.* Genomic and metagenomic surveys of hydrogenase distribution indicate H_2 is a widely utilised energy source for microbial growth and survival. *ISME J*, (2015).

6 Meyer, J. [FeFe] hydrogenases and their evolution: a genomic perspective. *Cell Mol Life Sci* **64**, 1063-1084, (2007).

7 Lubitz, W., Ogata, H., Rüdiger, O. & Reijerse, E. Hydrogenases. *Chem Rev* **114**, 4081-4148, (2014).

8 Conrad, R. Soil microorganisms as controllers of atmospheric trace gases (H2, CO, CH4, OCS, N2O, and NO). *Microbiol Rev* **60**, 609-640, (1996).

9 Wolf, P. G., Biswas, A., Morales, S. E., Greening, C. & Gaskins, H. R. H metabolism is widespread and diverse among human colonic microbes. *Gut Microbes*, 0, (2016).

10 Ballor, N. R., Paulsen, I. & Leadbetter, J. R. Genomic analysis reveals multiple [FeFe] hydrogenases and hydrogen sensors encoded by treponemes from the H(2)-rich termite gut. *Microb Ecol* **63**, 282-294, (2012).

11 Fischbach, M. A. & Sonnenburg, J. L. Eating for two: how metabolism establishes interspecies interactions in the gut. *Cell Host Microbe* **10**, 336-347, (2011).

12 Schmitz, R. A., Daniel, R., Deppenmeier, U. & Gottschalk, G. The Anaerobic Way of Life. *Prokaryotes: A Handbook on the Biology of Bacteria, Vol 2, Third Edition*, 86-101, (2006).

13 Vardar-Schara, G., Maeda, T. & Wood, T. K. Metabolically engineered bacteria for producing hydrogen via fermentation. *Microb Biotechnol* **1**, 107-125, (2008).

14 Calusinska, M., Happe, T., Joris, B. & Wilmotte, A. The surprising diversity of clostridial hydrogenases: a comparative genomic perspective. *Microbiology* **156**, 1575-1588, (2010).

15 Schut, G. J. & Adams, M. W. The iron-hydrogenase of *Thermotoga maritima* utilizes ferredoxin and NADH synergistically: a new perspective on anaerobic hydrogen production. *J Bacteriol* **191**, 4451-4457, (2009).

16 Ragsdale, S. W. Pyruvate ferredoxin oxidoreductase and its radical intermediate. *Chem Rev* **103**, 2333-2346, (2003).

17 Furdui, C. & Ragsdale, S. W. The role of pyruvate ferredoxin oxidoreductase in pyruvate synthesis during autotrophic growth by the Wood-Ljungdahl pathway. *J Biol Chem* **275**, 28494-28499, (2000).

18 Posewitz, M. C., Dubini, A., Meuser, J. E., Seibert, M. & Ghirardi, M. L. Hydrogenases, Hydrogen Production, and Anoxia. *The Chlamydomonas Sourcebook 3-Vol set* **2**, 217-255, (2009).

19 Chou, C. J., Jenney, F. E., Jr., Adams, M. W. & Kelly, R. M. Hydrogenesis in hyperthermophilic microorganisms: implications for biofuels. *Metab Eng* **10**, 394-404, (2008).

20 Wang, S., Huang, H., Kahnt, J. & Thauer, R. K. A reversible electron-bifurcating ferredoxin- and NAD-Dependent [FeFe]-Hydrogenase (HydABC) in Moorella thermoacetica. *Journal of Bacteriology* **195**, 1267-1275, (2013).

21 Poehlein, A. *et al.* An ancient pathway combining carbon dioxide fixation with the generation and utilization of a sodium ion gradient for ATP synthesis. *PLoS One* **7**, e33439, (2012).

22 Schuchmann, K. & Muller, V. A bacterial electron-bifurcating hydrogenase. *J Biol Chem* **287**, 31165-31171, (2012).

23 Schut, G. J. & Adams, M. W. W. The iron-hydrogenase of Thermotoga maritima utilizes ferredoxin and NADH synergistically: a new perspective on anaerobic hydrogen production. *Journal of Bacteriology* **191**, 4451-4457, (2009).

24 Zhou, Z. *et al.* Ammonia fermentation, a novel anoxic metabolism of nitrate by fungi. *J Biol Chem* **277**, 1892-1896, (2002).

25 McDowall, J. S. *et al.* Bacterial formate hydrogenlyase complex. *P Natl Acad Sci USA* **111**, E3948-3956, (2014).

26 Ghirardi, M. L., Dubini, A., Yu, J. & Maness, P. C. Photobiological hydrogen-producing systems. *Chem Soc Rev* **38**, 52-61, (2009).

27 Hu, Y. & Ribbe, M. W. Nitrogenase and homologs. *J Biol Inorg Chem* **20**, 435-445, (2015).

28 Hu, Y. & Ribbe, M. W. A journey into the active center of nitrogenase. *J Biol Inorg Chem* **19**, 731-736, (2014).

29 Ribbe, M. W., Hu, Y., Hodgson, K. O. & Hedman, B. Biosynthesis of nitrogenase metalloclusters. *Chem Rev* **114**, 4063-4080, (2014).

30 Bothe, H., Schmitz, O., Yates, M. G. & Newton, W. E. Nitrogen fixation and hydrogen metabolism in cyanobacteria. *Microbiol Mol Biol Rev* **74**, 529-551, (2010).

31 Seefeldt, L. C., Hoffman, B. M. & Dean, D. R. Mechanism of Mo-dependent nitrogenase. *Annu Rev Biochem* **78**, 701-722, (2009).

32 Wu, M. *et al.* Life in hot carbon monoxide: the complete genome sequence of Carboxydothermus hydrogenoformans Z-2901. *PLoS Genet* **1**, e65, (2005).

33 Cracknell, J. A., Wait, A. F., Lenz, O., Friedrich, B. & Armstrong, F. A. A kinetic and thermodynamic understanding of O2 tolerance in [NiFe]-hydrogenases. *Proc Natl Acad Sci U S A* **106**, 20681-20686, (2009).

34 Vincent, K. A. *et al.* Electrochemical definitions of O_2 sensitivity and oxidative inactivation in hydrogenases. *J Am Chem Soc* **127**, 18179-18189, (2005).

35 Shomura, Y., Yoon, K. S., Nishihara, H. & Higuchi, Y. Structural basis for a [4Fe-3S] cluster in the oxygen-tolerant membrane-bound [NiFe]-hydrogenase. *Nature* **479**, 253-256, (2011).

36 Liang, Y. *et al.* Increased biological hydrogen production by deletion of hydrogen-uptake system in photosynthetic bacteria. *Microbiol Res* **164**, 674-679, (2009).

37 Shima, S. *et al.* The crystal structure of [Fe]-hydrogenase reveals the geometry of the active site. *Science (New York, N.Y.)* **321**, 572-575, (2008).

38 Frey, M. Hydrogenases: hydrogen-activating enzymes. *ChemBioChem* **3**, 153-160, (2002).

39 Cammack, R. Redox enzymes. Splitting molecular hydrogen. *Nature* **373**, (1995).

40 Adams, M. W. The structure and mechanism of iron-hydrogenases. *Biochim Biophys Acta* **1020**, 115-145, (1990).

41 Cammack, R. Hydrogenase sophistication. *Nature* **397**, 214-215, (1999).

42 Pilak, O. *et al.* The crystal structure of the apoenzyme of the iron-sulphur cluster-free hydrogenase. *J Mol Biol* **358**, 798-809, (2006).

43 Korbas, M. *et al.* The iron-sulfur cluster-free hydrogenase (Hmd) is a metalloenzyme with a novel iron binding motif. *J Biol Chem* **281**, 30804-30813, (2006).

44 Shima, S. & Thauer, R. K. A third type of hydrogenase catalyzing H2 activation. *Chem Rec* **7**, 37-46, (2007).

45 Hiromoto, T. *et al.* The crystal structure of C176A mutated [Fe]-hydrogenase suggests an acyl-iron ligation in the active site iron complex. *FEBS Lett* **583**, 585-590, (2009).

46 Fontecilla-Camps, J. C., Volbeda, A., Cavazza, C. & Nicolet, Y. Structure/function relationships of [NiFe]- and [FeFe]-hydrogenases. *Chem Rev* **107**, 4273-4303, (2007).

47 Lubitz, W., Reijerse, E. & van Gastel, M. [NiFe] and [FeFe] hydrogenases studied by advanced magnetic resonance techniques. *Chem Rev* **107**, 4331-4365, (2007).

48 Dementin, S. *et al.* Introduction of methionines in the gas channel makes [NiFe] hydrogenase aero-tolerant. *Journal of the American Chemical Society* **131**, 10156-10164, (2009).

49 Cracknell, J. a., Wait, A. F., Lenz, O., Friedrich, B. & Armstrong, F. a. A kinetic and thermodynamic understanding of O2 tolerance in [NiFe]-hydrogenases. *Proceedings of the National Academy of Sciences of the United States of America* **106**, 20681-20686, (2009).

50 Buhrke, T., Lenz, O., Krauss, N. & Friedrich, B. Oxygen tolerance of the H2-sensing [NiFe] hydrogenase from Ralstonia eutropha H16 is based on limited access of oxygen to the active site. *J Biol Chem* **280**, 23791-23796, (2005).

51 Pandelia, M. E. *et al.* Characterization of a unique [FeS] cluster in the electron transfer chain of the oxygen tolerant [NiFe] hydrogenase from Aquifex aeolicus. *Proc Natl Acad Sci U S A* **108**, 6097-6102, (2011).

52 Fritsch, J. *et al.* The crystal structure of an oxygen-tolerant hydrogenase uncovers a novel iron-sulphur centre. *Nature*, 3-7, (2011).

53 Fritsch, J., Lenz, O. & Friedrich, B. Structure, function and biosynthesis of O(2)-tolerant hydrogenases. *Nat Rev Microbiol* **11**, 106-114, (2013).

54 Lauterbach, L. & Lenz, O. Catalytic production of hydrogen peroxide and water by oxygen-tolerant [NiFe]-hydrogenase during H2 cycling in the presence of O2. *J Am Chem Soc* **135**, 17897-17905, (2013).

55 Evans, R. M. *et al.* Principles of sustained enzymatic hydrogen oxidation in the presence of oxygen--the crucial influence of high potential Fe-S clusters in the electron relay of [NiFe]-hydrogenases. *J Am Chem Soc* **135**, 2694-2707, (2013).

56 Parkin, A. & Sargent, F. The hows and whys of aerobic H2 metabolism. *Curr Opin Chem Biol* **16**, 26-34, (2012).

57 Vincent, K. a. *et al.* Electricity from low-level H2 in still air--an ultimate test for an oxygen tolerant hydrogenase. *Chemical communications (Cambridge, England)*, 5033-5035, (2006).

58 Winkler, M., Esselborn, J. & Happe, T. Molecular basis of [FeFe]-hydrogenase function: an insight into the complex interplay between protein and catalytic cofactor. *Biochim Biophys Acta* **1827**, 974-985, (2013).

59 Poehlein, A. *et al.* An ancient pathway combining carbon dioxide fixation with the generation and utilization of a sodium ion gradient for ATP synthesis. *PloS One* **7**, e33439, (2012).

60 Berggren, G. *et al.* Biomimetic assembly and activation of [FeFe]-hydrogenases. *Nature* **499**, 66-69, (2013).

61 Peters, J. W. & Broderick, J. B. Emerging paradigms for complex iron-sulfur cofactor assembly and insertion. *Annu Rev Biochem* **81**, 429-450, (2012).

62 Adams, M. W. W. & Mortenson, L. E. The physical and catalytic properties of hydrogenase II of Clostridium pasteurianum. A comparison with hydrogenase I. *Journal of Biological Chemistry* **259**, 7045-7055, (1984).

63 Forestier, M. *et al.* Expression of two [Fe] -hydrogenases in Chlamydomonas reinhardtii under anaerobic conditions. *Eur J Biochem* **2758**, 2750-2758, (2003).

64 Girbal, L. *et al.* Homologous and heterologous overexpression in Clostridium acetobutylicum and characterization of purified clostridial and algal Fe-only hydrogenases with high specific activities. *Appl Environ Microbiol* **71**, 2777-2781, (2005).

65 Ghirardi, M. L. *et al.* Microalgae: a green source of renewable H(2). *Trends in Biotechnology* **18**, 506-511, (2000).

66 Ghirardi, M. L. *et al.* Hydrogenases and hydrogen photoproduction in oxygenic photosynthetic organisms. *Annu Rev Plant Biol* **58**, 71-91, (2007).

67 Nicolet, Y., Piras, C., Legrand, P., Hatchikian, C. E. & Fontecilla-Camps, J. C. Desulfovibrio desulfuricans iron hydrogenase: the structure shows unusual coordination to an active site Fe binuclear center. *Struct Fold Des* **7**, 13-23, (1999).

68 Nicolet, Y. *et al.* Crystallographic and FTIR spectroscopic evidence of changes in Fe coordination upon reduction of the active site of the Fe-only hydrogenase from Desulfovibrio desulfuricans. *J Am Chem Soc* **123**, 1596-1601, (2001).

69 Thauer, R. K., Jungermann, K. & Decker, K. Energy conservation in chemotrophic anaerobic bacteria. *Bacteriol Rev* **41**, 100-180, (1977).

70 Zheng, Y., Kahnt, J., Kwon, I. H., Mackie, R. I. & Thauer, R. K. Hydrogen Formation and its Regulation in Ruminococcus albus: Involvement of an Electron-Bifurcating [FeFe]-Hydrogenase, of a Non Electron-bifurcating [FeFe]-hydrogenase and of a Putative Hydrogen-Sensing [FeFe]-Hydrogenase. *J Bacteriol* **196**, 3840-3852, (2014).

71 Schuchmann, K. & Muller, V. Direct and reversible hydrogenation of Co2 to formate by a bacterial carbon dioxide reductase. *Science* **342**, 1382-1386, (2013).

72 Chen, J. S. & Blanchard, D. K. Isolation and properties of a unidirectional H2-oxidizing hydrogenase from the strictly anaerobic N2-fixing bacterium Clostridium pasteurianum W5. *Biochem Biophys Res Commun* **84**, 1144-1150, (1978).

73 Adams, M. & Mortenson, L. The purification of hydrogenase II (uptake hydrogenase) from the anaerobic N2-fixing bacterium Clostridium pasteurianum. *Biochimica et Biophysica Acta (BBA) - Bioenergetics* **766**, 51-61, (1984).

74 Adams, M. W. & Mortenson, L. E. The physical and catalytic properties of hydrogenase II of *Clostridium pasteurianum*. *J Biol Chem* **259**, 7045-7055, (1984).

75 Adams, M. W. W. The mechanisms of hydrogen activation and carbon monoxide binding by hydrogenase I and hydrogenase II of Clostridium pasteurianum. *Journal of Biological Chemistry* **262**, 15054-15061, (1987).

76 Schmidt, O., Drake, H. L. & Horn, M. A. Hitherto unknown [Fe-Fe]-hydrogenase gene diversity in anaerobes and anoxic enrichments from a moderately acidic fen. *Appl Environ Microbiol* **76**, 2027-2031, (2010).

77 Suzuki, A. & Knaff, D. B. Glutamate synthase: structural, mechanistic and regulatory properties, and role in the amino acid metabolism. *Photosynth Res* **83**, 191-217, (2005).

78 Ballor, N. R. & Leadbetter, J. R. Analysis of extensive [FeFe] hydrogenase gene diversity within the gut microbiota of insects representing five families of Dictyoptera. *Microb Ecol* **63**, 586-595, (2012).

79 Hackstein, J. H. P. Eukaryotic Fe-hydrogenases -- old eukaryotic heritage or adaptive acquisitions? *Biochemical Society transactions* **33**, 47-50, (2005).

80 Lill, R., Srinivasan, V. & Muhlenhoff, U. The role of mitochondria in cytosolic-nuclear iron-sulfur protein biogenesis and in cellular iron regulation. *Curr Opin Microbiol* **22**, 111-119, (2014).

81 Lill, R. & Muhlenhoff, U. Maturation of iron-sulfur proteins in eukaryotes: mechanisms, connected processes, and diseases. *Annu Rev Biochem* **77**, 669-700, (2008).

82 Pershad, H. R. *et al.* Catalytic electron transport in Chromatium vinosum [NiFe]-hydrogenase: application of voltammetry in detecting redox-active centers and establishing that hydrogen oxidation is very fast even at potentials close to the reversible H+/H2 value. *Biochemistry* **38**, 8992-8999, (1999).

83 Vincent, K. A., Parkin, A. & Armstrong, F. A. Investigating and exploiting the electrocatalytic properties of hydrogenases. *Chem Rev* **107**, 4366-4413, (2007).

84 Leger, C. *et al.* Enzyme electrokinetics: using protein film voltammetry to investigate redox enzymes and their mechanisms. *Biochemistry* **42**, 8653-8662, (2003).

85 Jones, A. K. *et al.* Enzyme electrokinetics: electrochemical studies of the anaerobic interconversions between active and inactive states of *Allochromatium vinosum* [NiFe]-hydrogenase. *J Am Chem Soc* **125**, 8505-8514, (2003).

86 Baffert, C. *et al.* Covalent attachment of FeFe hydrogenases to carbon electrodes for direct electron transfer. *Anal Chem* **84**, 7999-8005, (2012).

87 Le Goff, A. *et al.* From hydrogenases to noble metal-free catalytic nanomaterials for H2 production and uptake. *Science* **326**, 1384-1387, (2009).

88 Bard, A. J. & Faulkner, L. R. *Electrochemical Methods : Fundamentals and Applications*. 2nd edn, (Wiley, 2001).

89 Murphy, B. J., Sargent, F. & Armstrong, F. a. Transforming an oxygen-tolerant [NiFe] uptake hydrogenase into a proficient, reversible hydrogen producer. *Energy & Environmental Science* **7**, 1426-1433, (2014).

90 Armstrong, F. A. *et al.* Guiding Principles of Hydrogenase Catalysis Instigated and Clarified by Protein Film Electrochemistry. *Accounts of Chemical Research*, acs.accounts.6b00027, (2016).

91 Hexter, S. V., Grey, F., Happe, T., Climent, V. & Armstrong, F. A. Correction for Hexter et al., Electrocatalytic mechanism of reversible hydrogen cycling by enzymes and distinctions between the major classes of hydrogenases. *Proceedings of the National Academy of Sciences* **109**, 18232-18233, (2012).

92 Lukey, M. J. *et al.* How Escherichia coli is equipped to oxidize hydrogen under different redox conditions. *J Biol Chem* **285**, 3928-3938, (2010).

93 Goldet, G. *et al.* Electrochemical kinetic investigations of the reactions of [FeFe]-hydrogenases with carbon monoxide and oxygen: comparing the importance of gas tunnels and active-site electronic/redox effects. *Journal of the American Chemical Society* **131**, 14979-14989, (2009).

94 Parkin, A., Cavazza, C., Fontecilla-Camps, J. C. & Armstrong, F. A. Electrochemical investigations of the interconversions between catalytic and inhibited states of the [FeFe]-hydrogenase from *Desulfovibrio desulfuricans*. *J Am Chem Soc* **128**, 16808-16815, (2006).

95 Armstrong, F. A. Hydrogenases: active site puzzles and progress. *Curr Opin Chem Biol* **8**, 133-140, (2004).

96 Fourmond, V. *et al.* The mechanism of inhibition by H_2 of H_2-evolution by hydrogenases. *Chem Commun* **49**, 6840-6842, (2013).

97 Vincent, K. a. *et al.* Electrochemical definitions of O2 sensitivity and oxidative inactivation in hydrogenases. *Journal of the American Chemical Society* **127**, 18179-18189, (2005).

98 Hexter, S. V., Grey, F., Happe, T., Climent, V. & Armstrong, F. A. Electrocatalytic mechanism of reversible hydrogen cycling by enzymes and distinctions between the major classes of hydrogenases. *Proc Natl Acad Sci U S A* **109**, 11516-11521, (2012).

99 Forzi, L. & Sawers, R. G. Maturation of [NiFe]-hydrogenases in Escherichia coli. *Biometals* **20**, 565-578, (2007).

100 Mulder, D. W. *et al.* Insights into [FeFe]-Hydrogenase Structure, Mechanism, and Maturation. *Structure (London, England : 1993)* **19**, 1038-1052, (2011).

101 Posewitz, M. C. *et al.* Discovery of two novel radical S-adenosylmethionine proteins required for the assembly of an active [Fe] hydrogenase. *J Biol Chem* **279**, 25711-25720, (2004).

102 King, P. W., Posewitz, M. C., Ghirardi, M. L. & Seibert, M. Functional studies of [FeFe] hydrogenase maturation in an *Escherichia coli* biosynthetic system. *J Bacteriol* **188**, 2163-2172, (2006).

103 Mulder, D. W. *et al.* Activation of HydA(DeltaEFG) requires a preformed [4Fe-4S] cluster. *Biochemistry* **48**, 6240-6248, (2009).

104 Czech, I., Silakov, A., Lubitz, W. & Happe, T. The [FeFe]-hydrogenase maturase HydF from Clostridium acetobutylicum contains a CO and CN- ligated iron cofactor. *FEBS Lett* **584**, 638-642, (2010).

105 Shepard, E. M. *et al.* [FeFe]-hydrogenase maturation: HydG-catalyzed synthesis of carbon monoxide. *Journal of the American Chemical Society* **132**, 9247-9249, (2010).

106 Driesener, R. C. *et al.* [FeFe]-hydrogenase cyanide ligands derived from S-adenosylmethionine-dependent cleavage of tyrosine. *Angewandte Chemie (International ed. in English)* **49**, 1687-1690, (2010).

107 Suess, D. L. M., Kuchenreuther, J. M., De La Paz, L., Swartz, J. R. & Britt, R. D. Biosynthesis of the [FeFe] Hydrogenase H Cluster: A Central Role for the Radical SAM Enzyme HydG. *Inorganic Chemistry* **55**, 478-487, (2016).

108 Suess, D. L. *et al.* The Radical SAM Enzyme HydG Requires Cysteine and a Dangler Iron for Generating an Organometallic Precursor to the [FeFe]-Hydrogenase H-Cluster. *J Am Chem Soc* **138**, 1146-1149, (2016).

109 Kuchenreuther, J. M. *et al.* The HydG enzyme generates an Fe(CO)2(CN) synthon in assembly of the FeFe hydrogenase H-cluster. *Science* **343**, 424-427, (2014).

110 Peters, J. W. *et al.* [FeFe]- and [NiFe]-hydrogenase diversity, mechanism, and maturation. *Biochim Biophys Acta* **1853**, 1350-1369, (2015).

111 Boswell, N. *Biochemical Characterization of the -hydrogenase Maturation Protein HydE and Identification of the Substrate* Master of Science thesis, Montana State University, (2011).

112 Betz, J. N. *et al.* [FeFe]-hydrogenase maturation: insights into the role HydE plays in dithiomethylamine biosynthesis. *Biochemistry* **54**, 1807-1818, (2015).

113 Kuchenreuther, J. M., Stapleton, J. A. & Swartz, J. R. Tyrosine, cysteine, and S-adenosyl methionine stimulate in vitro [FeFe] hydrogenase activation. *PLoS One* **4**, e7565, (2009).

114 Rohac, R. *et al.* Carbon-sulfur bond-forming reaction catalysed by the radical SAM enzyme HydE. *Nat Chem* **8**, 491-500, (2016).

115 Mulder, D. W. *et al.* Stepwise [FeFe]-hydrogenase H-cluster assembly revealed in the structure of HydA(DeltaEFG). *Nature* **465**, 248-251, (2010).

116 Cendron, L. *et al.* Crystal structure of HydF scaffold protein provides insights into [FeFe]-hydrogenase maturation. *J Biol Chem* **286**, 43944-43950, (2011).

117 Esselborn, J. *et al.* Spontaneous activation of [FeFe]-hydrogenases by an inorganic [2Fe] active site mimic. *Nat Chem Biol* **9**, 607-609, (2013).

118 Esselborn, J. *et al.* A structural view of synthetic cofactor integration into [FeFe]-hydrogenases. *Chem. Sci.*, (2016).

119 Vincent, K. A. *et al.* Electrocatalytic hydrogen oxidation by an enzyme at high carbon monoxide or oxygen levels. *Proc Natl Acad Sci U S A* **102**, 16951-16954, (2005).

120 Imlay, J. A. Iron-sulphur clusters and the problem with oxygen. *Mol Microbiol* **59**, 1073-1082, (2006).

121 Mishra, S. & Imlay, J. A. An anaerobic bacterium, *Bacteroides thetaiotaomicron*, uses a consortium of enzymes to scavenge hydrogen peroxide. *Mol Microbiol* **90**, 1356-1371, (2013).

122 Mishra, S. & Imlay, J. Why do bacteria use so many enzymes to scavenge hydrogen peroxide? *Arch Biochem Biophys* **525**, 145-160, (2012).

123 Kawasaki, S. *et al.* Adaptive responses to oxygen stress in obligatory anaerobes Clostridium acetobutylicum and Clostridium aminovalericum. *Appl Environ Microbiol* **71**, 8442-8450, (2005).

124 Hillmann, F., Fischer, R. J., Saint-Prix, F., Girbal, L. & Bahl, H. PerR acts as a switch for oxygen tolerance in the strict anaerobe *Clostridium acetobutylicum*. *Mol Microbiol* **68**, 848-860, (2008).

125 Wood, P. M. The potential diagram for oxygen at pH 7. *Biochem J* **253**, 287-289, (1988).

126 Fridovich, I. Fundamental aspects of reactive oxygen species, or what's the matter with oxygen? *Ann N Y Acad Sci* **893**, 13-18, (1999).

127 Imlay, J. A. The molecular mechanisms and physiological consequences of oxidative stress: lessons from a model bacterium. *Nat Rev Microbiol* **11**, 443-454, (2013).

128 Kurtz, D. M., Jr. Avoiding high-valent iron intermediates: superoxide reductase and rubrerythrin. *J Inorg Biochem* **100**, 679-693, (2006).

129 Seaver, L. C. & Imlay, J. A. Are respiratory enzymes the primary sources of intracellular hydrogen peroxide? *J Biol Chem* **279**, 48742-48750, (2004).

130 Seaver, L. C. & Imlay, J. A. Hydrogen peroxide fluxes and compartmentalization inside growing Escherichia coli. *J Bacteriol* **183**, 7182-7189, (2001).

131 Weinberg, S. E. & Chandel, N. S. Targeting mitochondria metabolism for cancer therapy. *Nat Chem Biol* **11**, 9-15, (2015).

132 Thom, S. R. Hyperbaric Oxygen: Its Mechanisms and Efficacy. *Plast Reconstr Surg* **127**, 131s-141s, (2011).

133 Apel, K. & Hirt, H. Reactive oxygen species: metabolism, oxidative stress, and signal transduction. *Annu Rev Plant Biol* **55**, 373-399, (2004).

134 Loew, O. A New Enzyme of General Occurrence in Organismis. *Science* **11**, 701-702, (1900).

135 Whittaker, J. W. Non-heme manganese catalase--the 'other' catalase. *Arch Biochem Biophys* **525**, 111-120, (2012).

136 Sheng, Y. *et al.* Superoxide dismutases and superoxide reductases. *Chem Rev* **114**, 3854-3918, (2014).

137 Parsonage, D., Karplus, P. A. & Poole, L. B. Substrate specificity and redox potential of AhpC, a bacterial peroxiredoxin. *Proc Natl Acad Sci U S A* **105**, 8209-8214, (2008).

138 Lumppio, H. L., Shenvi, N. V., Summers, A. O., Voordouw, G. & Kurtz D.M., J. Rubrerythrin and rubredoxin oxidoreductase in Desulfovibrio vulgaris: A novel oxidative stress protection system. *Journal of Bacteriology* **183**, 101-108, (2001).

139 Hentges, D. J. in *Medical Microbiology* (ed S. Baron) (1996).

140 Abhyankar, W. *et al.* In pursuit of protein targets: proteomic characterization of bacterial spore outer layers. *J Proteome Res* **12**, 4507-4521, (2013).

141 Permpoonpattana, P. *et al.* Functional characterization of Clostridium difficile spore coat proteins. *J Bacteriol* **195**, 1492-1503, (2013).

142 Checinska, A., Burbank, M. & Paszczynski, A. J. Protection of Bacillus pumilus Spores by Catalases. *Applied and Environmental Microbiology* **78**, 6413-6422, (2012).

143 Lumppio, H. L., Shenvi, N. V., Summers, A. O., Voordouw, G. & Kurtz, D. M., Jr. Rubrerythrin and rubredoxin oxidoreductase in Desulfovibrio vulgaris: a novel oxidative stress protection system. *J Bacteriol* **183**, 101-108, (2001).

144 Thorgersen, M. P., Stirrett, K., Scott, R. A. & Adams, M. W. Mechanism of oxygen detoxification by the surprisingly oxygen-tolerant hyperthermophilic archaeon, Pyrococcus furiosus. *Proc Natl Acad Sci U S A* **109**, 18547-18552, (2012).

145 Riebe, O., Fischer, R. J. & Bahl, H. Desulfoferrodoxin of Clostridium acetobutylicum functions as a superoxide reductase. *FEBS Letters* **581**, 5605-5610, (2007).

146 Grunden, A. M. *et al.* In vitro reconstitution of an NADPH-dependent superoxide reduction pathway from Pyrococcus furiosus. *Appl Environ Microbiol* **71**, 1522-1530, (2005).

147 Fournier, M., Dermoun, Z., Durand, M. C. & Dolla, A. A new function of the Desulfovibrio vulgaris Hildenborough [Fe] hydrogenase in the protection against oxidative stress. *J Biol Chem* **279**, 1787-1793, (2004).

148 Adams, M. W., Jenney, F. E., Jr., Clay, M. D. & Johnson, M. K. Superoxide reductase: fact or fiction? *J Biol Inorg Chem* **7**, 647-652, (2002).

149 Huynh, B. H. *et al.* Desulfovibrio vulgaris hydrogenase: a nonheme iron enzyme lacking nickel that exhibits anomalous EPR and Mössbauer spectra. *P Natl Acad Sci USA* **81**, 3728-3732, (1984).

150 LeGall, J. *et al.* Isolation and characterization of rubrerythrin, a non-heme iron protein from *Desulfovibrio vulgaris* that contains rubredoxin centers and a hemerythrin-like binuclear iron cluster. *Biochemistry* **27**, 1636-1642, (1988).

151 Ravi, N., Prickril, B. C., Kurtz, D. M. & Huynh, B. H. Spectroscopic characterization of 57Fe-reconstituted rubrerythrin, a non-heme iron protein with structural analogies to ribonucleotide reductase. *Biochemistry* **32**, 8487-8491, (1993).

152 Riebe, O., Fischer, R. J., Wampler, D. A., Kurtz, D. M., Jr. & Bahl, H. Pathway for H_2O_2 and O_2 detoxification in *Clostridium acetobutylicum*. *Microbiology* **155**, 16-24, (2009).

153 Prickril, B. C., Kurtz, D. M., LeGall, J. & Voordouw, G. Cloning and sequencing of the gene for rubrerythrin from Desulfovibrio vulgaris (Hildenborough). *Biochemistry* **30**, 11118-11123, (1991).

154 Coulter, E. D., Shenvi, N. V. & Kurtz, D. M., Jr. NADH peroxidase activity of rubrerythrin. *Biochem Biophys Res Commun* **255**, 317-323, (1999).

155 Coulter, E. D. *et al.* Rubrerythrin-catalyzed substrate oxidation by dioxygen and hydrogen peroxide. *Inorganica Chimica Acta* **297**, 231-241, (2000).

156 Coulter, E. D. & Kurtz, D. M., Jr. A role for rubredoxin in oxidative stress protection in *Desulfovibrio vulgaris*: catalytic electron transfer to rubrerythrin and two-iron superoxide reductase. *Arch Biochem Biophys* **394**, 76-86, (2001).

157 Alban, P. S., Popham, D. L., Rippere, K. E. & Krieg, N. R. Identification of a gene for a rubrerythrin/nigerythrin-like protein in Spirillum volutans by using amino acid sequence data from mass spectrometry and NH2-terminal sequencing. *J Appl Microbiol* **85**, 875-882, (1998).

158 Sztukowska, M., Bugno, M., Potempa, J., Travis, J. & Kurtz, D. M., Jr. Role of rubrerythrin in the oxidative stress response of Porphyromonas gingivalis. *Mol Microbiol* **44**, 479-488, (2002).

159 Mydel, P. *et al.* Roles of the host oxidative immune response and bacterial antioxidant rubrerythrin during Porphyromonas gingivalis infection. *PLoS Pathog* **2**, e76, (2006).

160 Kawasaki, S., Sakai, Y., Takahashi, T., Suzuki, I. & Niimura, Y. O2 and reactive oxygen species detoxification complex, composed of O2-responsive NADH:rubredoxin oxidoreductase-flavoprotein A2-desulfoferrodoxin operon enzymes, rubperoxin, and rubredoxin, in Clostridium acetobutylicum. *Appl Environ Microbiol* **75**, 1021-1029, (2009).

161 Kawasaki, S. *et al.* An O2-inducible rubrerythrin-like protein, rubperoxin, is functional as a H2O2 reductase in an obligatory anaerobe Clostridium acetobutylicum. *FEBS Lett* **581**, 2460-2464, (2007).

162 Hillmann, F., Fischer, R. J. & Bahl, H. The rubrerythrin-like protein Hsp21 of Clostridium acetobutylicum is a general stress protein. *Arch Microbiol* **185**, 270-276, (2006).

163 Kawasaki, S., Ishikura, J., Watamura, Y. & Niimura, Y. Identification of O2-induced peptides in an obligatory anaerobe, Clostridium acetobutylicum. *FEBS Lett* **571**, 21-25, (2004).

164 Zhao, W., Ye, Z. & Zhao, J. RbrA, a cyanobacterial rubrerythrin, functions as a FNR-dependent peroxidase in heterocysts in protection of nitrogenase from damage by hydrogen peroxide in Anabaena sp. PCC 7120. *Mol Microbiol* **66**, 1219-1230, (2007).

165 Das, A., Coulter, E. D., Kurtz, D. M., Jr. & Ljungdahl, L. G. Five-gene cluster in Clostridium thermoaceticum consisting of two divergent operons encoding rubredoxin oxidoreductase- rubredoxin and rubrerythrin-type A flavoprotein-high-molecular-weight rubredoxin. *J Bacteriol* **183**, 1560-1567, (2001).

166 Riebe, O., Fischer, R.-J., Wampler, D. a., Kurtz, D. M. & Bahl, H. Pathway for H2O2 and O2 detoxification in Clostridium acetobutylicum. *Microbiology* **155**, 16-24, (2009).

167 Weinberg, M. V., Jenney, F. E., Jr., Cui, X. & Adams, M. W. Rubrerythrin from the hyperthermophilic archaeon Pyrococcus furiosus is a rubredoxin-dependent, iron-containing peroxidase. *J Bacteriol* **186**, 7888-7895, (2004).

168 Cooley, R. B., Arp, D. J. & Karplus, P. A. Symerythrin structures at atomic resolution and the origins of rubrerythrins and the ferritin-like superfamily. *J Mol Biol* **413**, 177-194, (2011).

169 Dillard, B. D., Demick, J. M., Adams, M. W. & Lanzilotta, W. N. A cryo-crystallographic time course for peroxide reduction by rubrerythrin from Pyrococcus furiosus. *J Biol Inorg Chem* **16**, 949-959, (2011).

170 Tempel, W. *et al.* Structural genomics of Pyrococcus furiosus: X-ray crystallography reveals 3D domain swapping in rubrerythrin. *Proteins* **57**, 878-882, (2004).

171 Jin, S., Kurtz, D. M., Liu, Z.-J., Rose, J. & Wang, B.-C. Displacement of iron by zinc at the diiron site of Desulfovibrio vulgaris rubrerythrin: X-ray crystal structure and anomalous scattering analysis. *Journal of inorganic biochemistry* **98**, 786-796, (2004).

172 Jin, S., Kurtz, D. M., Liu, Z.-J., Rose, J. & Wang, B.-C. X-ray crystal structure of Desulfovibrio vulgaris rubrerythrin with zinc substituted into the [Fe(SCys)4] site and alternative diiron site structures. *Biochemistry* **43**, 3204-3213, (2004).

173 Li, M. *et al.* Crystal structure studies on rubrerythrin: enzymatic activity in relation to the zinc movement. *J Biol Inorg Chem* **8**, 149-155, (2003).

174 Kurtz, D. & Nordlund, P. The structure of Desulfovibrio vulgaris rubrerythrin reveals a unique combination of rubredoxin-like FeS4 and ferritin-like diiron domains. *Nature Structural & Molecular Biology*, (1996).

175 Cooley, R. B., Arp, D. J. & Karplus, P. A. Evolutionary origin of a secondary structure: pi-helices as cryptic but widespread insertional variations of alpha-helices that enhance protein functionality. *J Mol Biol* **404**, 232-246, (2010).

176 Wakagi, T. Sulerythrin, the smallest member of the rubrerythrin family, from a strictly aerobic and thermoacidophilic archaeon, Sulfolobus tokodaii strain 7. *FEMS Microbiology Letters* **222**, 33-37, (2003).

177 Smoukov, S., Davydov, R. & Doan, P. EPR and ENDOR evidence for a 1-His, hydroxo-bridged mixed-valent diiron site in Desulfovibrio vulgaris rubrerythrin. *Biochemistry*, 6201-6208, (2003).

178 LeGall, J. *et al.* Isolation and characterization of rubrerythrin, a non-heme iron protein from Desulfovibrio vulgaris that contains rubredoxin centers and a hemerythrin-like binuclear iron cluster. *Biochemistry* **27**, 1636-1642, (1988).

179 Jin, S., Kurtz, D. M., Jr., Liu, Z. J., Rose, J. & Wang, B. C. Displacement of iron by zinc at the diiron site of Desulfovibrio vulgaris rubrerythrin: X-ray crystal structure and anomalous scattering analysis. *J Inorg Biochem* **98**, 786-796, (2004).

180 Jin, S., Kurtz, D. M., Jr., Liu, Z. J., Rose, J. & Wang, B. C. X-ray crystal structures of reduced rubrerythrin and its azide adduct: a structure-based mechanism for a non-heme diiron peroxidase. *J Am Chem Soc* **124**, 9845-9855, (2002).

181 Miyazaki, K. MEGAWHOP cloning: a method of creating random mutagenesis libraries via megaprimer PCR of whole plasmids. *Methods Enzymol* **498**, 399-406, (2011).

182 Wagner, S. *et al.* Tuning Escherichia coli for membrane protein overexpression. *Proc Natl Acad Sci U S A* **105**, 14371-14376, (2008).

183 Studier, F. W. Protein production by auto-induction in high-density shaking cultures. *Protein Expr Purif* **41**, 207-234, (2005).

184 McKenna, C. E., Gutheil, W. G. & Song, W. A method for preparing analytically pure sodium dithionite. Dithionite quality and observed nitrogenase-specific activities. *BBA-Gen Subjects* **1075**, 109-117, (1991).

185 Hillmann, F. *et al.* Reductive dioxygen scavenging by flavo-diiron proteins of *Clostridium acetobutylicum*. *FEBS Lett* **583**, 241-245, (2009).

186 Eidsness, M. K., Richie, K. A., Burden, A. E., Kurtz, D. M. & Scott, R. A. Dissecting contributions to the thermostability of *Pyrococcus furiosus* rubredoxin: β-sheet chimeras. *Biochemistry* **36**, 10406-10413, (1997).

187 Vranish, J. N. *et al.* Fluorescent probes for tracking the transfer of iron-sulfur cluster and other metal cofactors in biosynthetic reaction pathways. *J Am Chem Soc* **137**, 390-398, (2015).

188 Fish, W. W. in *Methods in Enzymology* Vol. 158 Ch. 27, 357-364 (1988).

189 Beinert, H. Semi-micro methods for analysis of labile sulfide and of labile sulfide plus sulfane sulfur in unusually stable iron-sulfur proteins. *Analytical Biochemistry* **131**, 373-378, (1983).

190 Fang, H. *et al.* Histidine ligand variants of a flavo-diiron protein: effects on structure and activities. *J Biol Inorg Chem* **17**, 1231-1239, (2012).

191 Noble, R. W. & Gibson, Q. H. The reaction of ferrous horseradish peroxidase with hydrogen peroxide. *J Biol Chem* **245**, 2409-2413, (1970).

192 Stanley, J. L., Rauchfuss, T. B. & Wilson, S. R. Studies on the condensation pathway to and properties of diiron azadithiolate carbonyls. *Organometallics* **26**, 1907-1911, (2007).

193 Li, H. & Rauchfuss, T. B. Iron carbonyl sulfides, formaldehyde, and amines condense to give the proposed azadithiolate cofactor of the Fe-only hydrogenases. *J Am Chem Soc* **124**, 726-727, (2002).

194 Schmidt, M., Contakes, S. M. & Rauchfuss, T. B. First generation analogues of the binuclear site in the Fe-only hydrogenases: Fe-2(mu-SR)(2)(CO)(4)(CN)(2)(2-). *J Am Chem Soc* **121**, 9736-9737, (1999).

195 Lawrence, J. D., Li, H. X., Rauchfuss, T. B., Benard, M. & Rohmer, M. M. Diiron azadithiolates as models for the iron-only hydrogenase active site: Synthesis, structure, and stereoelectronics. *Angew Chem Int Edit* **40**, 1768-1771, (2001).

196 Larkin, M. A. *et al.* Clustal W and Clustal X version 2.0. *Bioinformatics* **23**, 2947-2948, (2007).

197 McWilliam, H. *et al.* Analysis Tool Web Services from the EMBL-EBI. *Nucleic Acids Research* **41**, W597-W600, (2013).

198 Maddison, W. & Maddison, D. Mesquite: a modular system for evolutionary analysis. Version 3.10 http://mesquiteproject.org. (2016).

199 Huelsenbeck, J. P. & Ronquist, F. MRBAYES: Bayesian inference of phylogenetic trees. *Bioinformatics* **17**, 754-755, (2001).

200 Ronquist, F. & Huelsenbeck, J. P. MrBayes 3: Bayesian phylogenetic inference under mixed models. *Bioinformatics* **19**, 1572-1574, (2003).

201 Morariu, V. I., Srinivasan, B. V., Raykar, V. C., Duraiswami, R. & Davis, L. S. Automatic online tuning for fast Gaussian summation. *Advances in Neural Information Processing Systems (NIPS)*, (2008).

202 Léger, C., Dementin, S., Bertrand, P., Rousset, M. & Guigliarelli, B. Inhibition and aerobic inactivation kinetics of Desulfovibrio fructosovorans NiFe hydrogenase studied by protein film voltammetry. *Journal of the American Chemical Society* **126**, 12162-12172, (2004).

203 Gaussian 09 (Gaussian, Inc., Wallingford, CT, USA, 2009).

204 Pandey, A. S., Harris, T. V., Giles, L. J., Peters, J. W. & Szilagyi, R. K. Dithiomethylether as a ligand in the hydrogenase H-cluster. *J Am Chem Soc* **130**, 4533-4540, (2008).

205 Edgar, R. C. MUSCLE: a multiple sequence alignment method with reduced time and space complexity. *Bmc Bioinformatics* **5**, 1-19, (2004).

206 Edgar, R. C. MUSCLE: multiple sequence alignment with high accuracy and high throughput. *Nucleic Acids Research* **32**, 1792-1797, (2004).

207 Waterhouse, A. M., Procter, J. B., Martin, D. M. A., Clamp, M. & Barton, G. J. Jalview Version 2-a multiple sequence alignment editor and analysis workbench. *Bioinformatics* **25**, 1189-1191, (2009).

208 Battye, T. G. G., Kontogiannis, L., Johnson, O., Powell, H. R. & Leslie, A. G. W. iMOSFLM: a new graphical interface for diffraction-image processing with MOSFLM. *Acta Crystallogr D* **67**, 271-281, (2011).

209 Bailey, S. The Ccp4 Suite - Programs for Protein Crystallography. *Acta Crystallogr D* **50**, 760-763, (1994).

210 Mccoy, A. J. *et al.* Phaser crystallographic software. *J Appl Crystallogr* **40**, 658-674, (2007).

211 Emsley, P., Lohkamp, B., Scott, W. G. & Cowtan, K. Features and development of Coot. *Acta Crystallogr D* **66**, 486-501, (2010).

212 Adams, P. D. *et al.* PHENIX: a comprehensive Python-based system for macromolecular structure solution. *Acta Crystallogr D* **66**, 213-221, (2010).

213 Li, W. Z. & Godzik, A. Cd-hit: a fast program for clustering and comparing large sets of protein or nucleotide sequences. *Bioinformatics* **22**, 1658-1659, (2006).

214 Wittkop, T. *et al.* Comprehensive cluster analysis with Transitivity Clustering. *Nature Protocols* **6**, (2011).

215 Cline, M. S. *et al.* Integration of biological networks and gene expression data using Cytoscape. *Nature Protocols* **2**, 2366-2382, (2007).

216 Marchler-Bauer, A. & Bryant, S. H. CD-Search: protein domain annotations on the fly. *Nucleic Acids Research* **32**, W327-W331, (2004).

217 Sievers, F. *et al.* Fast, scalable generation of high-quality protein multiple sequence alignments using Clustal Omega. *Molecular Systems Biology* **7**, (2011).

218 Crooks, G. E., Hon, G., Chandonia, J. M. & Brenner, S. E. WebLogo: A sequence logo generator. *Genome Res* **14**, 1188-1190, (2004).

219 Cammack, R., Frey, M. & Robson, R. *Hydrogen as a fuel: learning from nature*. (Taylor & Francis, 2001).

220 Cammack, R. Redox Enzymes - Splitting Molecular-Hydrogen. *Nature* **373**, 556-557, (1995).

221 Mulder, D. W. *et al.* Activation of HydA(ΔEFG) requires a preformed [4Fe-4S] cluster. *Biochemistry* **48**, 6240-6248, (2009).

222 Mulder, D. W. *et al.* Stepwise [FeFe]-hydrogenase H-cluster assembly revealed in the structure of HydA(ΔEFG). *Nature* **465**, 248-251, (2010).

223 Knörzer, P. *et al.* Importance of the protein framework for catalytic activity of [FeFe]-hydrogenases. *J Biol Chem* **287**, 1489-1499, (2012).

224 Miyake, T. *et al.* Does the environment around the H-cluster allow coordination of the pendant amine to the catalytic iron center in [FeFe] hydrogenases? Answers from theory. *J Biol Inorg Chem* **18**, 693-700, (2013).

225 Baffert, C. *et al.* Hydrogen-activating enzymes: activity does not correlate with oxygen sensitivity. *Angew Chem Int Ed Engl* **47**, 2052-2054, (2008).

226 Huang, H., Wang, S., Moll, J. & Thauer, R. K. Electron bifurcation involved in the energy metabolism of the acetogenic bacterium *Moorella thermoacetica* growing on glucose or H_2 plus CO_2. *J Bacteriol* **194**, 3689-3699, (2012).

227 Gupta, N. *et al.* Recombinant *Desulfovibrio vulgaris* rubrerythrin. Isolation and characterization of the diiron domain. *Biochemistry* **34**, 3310-3318, (1995).

228 Ravi, N., Prickril, B. C., Kurtz, D. M., Jr. & Huynh, B. H. Spectroscopic characterization of 57Fe-reconstituted rubrerythrin, a non-heme iron protein with structural analogies to ribonucleotide reductase. *Biochemistry* **32**, 8487-8491, (1993).

229 Fox, B. G., Surerus, K. K., Munck, E. & Lipscomb, J. D. Evidence for a Mu-Oxo-Bridged Binuclear Iron Cluster in the Hydroxylase Component of Methane Monooxygenase - Mossbauer and Electron-Paramagnetic-Res Studies. *Journal of Biological Chemistry* **263**, 10553-10556, (1988).

230 Lynch, J. B., Juarez-Garcia, C., Munck, E. & Que, L., Jr. Mossbauer and EPR studies of the binuclear iron center in ribonucleotide reductase from Escherichia coli. A new iron-to-protein stoichiometry. *J Biol Chem* **264**, 8091-8096, (1989).

231 Erbes, D. L. & Burris, R. H. The kinetics of methyl viologen oxidation and reduction by the hydrogenase from Clostridium pasteurianum. *Biochim Biophys Acta* **525**, 45-54, (1978).

232 Vonabendroth, G. *et al.* Optimized over-expression of [FeFe] hydrogenases with high specific activity in Clostridium acetobutylicum. *International Journal of Hydrogen Energy* **33**, 6076-6081, (2008).

233 Morra, S. *et al.* Site saturation mutagenesis demonstrates a central role for cysteine 298 as proton donor to the catalytic site in CaHydA [FeFe]-hydrogenase. *PLoS One* **7**, e48400, (2012).

234 Fourmond, V. *et al.* Steady-state catalytic wave-shapes for 2-electron reversible electrocatalysts and enzymes. *J Am Chem Soc* **135**, 3926-3938, (2013).

235 Adams, M. W. The mechanisms of H2 activation and CO binding by hydrogenase I and hydrogenase II of Clostridium pasteurianum. *J Biol Chem* **262**, 15054-15061, (1987).

236 Liebgott, P. P. *et al.* Relating diffusion along the substrate tunnel and oxygen sensitivity in hydrogenase. *Nat Chem Biol* **6**, 63-70, (2010).

237 Fourmond, V. *et al.* The oxidative inactivation of FeFe hydrogenase reveals the flexibility of the H-cluster. *Nat Chem* **6**, 336-342, (2014).

238 Siebel, J. F. *et al.* Hybrid [FeFe]-hydrogenases with modified active sites show remarkable residual enzymatic activity. *Biochemistry* **54**, 1474-1483, (2015).

239 Hsieh, C. H. *et al.* Structural and spectroscopic features of mixed valent Fe(II)Fe(I) complexes and factors related to the rotated configuration of diiron hydrogenase. *J Am Chem Soc* **134**, 13089-13102, (2012).

240 Chernev, P. *et al.* Hydride binding to the active site of [FeFe]-hydrogenase. *Inorg Chem* **53**, 12164-12177, (2014).

241 Peters, J. W. X-ray Crystal Structure of the Fe-Only Hydrogenase (CpI) from Clostridium pasteurianum to 1.8 Angstrom Resolution. *Science* **282**, 1853-1858, (1998).

242 Nicolet, Y. *et al.* Crystallographic and FTIR spectroscopic evidence of changes in Fe coordination upon reduction of the active site of the Fe-only hydrogenase from Desulfovibrio desulfuricans. *Journal of the American Chemical Society* **123**, 1596-1601, (2001).

243 Nicolet, Y., Piras, C., Legrand, P., Hatchikian, C. E. & Fontecilla-Camps, J. C. Desulfovibrio desulfuricans iron hydrogenase: the structure shows unusual coordination to an active site Fe binuclear center. *Structure (London, England : 1993)* **7**, 13-23, (1999).

244 Pandey, A. S., Harris, T. V., Giles, L. J., Peters, J. W. & Szilagyi, R. K. Dithiomethylether as a ligand in the hydrogenase h-cluster. *Journal of the American Chemical Society* **130**, 4533-4540, (2008).

245 Siegbahn, P. E. M., Tye, J. W. & Hall, M. B. Computational studies of [NiFe] and [FeFe] hydrogenases. *Chem Rev* **107**, 4414-4435, (2007).

246 Silakov, A., Wenk, B., Reijerse, E. & Lubitz, W. (14)N HYSCORE investigation of the H-cluster of [FeFe] hydrogenase: evidence for a nitrogen in the dithiol bridge. *Phys Chem Chem Phys* **11**, 6592-6599, (2009).

247 Hatchikian, E. C., Magro, V., Forget, N., Nicolet, Y. & Fontecilla-Camps, J. C. Carboxy-terminal processing of the large subunit of [Fe] hydrogenase from Desulfovibrio desulfuricans ATCC 7757. *J Bacteriol* **181**, 2947-2952, (1999).

248 Adamska, A. *et al.* Identification and characterization of the "super-reduced" state of the H-cluster in [FeFe] hydrogenase: a new building block for the catalytic cycle? *Angew Chem Int Ed Engl* **51**, 11458-11462, (2012).

249 Mulder, D. W. *et al.* EPR and FTIR analysis of the mechanism of H2 activation by [FeFe]-hydrogenase HydA1 from Chlamydomonas reinhardtii. *J Am Chem Soc* **135**, 6921-6929, (2013).

250 Roseboom, W., De Lacey, A. L., Fernandez, V. M., Hatchikian, E. C. & Albracht, S. P. The active site of the [FeFe]-hydrogenase from Desulfovibrio desulfuricans. II. Redox properties, light sensitivity and CO-ligand exchange as observed by infrared spectroscopy. *J Biol Inorg Chem* **11**, 102-118, (2006).

251 Silakov, A., Kamp, C., Reijerse, E., Happe, T. & Lubitz, W. Spectroelectrochemical characterization of the active site of the [FeFe] hydrogenase HydA1 from Chlamydomonas reinhardtii. *Biochemistry* **48**, 7780-7786, (2009).

252 Adamska-Venkatesh, A. *et al.* New redox states observed in [FeFe] hydrogenases reveal redox coupling within the H-cluster. *J Am Chem Soc* **136**, 11339-11346, (2014).

253 De Lacey, A. L., Fernandez, V. M., Rousset, M. & Cammack, R. Activation and inactivation of hydrogenase function and the catalytic cycle: spectroelectrochemical studies. *Chem Rev* **107**, 4304-4330, (2007).

254 Chen, Z. *et al.* Infrared studies of the CO-inhibited form of the Fe-only hydrogenase from Clostridium pasteurianum I: examination of its light sensitivity at cryogenic temperatures. *Biochemistry* **41**, 2036-2043, (2002).

255 Gilbert-Wilson, R. *et al.* Spectroscopic Investigations of [FeFe] Hydrogenase Maturated with [(57)Fe2(adt)(CN)2(CO)4](2.). *J Am Chem Soc* **137**, 8998-9005, (2015).

256 Adamska, A. *et al.* Identification and Characterization of the “Super-Reduced” State of the H-Cluster in [FeFe] Hydrogenase: A New Building Block for the Catalytic Cycle? *Angewandte Chemie (International ed. in English)* **51**, 11458-11462, (2012).

257 Kamp, C. *et al.* Isolation and first EPR characterization of the [FeFe]-hydrogenases from green algae. *Biochim Biophys Acta* **1777**, 410-416, (2008).

258 De Lacey, A. L. *et al.* IR spectroelectrochemical study of the binding of carbon monoxide to the active site of Desulfovibrio fructosovorans Ni-Fe hydrogenase. *J Biol Inorg Chem* **7**, 318-326, (2002).

259 Kubas, G. J. Fundamentals of H2 binding and reactivity on transition metals underlying hydrogenase function and H2 production and storage. *CHem Rev* **107**, 4152-4205, (2007).

260 Canfield, D. E. THE EARLY HISTORY OF ATMOSPHERIC OXYGEN: Homage to Robert M. Garrels. *Annual Review of Earth and Planetary Sciences* **33**, 1-36, (2005).

261 Sessions, A. L., Doughty, D. M., Welander, P. V., Summons, R. E. & Newman, D. K. The continuing puzzle of the great oxidation event. *Curr Biol* **19**, R567-574, (2009).

262 Jang, S. & Imlay, J. A. Micromolar intracellular hydrogen peroxide disrupts metabolism by damaging iron-sulfur enzymes. *J Biol Chem* **282**, 929-937, (2007).

263 Strand, K. R. *et al.* Oxidative stress protection and the repair response to hydrogen peroxide in the hyperthermophilic archaeon Pyrococcus furiosus and in related species. *Arch Microbiol* **192**, 447-459, (2010).

264 Lakhal, R. *et al.* Oxygen uptake rates in the hyperthermophilic anaerobe Thermotoga maritima grown in a bioreactor under controlled oxygen exposure: clues to its defence strategy against oxidative stress. *Arch Microbiol* **193**, 429-438, (2011).

265 Iyer, R. B., Silaghi-Dumitrescu, R., Kurtz, D. M., Jr. & Lanzilotta, W. N. High-resolution crystal structures of Desulfovibrio vulgaris (Hildenborough) nigerythrin: facile, redox-dependent iron movement, domain interface variability, and peroxidase activity in the rubrerythrins. *J Biol Inorg Chem* **10**, 407-416, (2005).

266 Smoukov, S. K. *et al.* EPR and ENDOR evidence for a 1-His, hydroxo-bridged mixed-valent diiron site in Desulfovibrio vulgaris rubrerythrin. *Biochemistry* **42**, 6201-6208, (2003).

267 deMare, F., Kurtz, D. M., Jr. & Nordlund, P. The structure of Desulfovibrio vulgaris rubrerythrin reveals a unique combination of rubredoxin-like FeS4 and ferritin-like diiron domains. *Nat Struct Biol* **3**, 539-546, (1996).

268 Jin, S., Kurtz, D. M., Jr., Liu, Z. J., Rose, J. & Wang, B. C. X-ray crystal structure of Desulfovibrio vulgaris rubrerythrin with zinc substituted into the [Fe(SCys)4] site and alternative diiron site structures. *Biochemistry* **43**, 3204-3213, (2004).

269 Fushinobu, S., Shoun, H. & Wakagi, T. Crystal structure of sulerythrin, a rubrerythrin-like protein from a strictly aerobic archaeon, Sulfolobus tokodaii strain 7, shows unexpected domain swapping. *Biochemistry* **42**, 11707-11715, (2003).

270 May, A., Hillmann, F., Riebe, O., Fischer, R. J. & Bahl, H. A rubrerythrin-like oxidative stress protein of Clostridium acetobutylicum is encoded by a duplicated gene and identical to the heat shock protein Hsp21. *FEMS Microbiol Lett* **238**, 249-254, (2004).

271 Sieker, L. C. *et al.* The 1.9 A crystal structure of the "as isolated" rubrerythrin from Desulfovibrio vulgaris: some surprising results. *J Biol Inorg Chem* **5**, 505-513, (2000).

272 Griese, J. J. & Hogbom, M. X-ray reduction correlates with soaking accessibility as judged from four non-crystallographically related diiron sites. *Metallomics* **4**, 894-898, (2012).

273 Sigfridsson, K. G. *et al.* Rapid X-ray photoreduction of dimetal-oxygen cofactors in ribonucleotide reductase. *J Biol Chem* **288**, 9648-9661, (2013).

274 Leidel, N. *et al.* High-valent [MnFe] and [FeFe] cofactors in ribonucleotide reductases. *Biochim Biophys Acta* **1817**, 430-444, (2012).

275 DeMaré, F. *et al.* Re-engineering the diiron site in rubrerythrin towards that in ribonucleotide reductase. *Inorganica Chimica Acta* **263**, 255-262, (1997).

276 Molloy, S. Environmental microbiology: disentangling syntrophy. *Nat Rev Microbiol* **12**, 7, (2014).

277 Morris, B. E., Henneberger, R., Huber, H. & Moissl-Eichinger, C. Microbial syntrophy: interaction for the common good. *FEMS Microbiol Rev* **37**, 384-406, (2013).

278 Biswas, R., Zheng, T., Olson, D. G., Lynd, L. R. & Guss, A. M. Elimination of hydrogenase active site assembly blocks H2 production and increases ethanol yield in Clostridium thermocellum. *Biotechnol Biofuels* **8**, 20, (2015).

279 Lubner, C. E., Grimme, R., Bryant, D. A. & Golbeck, J. H. Wiring photosystem I for direct solar hydrogen production. *Biochemistry* **49**, 404-414, (2010).

280 Hambourger, M. *et al.* [FeFe]-hydrogenase-catalyzed H2 production in a photoelectrochemical biofuel cell. *Journal of the American Chemical Society* **130**, 2015-2022, (2008).

281 Justice, A. K., Zampella, G., Gioia, L. D. & Rauchfuss, T. B. Lewis vs. Br?nsted-basicities of diiron dithiolates: spectroscopic detection of the ?rotated structure? and remarkable effects of ethane- vs. propanedithiolate. *Chemical Communications*, 2019, (2007).

282 Thomas, C. M., Darensbourg, M. Y. & Hall, M. B. Computational definition of a mixed valent Fe(II)Fe(I) model of the [FeFe]hydrogenase active site resting state. *J Inorg Biochem* **101**, 1752-1757, (2007).

283 Liu, Z. P. & Hu, P. A density functional theory study on the active center of Fe-only hydrogenase: characterization and electronic structure of the redox states. *J Am Chem Soc* **124**, 5175-5182, (2002).

284 Bruschi, M. *et al.* Functionally relevant interplay between the Fe(4)S(4) cluster and CN(-) ligands in the active site of [FeFe]-hydrogenases. *J Am Chem Soc* **132**, 4992-4993, (2010).

285 Bruschi, M. *et al.* Influence of the [2Fe]H subcluster environment on the properties of key intermediates in the catalytic cycle of [FeFe] hydrogenases: hints for the rational design of synthetic catalysts. *Angew Chem Int Ed Engl* **48**, 3503-3506, (2009).

286 Bruschi, M. *et al.* in *Encyclopedia of Inorganic and Bioinorganic Chemistry.* (2011).

287 Boyd, E. S. *et al.* [FeFe]-hydrogenase abundance and diversity along a vertical redox gradient in Great Salt Lake, USA. *Int J Mol Sci* **15**, 21947-21966, (2014).

288 Hrdy, I. *et al.* Trichomonas hydrogenosomes contain the NADH dehydrogenase module of mitochondrial complex I. *Nature* **432**, 618-622, (2004).

289 Burroughs, A. M., Balaji, S., Iyer, L. M. & Aravind, L. A novel superfamily containing the beta-grasp fold involved in binding diverse soluble ligands. *Biol Direct* **2**, (2007).

290 Zhulin, I. B., Taylor, B. L. & Dixon, R. PAS domain S-boxes in Archaea, Bacteria and sensors for oxygen and redox. *Trends Biochem Sci* **22**, 331-333, (1997).

291 Taylor, B. L. & Zhulin, I. B. PAS domains: internal sensors of oxygen, redox potential, and light. *Microbiol Mol Biol Rev* **63**, 479-506, (1999).

292 Vignais, P. M., Billoud, B. & Meyer, J. in *FEMS Microbiology Reviews* Vol. 25 455-501 (2001).

293 Boyd, E. S., Hamilton, T. L., Spear, J. R., Lavin, M. & Peters, J. W. [FeFe]-hydrogenase in Yellowstone National Park: evidence for dispersal limitation and phylogenetic niche conservatism. *ISME J* **4**, 1485-1495, (2010).

294 Stripp, S. T. *et al.* How oxygen attacks [FeFe] hydrogenases from photosynthetic organisms. *Proc Natl Acad Sci U S A* **106**, 17331-17336, (2009).

295 Lambertz, C. *et al.* O2 reactions at the six-iron active site (H-cluster) in [FeFe]-hydrogenase. *J Biol Chem* **286**, 40614-40623, (2011).

296 Swanson, K. D. *et al.* [FeFe]-hydrogenase oxygen inactivation is initiated at the H cluster 2Fe subcluster. *J Am Chem Soc* **137**, 1809-1816, (2015).